**Springer Theses**
Recognizing Outstanding Ph.D. Research

Tuan Anh Ho

# Nanoscale Fluid Transport

## From Molecular Signatures to Applications

Springer

## Springer Theses

Recognizing Outstanding Ph.D. Research

## Aims and Scope

The series "Springer Theses" brings together a selection of the very best Ph.D. theses from around the world and across the physical sciences. Nominated and endorsed by two recognized specialists, each published volume has been selected for its scientific excellence and the high impact of its contents for the pertinent field of research. For greater accessibility to non-specialists, the published versions include an extended introduction, as well as a foreword by the student's supervisor explaining the special relevance of the work for the field. As a whole, the series will provide a valuable resource both for newcomers to the research fields described, and for other scientists seeking detailed background information on special questions. Finally, it provides an accredited documentation of the valuable contributions made by today's younger generation of scientists.

## Theses are accepted into the series by invited nomination only and must fulfill all of the following criteria

- They must be written in good English.
- The topic should fall within the confines of Chemistry, Physics, Earth Sciences, Engineering and related interdisciplinary fields such as Materials, Nanoscience, Chemical Engineering, Complex Systems and Biophysics.
- The work reported in the thesis must represent a significant scientific advance.
- If the thesis includes previously published material, permission to reproduce this must be gained from the respective copyright holder.
- They must have been examined and passed during the 12 months prior to nomination.
- Each thesis should include a foreword by the supervisor outlining the significance of its content.
- The theses should have a clearly defined structure including an introduction accessible to scientists not expert in that particular field.

More information about this series at http://www.springer.com/series/8790

Tuan Anh Ho

# Nanoscale Fluid Transport

## From Molecular Signatures to Applications

Doctoral Thesis accepted by
University College London, UK

Springer

*Author*
Dr. Tuan Anh Ho
Geochemistry Department
Sandia National Laboratories
Albuquerque, NM
USA

*Supervisor*
Prof. Alberto Striolo
Department of Chemical Engineering
University College London
London
UK

ISSN 2190-5053 ISSN 2190-5061 (electronic)
Springer Theses
ISBN 978-3-319-47002-3 ISBN 978-3-319-47003-0 (eBook)
DOI 10.1007/978-3-319-47003-0

Library of Congress Control Number: 2016952999



Printed on acid-free paper

This Springer imprint is published by Springer Nature
The registered company is Springer International Publishing AG
The registered company address is: Gewerbestrasse 11, 6330 Cham, Switzerland

# Supervisor's Foreword

This thesis represents a comprehensive utilization of computational tools to elucidate fundamental physical phenomena that occur at the interface between solids and liquids. The tools employed include equilibrium and non-equilibrium molecular dynamics simulations, computational techniques that are finding more and more relevance because of the continuous improvement of high-end computational capabilities, and that are developed from rigorous statistical mechanics principles.

The liquids considered in this piece of original work contain water, either as the only fluid, the majority fluid within which salts are dissolved, or one of two rather immiscible fluids present. The solid substrates are carefully chosen to provide insights for the development of applications that are currently attracting enormous research interest because of their societal importance. The three applications explicitly considered in this thesis are (a) the design of drag-reducing and self-cleaning surfaces; (b) water desalination; and (c) the environmentally conscious development of shale gas.

The results obtained with relevance to each of the three applications are not only fascinating and interesting, but they in some cases challenge conventional wisdom. Regarding the first application, the analysis of the hydrodynamic boundary condition demonstrates, contrary to expectations, that it is possible to have a surface on which the contact angle of water is low, while supporting hydrodynamic slip. Regarding water desalination, the computational results presented in this thesis suggest a possible innovative technology that combines the advantages of membrane and capacitive desalination processes, while reducing their limitations. Regarding shale gas, the results presented here demonstrate that the permeability of natural gas through the narrow clay pores that are present in shale formations strongly depend on the amount of water present and on the pressure drop, possibly explaining the fast decrease in productivity observed in unconventional gas fields after hydraulic fracturing processes.

London, UK
July 2016

Prof. Alberto Striolo

# Abstract

Motivated by the fact that many novel fluid transport phenomena have been discovered at nano length scales, in this thesis I use molecular dynamics simulations to investigate how a solid surface affects the fluid properties and fluid transport in nanochannels. My ultimate goal is to search for the molecular signatures of the macroscopic observations. From the understanding of the mutual relation between molecular properties and macroscopic observations, I learn how to tailor the fluid–solid interaction to improve the performance of practical applications including nano-fluidic devices, water desalination, energy storage, and shale gas exploration. For example, in Chap. 3 I find out that liquid water can slip on hydrophilic surfaces, which contradicts conventional knowledge. The responsible molecular signature appears to be the dynamical properties of interfacial water molecules, governed by the strength of water–surface interactions and surface morphology. When water molecules can migrate from one preferential adsorption site to the next without requiring hopping events, hydrodynamic liquid slip occurs. In Chap. 4 I illustrate that the structural and dynamical properties of the electric double layer formed near graphene electrodes are crucial to the performance of supercapacitors and capacitive desalination devices. By tailoring the electrode, thin and mobile electric double layer can be obtained that can tremendously enhance the capacitance of supercapacitors and the manner that capacitive desalination devices is operated. Finally, in the study of two-phase (water and methane) flow through muscovite nanopore reported in Chap. 5 I demonstrate that the flow pattern change not only affects the movement of methane with respect to that of water but also affects the pore structure, in particular its width. As muscovite has similar structure to illite, a clay often found in shale rocks, these results advance our understanding regarding the mechanism of water and gas transport in tight shale gas formations.

**Parts of this thesis have been published in the following journal articles:**

1. T.A. Ho, D.V. Papavassiliou, L.L. Lee, A. Striolo, *Water Can Slip on a Hydrophilic Surface*, **Proceedings of the National Academy of Sciences of the United States of America** 108 (**2011**) 16170–16175.
2. T.A. Ho and A. Striolo, *Promising Performance Indicators for Water Desalination and Aqueous Capacitors Obtained by Engineering the Electric Double Layer in Nano-Structured Carbon Electrodes*, **J. Phys. Chem. C** 119 **(2015)** 3331–3337.
3. T.A. Ho and A. Striolo, *Water and Methane in Shale Rocks: Flow Pattern Effects on Fluid Transport and Pore Structure,* AIChE Journal 61 **(2015)** 2993.
4. T.A. Ho and A. Striolo, Polarizability Effects in Molecular Dynamics Simulations of the Graphene-Water Interface, **J. Chem. Phys.** 138 **(2013)** 054117.

# Acknowledgements

I would like to express my deepest gratitude to my advisor Prof. Alberto Striolo for his guidance, encouragement, motivation, and support throughout my Ph.D. study. I appreciate his time and efforts spending to help me improve my personal skills and build my career. I enjoy my time working in his fantastic group and I am very proud of what we have achieved together.

I would like to thank Prof. Haroun Mahgerefteh for serving as my secondary advisor. Special thanks to Prof. Dimitrios Papavassiliou for the collaborations and advice during early years of my Ph.D. study. I am also grateful to my undergraduate advisor, Dr. L.H. Nguyen for encouraging me to enter postgraduate school and for all the interesting discussions we had every time I visit. Thank you my officemates, colleagues, and friends for all the fun and joy we shared during my Ph.D. study.

This thesis is dedicated to my wonderful parents and my lovely sisters, who always believe and encourage me. Words cannot express my gratitude for everything they have done to make me into who I am. I hope I have made them proud. This thesis is also dedicated to my other half Ngoc Nguyen. I am thankful to my wife for love and care and for sharing with me every moment of this incredible journey. I am looking forward to our new one. Finally thank you my unborn baby Tony for encouraging me to leave doctoral school for a new job. I cannot wait to have him in this world.

February 2015

Tuan Anh Ho
University College London

# Contents

# Chapter 1
# Introduction

Nanoscale fluid transport is usually referred to the fluid flow through a channel with the size along one or more directions below 100 nm [1, 2]. At this small length scale, due to high surface area to volume ratio, the fluid-solid interaction at solid/fluid interface is one of the dominant factors that governs fluid behaviour [3]. Because of this unique feature many interesting transport phenomena particularly occur on this length scale including hydrodynamic slip boundary condition [4], diffusion limited reaction [5], overlap electric double layer and surface-charge-governed ion transport [6, 7], and single-file molecular transport [8]. These novel transport phenomena are discovered in many disciplines in science and engineering [9] and have initiated a wide range of innovative applications such as separation, water desalination, solvent and solute transport, energy conversion, and biosensing [1, 9–11]. In the remainder of this chapter I briefly introduce some related literature and state my research topic.

Perhaps, one of the most novel fluid transport phenomena that has been intensively studied in the past few decades is the hydrodynamic slip boundary condition. I could mention here an endless list of publications on this interesting topic over years [4, 12–20]. These publications reminisce the assumption that when a fluid flows inside a macrochannel the fluid near the surface travels at the same speed as the surface does. In other words, the fluid in contact with the surface is stationary with regard to the surface (i.e., no slip boundary condition) [21]. This no slip boundary condition is successfully applied to model various macroscopic experiments. However, the assumption of no slip boundary condition is violated when fluids flow inside nanochannels. Many experimental and simulation results strongly suggest that interfacial fluids can slip on nanochannel surfaces [4]. For example, Craig et al. [22] used an atomic force microscope (AFM) to measure the hydrodynamic drainage force and concluded that hydrodynamic slip boundary condition occurs. Zhu and Granick [20] used surface force apparatus (SFA) to measure the drainage force between two approaching surfaces and suggested that the drainage force becomes up to two to four orders of magnitude less than expected, which is caused by the slip boundary condition at interface. Barrat and Bocquet [23]



T.A. Ho, *Nanoscale Fluid Transport*, Springer Theses,
DOI 10.1007/978-3-319-47003-0_1

simulated the flow of Lennard-Jones fluid on a solid substrate. They concluded that when the contact angle of a liquid droplet sitting on a solid surface is large enough the boundary condition of the liquid flow on that surface remarkably differs from the no-slip boundary condition.

In the context of the hydrodynamic slip boundary condition, carbon nanotube (CNT) and graphene are the exceptional materials that offer a large degree of liquid slip. Large liquid slip can reduce the friction between liquid and wall, and increase the flow rate compared to the continuum hydrodynamic theory. The flow enhancement, which is the ratio between the flow rate measured in nanochannels and that estimated using continuum hydrodynamic theory, is described as $\varepsilon = Q_{slip}/Q_{no-slip} = \left(1 + 8L_s/D\right)$, where $L_s$ and D are the slip length and diameter of CNT, respectively [24, 25]. The slip length $L_s$ reported for water flow in CNT and graphene varies from a few nm to a few mm [24]. For example, Majumder et al. [26] experimentally studied the water flow in 7 nm CNT and reported very large slip length from $39 \times 10^3$ to $68 \times 10^3$ nm. As a result the flow rate inside 7 nm [26] was found to be four to five orders of magnitude higher than that predicted from continuum hydrodynamic theory. Holt et al. [27] investigated water flow in sub-2 nm CNTs and found the slip length from 140 to 1400 nm. Thomas et al. [28] applied MD simulation to study pressure-driven water flow through 1.66–4.99 nm CNT and reported the slip length varies from 30 to 110 nm. Koumoutsakos et al. [29] conducted non-equilibrium simulations to study water flow in graphite nanopore and estimated the slip length of 64 nm. Maali et al. [17] indirectly measured the slip length of water on graphite surface using AFM and found the slip length of 8 nm.

When the CNT diameter is small enough (0.81 nm) the water flow through CNT exhibits another unique feature. Hummer et al. [30], in their molecular dynamics simulation study, observed the simultaneous and continuous filling of CNT with a one-dimensionally ordered chain of water molecules (i.e., the single-file water transport mechanism). This special water configuration was also reported later by Suk and Aluru [31] in a molecular modelling study of the water transport through ultrathin graphene.

>Rapid water transport observed CNT and graphene pore when coupling with ion rejection can advance tremendously water purification applications. Working toward this goal, Fornasiero et al. [32] experimentally study ion rejection in sub-2 nm CNT with the negatively charged group attached to the tube entrance. Their results indicate that about 98 % of ion rejection can be achieved and that the electrostatic interactions dominate over steric and hydrodynamic effects in governing ion rejection. Corry [33] in a molecular dynamics simulation study shown that salt rejection of the 0.66, 0.81, 0.93, and 1.09 nm CNTs under the hydrostatic pressure of 208 MPa is 100, 100, 95, and 58 %, respectively. The narrow CNT not only extremely well rejects the ion but also conducts the water at several orders faster than the existing membranes do. Cohen-Tanugi and Grossman [34] studied water desalination across nanoporous graphene. They reported that the desalination performance of graphene membrane depends on pore size, chemical

functionalization, and applied pressure. Hydroxyl groups attached to the edge of the graphene pore can roughly double the water flux due to the ability of hydroxyl functional groups to substitute for water molecules in the ion hydration shell.

The CNT and graphene nanopores not only can reject ions but also can distinguish ion types (i.e., ion selectivity). For example, Sint et al. [35] used molecular dynamics simulations to study ion selectivity through functionalized graphene nanopores. The graphene nanopore functionalized by negatively charged nitrogen and fluorine favors the passages of cations such as lithium, sodium, and potassium. The graphene pore terminated by positively charged hydrogen favors the passages of anions such as chloride and bromine. The selectivity is caused by the electrostatic interaction between ions and functional groups. He et al. [36] suggested that by functionalizing graphene nanopore, changing pore size, and manipulating external field the graphene nanopores can select either potassium or sodium ions. Hilder et al. [37] demonstrated that the (5,5) silicon carbide (SiC) nanotube can reject both sodium and chloride ions, but the (6,6) and the (7,7) SiC nanotubes were found to be chloride-selective. Song and Corry [38] conducted molecular dynamics simulations to investigate the ion-selectivity through single-walled carbon nanotube. They demonstrated that different dehydration energies of ions, hydration shell structures, and interactions with carbon nanotube result in different free energy barriers when ions enter nanotube.

Ion transport through nanochannels also involves in various electrokinetic phenomena including electro-osmosis [39]. Because of the strong electrostatic interaction between ions and surface charges and because of confinement effects, the behaviour of ions inside nanochannels differs from bulk behaviour. For example, Stein et al. [6] experimentally studied the ion transport in 70 nm silica nanochannel. They concluded that at low concentration, the conductance of nanochannel strongly deviates from the bulk behaviours. When the channel size is small, the electric double layer (EDL) near the top surface overlaps with the EDL near the bottom surface. Inside the overlap EDL most of ions are counterions and the number of counterions inside this EDL depends only on the surface charge. Because the channel conductance depends only on the number of the counterions it is independent of bulk electrolyte solution [7].

In the last decade, because of the success of shale gas production in the USA phenomena occurring that nanometer scale, in particular the gas flow in nanopores, have attracted great attention of scientists worldwide. Shale is fine-grained, sedimentary rock characterized by small pores ranging from 1 to 200 nm [40]. The permeability is usually used as a measure of how easy fluid flows through the rock matrix. It depends largely on the connectivity of the fracture networks and interaction between fluid and shale rock. High porosity does not always yield high permeability because of lack of the flow path. The permeability of shale rocks can be as low as 1–100 nanodarcy, (for comparison, the permeability of sandstone is of the order of 1–10 millidarcy) [41]. To economically produce natural gas from shale horizontal drilling and hydraulic fracturing have been carried out. The former exposes more wellbores to the reservoir while the later creates more fracture networks to increase the permeability [41].

Although inorganic matters such as clay minerals are the main component of shale reservoirs the amount and type of organic content decide whether a shale reservoir can be targeted for oil and gas exploration [42–44]. Because organic matter can adsorb gas and store significant amounts of free gas in its pores [45] the higher the concentration of organic matter in shale reservoir, the better its source potential [46]. Data in the literature also suggests that clay minerals do not significantly contribute to methane sorption in organic-rich shale (e.g., Barnett, Haynesville) [47, 48].

Under high pressure and temperature, organic matter is usually transformed into kerogen during sediment diagenesis [42, 49]. Depending on the kerogen types hydrocarbons in shale reservoir can be oil, wet gas, or dry gas. Based on the atomic H/C and O/C ratios (i.e., van Krevelen diagram), kerogen is usually classified into four types [42, 49]. Type I (e.g., Green River kerogen) is primarily formed in lacustrine and sometimes marine environments. It is highly aliphatic with H/C > 1.5 and O/C from 0.03 to 0.1. This type of kerogen mainly produces oil but sometime gas. Type II (e.g., Barnett kerogen) is typically formed in deep marine environments. It is rich in hydrogen and low in carbon (H/C $\sim$ 1.3, O/C $\sim$ 0.15). This kerogen can produce oil and gas. Type III is derived from higher plant debris (e.g., coal). It has H/C < 0.8 and O/C from 0.03 to 0.3. It can generate mostly dry gas. Type IV kerogen consists of residual organic matter with high carbon content and no hydrogen. This type of kerogen has no potential in generating hydrocarbons.

When a shale reservoir is targeted for oil and gas production horizontal drilling and hydraulic fracturing are carried out to extract hydrocarbons. During production stage, fluids flow through pore networks at different length scales. Figure 1.1 shows a conceptual model highlighting the importance of the phenomena occurring at nanometer length scale in shale gas production [50]. At nanometer length scale (yellow square), gas molecules desorb from kerogen/clay matrix and diffuse into the nanopore network. From nanopore network gas flows into micro-fracture network (purple square) and to wellbore for production (blue square). Because gases

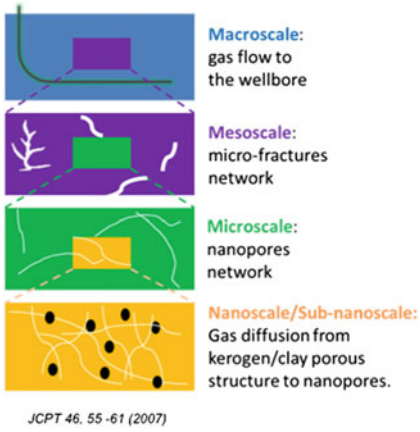


**Fig. 1.1** Conceptual model demonstrating multiple length scales involving in shale gas production (modified from [50])

desorption and diffusion in kerogen/clay matrix are the slowest processes they are considered to be the time-limiting steps governing the overall productivity. Understanding gas adsorption, desorption, diffusion, and flow in kerogen/clay nanopores, therefore, are important to the sustainability of un-conventional oil and gas production.

Different equations and models have been implemented to describe the flow in pores of different size. The Knudsen (Kn) number, the ratio between the mean free path of fluid molecule and the characteristic dimension of the pore, is usually used to classify the flow regime [51–53]. If Kn < 0.01 the flow in the pore can be assumed as continuum. The hydrodynamic non-slip boundary condition Hagen-Poiseuille equation or Darcy's law $Q = \frac{\pi r^4}{8\mu}\frac{\Delta P}{L}$ (where r is the pore radius, μ is the fluid viscosity, ΔP/L is the pressure drop along the channel length L) is suitable to estimate the flow rate in micropores in unconventional and conventional reservoirs [50]. When 0.01 < Kn < 0.1 gas molecules slip on the solid surface (i.e., slippage effect or Klinkenberg effect). As we discussed above, fluid slippage inside pores can lead to significant flow enhancement. The Darcy's law with the assumption of no-slip boundary condition underestimates the flow rate when slip occurs. Modification of the continuum theory such as Klinkenberg correction is required to correctly predict the gas flow rate in this flow regime [41, 54, 55]. When 0.1 < Kn < 10 (transition flow) both slip flow and diffusion flow can occur. At this flow regime traditional hydrodynamics equations start to fail to predict the flow rate [51]. When Kn > 10 continuum theory completely breaks down. The Knudsen diffusion equation $\frac{q\rho M}{\phi A} = D_k \frac{\Delta P}{RTL}$ (where q is the flow rate, ρ is the fluid density, ϕ is the porosity, ΔP is the pressure drop, A is the cross area, L is the length of pore, T is temperature, and $D_k = \frac{d}{3}\sqrt{\frac{8RT}{\pi M}}$ is the Knudsen diffusion coefficient) is used to estimate flow rate [27, 50]. The Knudsen diffusion theory is based on several assumptions. First, the pore size is much smaller than mean free path of molecules. Second, density is small so that gas-gas collisions are insignificant comparing to gas-wall collisions. In the nanopores such as those found in shale reservoirs the second assumption is violated because of high gas pressure and high fluid density [52]. Indeed, the Knudsen diffusion theory underestimated by at least one to two orders of magnitude the flow of fluid in carbon nanotube [27]. Therefore, accurate descriptions of gas transport through nanopores require more experimental or numerical studies.

Molecular modeling is a useful technique that has been extensively employed to study the flow inside shale matrix [52, 55–59]. Monte Carlo (MC) and molecular dynamics (MD) simulations can be deployed to simultaneously model adsorption and flows in nanopores, in particular nanopores in kerogen. To enable these simulations, different kerogen models were proposed. Ungerer et al. [60] developed kerogen models that differ in type and thermal maturation. Their kerogen molecules were built to reproduce the elemental properties obtained from the elemental and functional group analysis of the kerogen in Duvernay organic-rich marine shale formation [61]. The resultant models can predict thermodynamics properties and

volumetric properties of kerogen. Bousige et al. [62] constructed molecular model of immature and mature kerogens using a technique that combines MD and hybrid reverse MC simulations. Their models can reproduce the experimental pair distribution function, atomic chemical composition and density of kerogen. Thanks to the use of reactive force field their model can be implemented to study the structural deformation and fracture mechanism of kerogen under severe stimulation such as fracking [62]. Other authors used carbon material as a proxy to kerogen [59, 63]. In general, because of the limitation of molecular modeling all kerogen models possess only the micropores (<2 nm). The mesopores and macropores are not present.

Regarding the fluids flow in kerogen matrix, Falk et al. [63] employed molecular dynamics simulation to study the flow of condensed hydrocarbons through nanoporous media. They used carbon material as a model for kerogen. They concluded that Darcy's law fails to predict transport in shale nanoporous matrix because of the strong adsorption in kerogen and the breakdown of hydrodynamics at the nanoscale [63]. They proposed new theoretical framework basing on statistical mechanics molecular simulation that does not require assuming any flow types that is common in continuum theory. The new models base on the slip-like friction of hydrocarbons within the kerogen and a free volume term. Collell et al. [57] studied transport mechanism of hydrocarbons through kerogen membrane. The kerogen model used represents oil-prone type II kerogen. They concluded that the mechanism of hydrocarbons transport through kerogen membranes is purely diffusion. Ho et al. [64] employed MC and MD simulations to study the adsorption and extraction of methane from the kerogen matrix. The model they used is type II-D mature kerogen similar to that found in Barnett shale. The kerogen model yields density and pore size distribution that are in good agreement with experimental data. The comparison of the adsorption isotherm obtained from MC simulation with experimental results suggests that the model can be used to predict the amount of gas deposited in organic-rich shale in US. Interestingly, the methane extraction simulation is carried out to study the mechanism of methane release in kerogen. The results indicate that methane release from kerogen matrix occurs in a two-stages process. First, methane was produced very fast at the beginning of extraction. This is because the gas extracted is mainly the pressurized gas. The pressure gradient is the main driving force at this stage. After that methane is extracted at very slow rate due to the slow desorption and diffusion of gas in kerogen matrix. In overall the extraction rate profile obtained from MD simulation is, in some sense, in good agreement with the declines curves observed in field production. The prediction of the gas production in the future most likely depends on the gas extraction in the second stages.

From the above discussions, one can easily recognize that insight into nanoscale fluid transport phenomena can be studied using Monte Carlo (MC) and molecular dynamics (MD) simulations [65–69]. Molecular dynamics (MD) simulation packages [70, 71] solve Newton's second law of motion for each atom $\sum_j \boldsymbol{F_{ij}} = m_i \frac{d^2 \boldsymbol{r_i}}{dt^2}$, where $m_i$, $\mathbf{r_i}$, t, and $\mathbf{F_{ij}}$ are atomic mass, position of atom i, time, and force between atoms i and j, respectively. The force $\boldsymbol{F_{ij}} = -\nabla_i V_{ij}$, where $V_{ij}$ is the interaction potential. The equation of motion is usually integrated within the cut-off distance,

with the random initial configurations and initial velocities calculated from Boltzmann distribution [70]. To study the transport of fluid two types of flow are usually implemented. The first kind is the Couette flow, in which the atoms belonging to the surfaces are driven at a constant velocity. The second type is the Poiseuille flow, in which a body force is applied on each fluid atom [21]. The trajectory of each atom and thermodynamic properties are obtained from the simulation. By analysing these outputs, the physical properties of the system can be achieved enclosing density profile, velocity profile, radial distribution function, orientation distribution, diffusion coefficient, etc. These results help to understand the behaviours of fluid at solid/fluid interfaces and fluid transport in nanochannel. Multiple molecular dynamics simulation packages available are LAMMPS, GROMACS, CHARMM, NAMD, and materials studio.

Monte Carlo molecular simulation, in particular grand canonical Monte Carlo (GCMC) simulation has been extensively used to compute isotherms in porous materials. Therefore, it is a good tool to estimate how much fluid should be present inside nanopores at specific thermodynamics conditions before MD simulation is carried out. Technically, MC simulation is started from a microstate (i.e., configuration) that is part of the sampling ensemble, and then moved on to a new microstate (i.e., new configuration). If the energy of the new configuration is smaller than that of the old configuration the move is accepted. If the energy of new configuration is larger than the energy of the old configuration the move is accepted with probabilities that satisfy the Boltzmann distribution. For example, the probability of moving a configuration from lower energy state to higher energy state is $p$ ($p < 1$). A random number $Ra$ is generated from a uniform distribution in the interval [0,1]. The move is accepted if $Ra < p$ and rejected otherwise. It is important that the random-number generator does generate $Ra$ uniformly in the interval [0,1]. Even though the dynamics of the simulated system cannot be study using MC simulation, the equilibrium properties sampled by this technique should reproduce the real system's equilibrium properties [72].

In GCMC simulation, chemical potential, volume, and temperature are fixed. The principal of this technique is the adsorbed gas in nanopores is in equilibrium with gas in the imaginary reservoir. At equilibrium the temperature and chemical potential of fluid in simulation box equals to those of fluids in the reservoirs. There are two MC moves that we have to sample: (i) displacement of particle in which a particle is selected randomly and given a new position and (ii) insertion and removal of particles in which a particle is inserted into the system at random position or a random particle is removed from the system. These moves are accepted according to a mechanical statistical rule as discussed above. To be able to compare the calculated isotherms with experimental results the amount of fluid inside the pore as a function of pressure is desired. Because the pressure is related to the chemical potential by an equation of state it is always possible to calculate pressure corresponding to a given chemical potential and vice versa. Another approach would be to perform an "empty box" simulation (i.e. box without adsorbent) to establish the gas pressure at specific chemical potential [73]. Multiple

simulation packages are available to conduct MC molecular simulations including LAMMPS, Towhee, Music, and Cassandra.

Inspired by the fact that many novel fluid transport phenomena are discovered and play important roles in numerous applications and that molecular simulations have been used extensively to study nanoscale fluid transport, in this thesis I implement MD simulations to study fluid transport through nanochannels. In particular, I employ equilibrium and non-equilibrium atomistic molecular dynamics simulations using LAMMPS and GROMACS to investigate how fluids behave at interfaces (solid/liquid and liquid/gas interfaces) and how the interfacial fluid properties affect fluid transport. The solid substrates I consider are metal oxide surfaces, clay minerals, and graphene. The fluids are water, aqueous electrolyte solutions, and methane. My ultimate research goal is to search for the molecular signatures of the macroscopic observations. From the understanding of the mutual relation between molecular signatures and macroscopic observations, I learn how to tailor the fluid-solid interaction to improve the performance of practical applications as diverse as nano-fluidic devices, water desalination, energy storage, and shale gas exploration.

The thesis is organized as follow. In Chap. 2 I provide the basic background of molecular dynamics simulations. In Chap. 3 I report the results on the correlation between the molecular properties of interfacial water and the hydrodynamic boundary condition, which is described in terms of slip versus no-slip boundary conditions. Briefly, it is well known that hydrophobic surfaces tend to cause water slip whereas hydrophilic ones do not. My molecular dynamics simulation results, however, suggest that this dichotomy might be purely coincidental. Indeed, liquid water can slip on hydrophilic surfaces and the microscopic properties of interfacial water at solid/liquid interfaces are responsible for this observation. My finding could lead to the advancement of a variety of applications, including the design of hydrophilic nano-porous membranes with high permeation and self-cleaning hydrophilic surfaces.

In Chap. 4 I provide details of the study on the role of thin and mobile electric double layers in capacitive desalination and energy storage. Shortly, the structural and dynamical properties of the ions accumulating near the electrodes are the main factors that affect the performance of the supercapacitors and capacitive desalination devices. Using MD simulations I proposed a composite electrodes that favour the formation of compact and mobile EDL. These allow us to both effectively and efficiently store energy and purify water.

In Chap. 5 I present my molecular dynamics simulation results for the study of the water and methane migration in muscovite nanopore. The effects of flow patterns on the fluid transport and on the pore structure are investigated. The results indicate the movement of methane with respect to that of water changes when the flow pattern is altered. My results also illustrate the importance of the capillary force, due to the formation of water bridges across the clay pores, not only on the fluid flow, but also on the pore structure, in particular its width. When the water bridges are broken, perhaps because of fast fluid flow, the capillary force vanishes leading to significant pore expansion. Because muscovite has similar structure to

illite, a clay often found in shale rocks, these results advance my understanding regarding the mechanism of water and gas transport in tight shale gas formations.

Finally, in Chap. 6 I provide a comprehensive conclusion about the work presented in this thesis and the outlook. Note that in Appendix A and B, I provide the supplemental information to support the work presented in Chap. 4. In particular, in Appendix A, I provide the research on the polarizability effects in molecular dynamics simulations of the graphene/water interface. In Appendix B I report the additional details for the numerical integration of the Poisson equation.

## References


1. Duan, C., Wang, W., & Xie, Q. (2013). Review article: Fabrication of nanofluidic devices. *Biomicrofluidics, 7*(2), 026501.
2. Sparreboom, W., van den Berg, A., & Eijkel, J. C. T. (2009). Principles and applications of nanofluidic transport. *Nature Nanotechnology, 4*(11), 713–720.
3. Yang, S. C. (2006). Effects of surface roughness and interface wettability on nanoscale flow in a nanochannel. *Microfluidics and Nanofluidics, 2*(6), 501–511.
4. Neto, C., Evans, D. R., Bonaccurso, E., Butt, H. J., & Craig, V. S. J. (2005). Boundary slip in Newtonian liquids: A review of experimental studies. *Reports on Progress in Physics, 68*(12), 2859–2898.
5. Karnik, R., Castelino, K., Duan, C. H., & Majumdar, A. (2006). Diffusion-limited patterning of molecules in nanofluidic channels. *Nano Letters, 6*(8), 1735–1740.
6. Stein, D., Kruithof, M., & Dekker, C. (2004). Surface-charge-governed ion transport in nanofluidic channels. *Physical Review Letters, 93*(3), 035901.
7. Chang, H. C., & Yossifon, G. (2009). Understanding electrokinetics at the nanoscale: A perspective. *Biomicrofluidics, 3*(1), 012001.
8. Berezhkovskii, A., & Hummer, G. (2002). Single-file transport of water molecules through a carbon nanotube. *Physical Review Letters, 89*(6), 064503.
9. Eijkel, J. C. T., & van den Berg, A. (2005). Nanofluidics: What is it and what can we expect from it? *Microfluidics and Nanofluidics, 1*(3), 249–267.
10. Sparreboom, W., van den Berg, A., & Eijkel, J. C. T. (2010). Transport in nanofluidic systems: A review of theory and applications. *New Journal of Physics, 12*, 015004.
11. Thomas, M., Corry, B., & Hilder, T. A. (2014). What have we learnt about the mechanisms of rapid water transport, ion rejection and selectivity in nanopores from molecular simulation? *Small (Weinheim an der Bergstrasse, Germany), 10*(8), 1453–1465.
12. Cottin-Bizonne, C., Cross, B., Steinberger, A., & Charlaix, E. (2005). Boundary slip on smooth hydrophobic surfaces: Intrinsic effects and possible artifacts. *Physical Review Letters, 94*(5), 056102.
13. Ho, T. A., Papavassiliou, D. V., Lee, L. L., & Striolo, A. (2011). Liquid water can slip on a hydrophilic surface. *Proceedings of the National Academy of Sciences USA, 108*(39), 16170–16175.
14. Huang, D. M., Sendner, C., Horinek, D., Netz, R. R., & Bocquet, L. (2008). Water slippage versus contact angle: A quasiuniversal relationship. *Physical Review Letters, 101*(22), 226101.
15. Kannam, S. K., Todd, B. D., Hansen, J. S., & Daivis, P. J. (2011). Slip flow in graphene nanochannels. *The Journal of Chemical Physics, 135*(14), 144701.
16. Kannam, S. K., Todd, B. D., Hansen, J. S., & Daivis, P. J. (2012). Slip length of water on graphene: Limitations of non-equilibrium molecular dynamics simulations. *The Journal of Chemical Physics, 136*(2), 024705–024713.

17. Maali, A., Cohen-Bouhacina, T., & Kellay, H. (2008). Measurement of the slip length of water flow on graphite surface. *Applied Physics Letters, 92*(5), 053101.
18. Martini, A., Hsu, H.-Y., Patankar, N. A., & Lichter, S. (2008). Slip at high shear rates. *Physical Review Letters, 100*(20), 206001.
19. Martini, A., Roxin, A., Snurr, R. Q., Wang, Q., & Lichter, S. (2008). Molecular mechanisms of liquid slip. *Journal of Fluid Mechanics, 600*(1), 257.
20. Zhu, Y., & Granick, S. (2001). Rate-dependent slip of Newtonian liquid at smooth surfaces. *Physical Review Letters, 87*(9), 096105.
21. Lauga E., Brenner, M., & Stone H. (2007) *Handbook of experimental fluid dynamics.* New York: Springer.
22. Craig, V. S. J., Neto, C., & Williams, D. R. M. (2001). Shear-dependent boundary slip in an aqueous Newtonian liquid. *Physical Review Letters, 87*(5), 054504.
23. Barrat, J. L., & Bocquet, L. (1999). Large slip effect at a nonwetting fluid-solid interface. *Physical Review Letters, 82*(23), 4671–4674.
24. Kannam, S. K., Todd, B. D., Hansen, J. S., & Daivis, P. J. (2013). How fast does water flow in carbon nanotubes? *The Journal of Chemical Physics, 138*(9), 094701.
25. Whitby, M., Cagnon, L., Thanou, M., & Quirke, N. (2008). Enhanced fluid flow through nanoscale carbon pipes. *Nano Letters, 8*(9), 2632–2637.
26. Majumder, M., Chopra, N., Andrews, R., & Hinds, B. J. (2005). Nanoscale hydrodynamics: Enhanced flow in carbon nanotubes. *Nature, 438*(7070), 44.
27. Holt, J. K., et al. (2006). Fast mass transport through sub-2-nanometer carbon nanotubes. *Science, 312*(5776), 1034–1037.
28. Thomas, J. A., McGaughey, A. J. H., & Kuter-Arnebeck, O. (2010). Pressure-driven water flow through carbon nanotubes: Insights from molecular dynamics simulation. *International Journal of Thermal Sciences, 49*(2), 281–289.
29. Koumoutsakos, P., Jaffe, R. L., Werder, T., & Walther, J. H. (2003). On the validity of the no-slip condition in nanofluidics. *Nanotech, 1*, 148–151.
30. Hummer, G., Rasaiah, J. C., & Noworyta, J. P. (2001). Water conduction through the hydrophobic channel of a carbon nanotube. *Nature, 414*(6860), 188–190.
31. Suk, M. E., & Aluru, N. R. (2010). Water transport through ultrathin graphene. *The Journal of Physical Chemistry Letters, 1*(10), 1590–1594.
32. Fornasiero, F., et al. (2008). Ion exclusion by sub-2-nm carbon nanotube pores. *Proceedings of the National Academy of Sciences USA, 105*(45), 17250–17255.
33. Corry, B. (2008). Designing carbon nanotube membranes for efficient water desalination. *The Journal of Physical Chemistry B, 112*(5), 1427–1434.
34. Cohen-Tanugi, D., & Grossman, J. C. (2012). Water desalination across nanoporous graphene. *Nano Letters, 12*(7), 3602–3608.
35. Sint, K., Wang, B., & Král, P. (2008). Selective ion passage through functionalized graphene nanopores. *Journal of the American Chemical Society, 130*(49), 16448–16449.
36. He, Z., Zhou, J., Lu, X., & Corry, B. (2013). Bioinspired graphene nanopores with voltage-tunable ion selectivity for Na+ and K+. *ACS Nano, 7*(11), 10148–10157.
37. Hilder, T. A., Yang, R., Gordon, D., Rendell, A. P., & Chung, S.-H. (2012). Silicon carbide nanotube as a chloride-selective channel. *The Journal of Physical Chemistry C, 116*(7), 4465–4470.
38. Song, C., & Corry, B. (2009). Intrinsic ion selectivity of narrow hydrophobic pores. *The Journal of Physical Chemistry B, 113*(21), 7642–7649.
39. Joly, L., Ybert, C., Trizac, E., & Bocquet, L. (2004). Hydrodynamics within the electric double layer on slipping surfaces. *Physical Review Letters, 93*(25), 257805.
40. Cipolla, C. L., Lolon, E., & Mayerhofer, M. J. (2009). *Reservoir modeling and production evaluation in shale-gas reservoirs*. International Petroleum Technology Conference.
41. King, G. E. Hydraulic fracturing 101: What every representative, environmentalist, regulator, reporter, investor, university researcher, neighbor, and engineer should know about hydraulic fracturing risk.

42. Boyer, C., Kieschnick, J., Suarez-Rivera, R., Lewis, R., & Water, G. (2006). Producing gas from its source. *Oilfield Review 18*(3), 36–49
43. King, G. E. (2010). Thirty years of gas shale fracturing: What have we learned? *SPE-133456-MS*.
44. Passey, Q. R., Bohacs, K., Esch, W. L., Klimentidis, R., & Sinha, S. (2010). From oil-prone source rock to gas-producing shale reservoir—geologic and petrophysical characterization of unconventional shale gas reservoirs. *SPE-133456-MS*.
45. Wang, F. P., & Reed, R. M. (2009). Pore networks and fluid flow in gas shales. *SPE-133456-MS*.
46. Berman, A., & Pittinger, L. F. (2011). US shale gas: Less abundance, higher cost. *The Oil Drum* http://nowandfutures.com/large/shale_gas_depletion(oildrum)8212.html
47. Gasparik, M., et al. (2014). Geological controls on the methane storage capacity in organic-rich shales. *International Journal of Coal Geology, 123*, 34–51.
48. Heller, R., & Zoback, M. (2014). Adsorption of methane and carbon dioxide on gas shale and pure mineral samples. *Journal of Unconventional Oil and Gas Resources, 8*, 14–24.
49. Vandenbroucke, M., & Largeau, C. (2007). Kerogen origin, evolution and structure. *Organic Geochemistry, 38*(5), 719–833.
50. Javadpour, F., Fisher, D., & Unsworth., M. Nanoscale gas flow in shale gas sediments. *Journal of Canadian Petroleum Technology, 46*(10).
51. Ziarani, A. S., & Aguilera, R. (2011). Knudsen's permeability correction for tight porous media. *Transport in Porous Media, 91*(1), 239–260.
52. Jin, Z., & Firoozabadi, A. (2015). Flow of methane in shale nanopores at low and high pressure by molecular dynamics simulations. *The Journal of Chemical Physics, 143*(10), 104315.
53. Zhang, P., Hu, L., Meegoda, J. N., & Gao, S. (2015). Micro/nano-pore network analysis of gas flow in shale matrix. *Scientific Reports, 5*, 13501.
54. Klinkenberg, L. J. (1941). *The permeability of porous media to liquids and gases*. American Petroleum Institute. Drilling and Production Practice, New York.
55. Firouzi, M., Alnoaimi, K., Kovscek, A., & Wilcox, J. (2014). Klinkenberg effect on predicting and measuring helium permeability in gas shales. *International Journal of Coal Geology, 123*, 62–68.
56. Bhatia, S. K., Bonilla, M. R., & Nicholson, D. (2011). Molecular transport in nanopores: A theoretical perspective. *Physical Chemistry Chemical Physics: PCCP, 13*(34), 15350–15383.
57. Collell, J., et al. (2015). Transport of multicomponent hydrocarbon mixtures in shale organic matter by molecular simulations. *The Journal of Physical Chemistry C, 119*(39), 22587–22595.
58. Wang, S., Javadpour, F., & Feng, Q. (2016). Molecular dynamics simulations of oil transport through inorganic nanopores in shale. *Fuel, 171*, 74–86.
59. He, S., Jiang, Y., Conrad, J. C., & Qin, G. (2015). Molecular simulation of natural gas transport and storage in shale rocks with heterogeneous nano-pore structures. *Journal of Petroleum Science and Engineering, 133*, 401–409.
60. Ungerer, P., Collell, J., & Yiannourakou, M. (2015). Molecular modeling of the volumetric and thermodynamic properties of kerogen: Influence of organic type and maturity. *Energy & Fuels, 29*(1), 91–105.
61. Kelemen, S. R., et al. (2007). Direct characterization of kerogen by X-ray and solid-state 13C nuclear magnetic resonance methods. *Energy & Fuels, 21*(3), 1548–1561.
62. Bousige, C., et al. (2016). Realistic molecular model of kerogen's nanostructure. *Nature Materials, 15*, 576–582.
63. Falk, K., Coasne, B., Pellenq, R., Ulm, F.-J., & Bocquet, L. (2015). Subcontinuum mass transport of condensed hydrocarbons in nanoporous media. *Nature Communications, 6*, 6949.
64. Ho, T. A., Criscenti, L. J., & Wang, Y. (2016). Nanostructural control of methane release in kerogen and its implications to wellbore production decline. *Scientific Reports, 6*, 28053.

65. Castrillon, S. R. V., Giovambattista, N., Aksay, I. A., & Debenedetti, P. G. (2009). Effect of surface polarity on the structure and dynamics of water in nanoscale confinement. *The Journal of Physical Chemistry B, 113*(5), 1438–1446.
66. Gordillo, M. C., & Marti, J. (2008). Structure of water adsorbed on a single graphene sheet. *Physical Review B, 78*(7), 075432.
67. Argyris, D., Tummala, N. R., Striolo, A., & Cole, D. R. (2008). Molecular structure and dynamics in thin water films at the silica and graphite surfaces. *Journal of Physical Chemistry C, 112*(35), 13587–13599.
68. Argyris, D., Cole, D. R., & Striolo, A. (2009). Hydration structure on crystalline silica substrates. *Langmuir, 25*(14), 8025–8035.
69. Wang, J. W., Kalinichev, A. G., & Kirkpatrick, R. J. (2009). Asymmetric hydrogen bonding and orientational ordering of water at hydrophobic and hydrophilic surfaces: A comparison of water/vapor, water/talc, and water/mica interfaces. *Journal of Physical Chemistry C, 113*(25), 11077–11085.
70. Van der Spoel, D., et al. (2005). GROMACS: Fast, flexible, and free. *Journal of Computational Chemistry, 26*(16), 1701–1718.
71. Plimpton, S. (1995). Fast parallel algorithms for short-range molecular-dynamics. *Journal of Computational Physics, 117*(1), 1–19.
72. Frenkel, D., & Smit, B. (2002). *Understanding molecular simulation from algorithms to applications*. New York: Academic Press.
73. Greathouse, J. A., Kinnibrugh, T. L., & Allendorf, M. D. (2009). Adsorption and separation of noble gases by IRMOF-1: Grand canonical Monte Carlo simulations. *Industrial and Engineering Chemistry Research, 48*(7), 3425–3431.

# Chapter 2
# Methodology

## 2.1 Basic Background of Molecular Dynamics Simulation

Molecular dynamics simulation solves Newton's second law of motion for each atom $\sum_j \boldsymbol{F_{ij}} = m_i \frac{\mathrm{d}^2 \boldsymbol{r_i}}{\mathrm{d}t^2}$, where $m_i$, $\mathbf{r_i}$, t, and $\mathbf{F_{ij}}$ are atomic mass, position of atom i, time, and force between atoms i and j, respectively. The equation of motion is usually integrated with the random initial configurations and initial velocities calculated from Boltzmann distribution [1]. Solving the equation of motion requires the input of atomic mass, time step, and force. While it is straightforward to provide atomic mass and time step (e.g., 1 fs) the determination of the force between atom i and j requires special care because MD simulation results strongly depend on the applied force field. The force $\mathbf{F}$ is calculated from the interaction potential $V_{ij}$ as $\boldsymbol{F_{ij}} = -\nabla_i V_{ij}$.

### *2.1.1 Force Field*

In my simulations, non-bonded potential energy is described as:

$$V_{ij} = 4\varepsilon_{ij}\left[\left(\frac{\delta_{ij}}{r_{ij}}\right)^{12} - \left(\frac{\delta_{ij}}{r_{ij}}\right)^{6}\right] + f\frac{q_i q_j}{\varepsilon_r r_{ij}} \tag{2.1}$$

The first terms in the right-hand side of Eq. (2.1) describe Lennard-Jones (LJ) interaction. The second terms in the right-hand side of Eq. (2.1) describe electrostatic potentials. The cross LJ interaction between unlike species is given by the Lorentz-Berthelot mixing rules: $\sigma_{ij} = \frac{\sigma_{ii} + \sigma_{jj}}{2}$ and $\varepsilon_{ij} = \sqrt{\varepsilon_{ii}\varepsilon_{jj}}$. The calculation of the non-bonded interactions is the most time consuming step in molecular dynamics



T.A. Ho, *Nanoscale Fluid Transport*, Springer Theses,
DOI 10.1007/978-3-319-47003-0_2

simulation. To speed up the computation, the interactions between two atoms separated by a distance greater than the cutoff distance are ignored. While this approach works well for the Lennard-Jones interaction it is not suitable to implement for the system where charged atoms are present because of the significance of the long-range electrostatic interaction. The most popular method to approximate the electrostatic interaction is to partition it into a long-range component and a short-range component. The short-range component is calculated following Eq. (2.1) in real space and the long-range one is estimated in Fourier space using different approaches including Ewald, particle-mesh Ewald (PME), and Particle-Particle Particle-Mesh methods [1]. These methods require less computer time compared to the direct summation using Eq. (2.1). In my simulations I usually implement PME algorithm to calculate the long-range electrostatic interaction.

As water is present in all of my simulated systems selecting the good water model is critical to simulation results. There are a lot of models available in literature including SPC [2], SPC/E [3], TIP4P/2005 [4], TIP3P [5], TIP5P [6], TIP4P/2005f [7], and SWM4_NDP [8] water models. SPC and SPC/E are the three sites rigid water models. Partial charges are assigned to oxygen and hydrogen atoms, while the center of LJ interactions is the oxygen atom. When the rigid SPC/E model is implemented, the two O–H bonds and the fictitious H–H bond lengths were constrained using the SHAKE algorithm [9]. TIP4P/2005 is a four sites rigid model. The oxygen atom carries no charge and is the center of LJ interaction. Partial charges are assigned to each hydrogen atom and to a dummy atom M located along the bisector of the HOH angle. TIP5P is a rigid five-sites water model. A partial charge is placed on each hydrogen atom, and partial charges of equal magnitude and opposite sign are placed on two lone-pair interaction sites. The oxygen atom has no charge and it functions as the center of LJ interactions. TIP3P is a three-sites rigid water model. It was developed to improve the energy and density for liquid water [5]. TIP4P/2005f is the flexible version TIP4P/2005 water model [7]. The O–H bond and HOH angle are allowed to vibrate in this water models. SWM4_DP is a polarizable water model with four sites and Drude polarizability. The oxygen atom is the center of LJ interactions. The charge distribution is represented by three point charges: two hydrogen sites and one additional site positioned along the HOH bisector. Electronic induction is described by introducing a classical charged Drude particle attached to the oxygen by a harmonic spring. The oxygen atom carries a partial charge equal and opposite that of the Drude particle.

In my thesis, because I study the structural and dynamical properties of interfacial water the selected water model is expected to reproduce, at least the properties of bulk water. Mark and Nilsson [10], in the study of the structure and dynamics of the TIP3P, SPC, SPC/E water models at 297 K, compared the radial distribution function $g_{OO}$, $g_{OH}$, and $g_{HH}$ (i.e., a common property used to study structure of liquid water) and self-diffusion coefficients with experimental data. They reported that SPC/E model give the best bulk water dynamics and structure and SPC and TIP3P water models predict less water structure and faster diffusion when compared with experimental data. Pusztai et al. [11] compared the radial

**Table 2.1** Self-diffusion coefficients ($10^{-5}$ $cm^2/s$) reported for some popular water models

| $H_2O$ | SPC | SPC/E | TIP3P | TIP5P | TIP4P/2005 | TIP4P/2005f | SWM4-NDP |
|---|---|---|---|---|---|---|---|
| D | 3.85 [13] | 2.49 [13] | 5.13 [13] | 2.62 [13] | 2.08 [4] | 1.93 [7] | 2.33 [8] |

distribution function of water models including SPC/E, TIP4P, TIP4P-2005 with the neutron diffraction data and reported that the structure of liquid water predicted using these water models are reasonable when compared with experimental data. For SWM4-NDP water model, while the radial distribution function $g_{OO}$ is consistent with experimental data the $g_{OH}$ and $g_{HH}$ are slightly different from experimental results [8]. In the Table 2.1 I compare the self-diffusion coefficients reported for some popular water models. For comparison, the self-diffusion coefficient obtained from experiment is $2.3 \times 10^{-5}$ $cm^2/s$ [12].

Among the popular water models mentioned SWM4-NDP reproduces the best experimental data of self-diffusion coefficient. While SPC, TIP3P, and TIP5P models overestimate TIP4P/2005 and TIP4P/2005f models underestimate the self-diffusion coefficient of water. Self-diffusion coefficient predicted using SPC/E model is slightly higher than experimental result.

A good water model is the model that reproduces all the properties of water molecules (e.g., dipole moment, dielectric constant, density, self-diffusion coefficient, radial distribution function, heat capacity, and phase diagram…). No water model in literature can reproduce all of these properties [14]. Because SPC/E is a simple (3 rigid sites) water model that reproduces well the experimental structure (i.e., radial distribution function $g_{OO}$, $g_{OH}$, and $g_{HH}$ [10]), and self-diffusion coefficient of water [13] at ambient conditions it is the model of choice in my simulation.

Molecular dynamics simulation results strongly depend on the force field describing the interactions among various constituents in the simulated system. For example, in one of my publications [15] I compare the water properties predicted on the crystalline silica substrate. I implement four different force fields to describe the silica surface. These force fields yield different orientation and flexibility of surface hydrogen atoms, and also different interaction potentials with water molecules. My results indicate the dependence of both structural and dynamical properties on the force field implemented. Comparison with experimental data is therefore necessary to discriminate the accuracy of implemented force fields. In this thesis, where this comparison is possible I will provide in details.

### *2.1.2 Algorithm*

Solving the equation of motion requires the calculation of the pair-wise potential energy for all the atoms in the system. Due to the complicated nature of this

calculation, there is no analytical solution to the equations of motion. Therefore, a numerical method is applied. Numerous numerical algorithms have been developed to integrate the equations of motion including Verlet and leap-frog [1].

In my simulations I usually apply leap-frog algorithm to solve Newton's equations of motion. According to this algorithm, the position and velocity are described as follow:

$$r(t+\delta t) = r(t) + v(t+\frac{1}{2}\delta t)\delta t \tag{2.2}$$

$$v\left(t+\frac{1}{2}\delta t\right) = v\left(t-\frac{1}{2}\delta t\right) + \frac{F(t)}{m}\delta t \tag{2.3}$$

In Eq. (2.3) the velocities are calculated at time $t+\frac{1}{2}\delta t$. These are then used to calculate the positions $r$ at time $t+\delta t$. In this way, the velocities leap over the positions, then the positions leap over the velocities. The velocities at time $t$ can be approximated by Eq. (2.4):

$$v(t) = \frac{1}{2}\left[v\left(t+\frac{1}{2}\delta t\right) + v\left(t-\frac{1}{2}\delta t\right)\right] \tag{2.4}$$

### *2.1.3 Themostat*

By simply solving the Newtonian equation of motion for all atoms in the system the NVE ensemble (i.e., microcanonical ensemble in which the number of atom, volume, energy are constant) is generated. Because molecular dynamics simulation results are expected to be compared with the experimental data, which are usually obtained at constant temperature, the NVT ensemble (i.e., canonical ensemble in which the number of atom, volume, temperature are constant) must be generated. Another reason I need to control the temperature, although it is not from the thermodynamic standpoint, is because of the numerical errors from MD simulation algorithm. Using thermostat can avoid steady energy drift from equilibrium state. Several thermostat methods are available in the literature including Andersen, Berendsen, Nose-Hoover [1]. For example, in Andersen thermostat the velocities of particles at each time step are reassigned the new values chosen from Maxwell-Boltzmann distribution [1, 16]. While this method requires no direct modification of the integration of equation of motion [16] it disturbs the velocity time correlations and slow down the kinetics of the system [1, 16]. Therefore, it should not be used to study dynamical properties. In Berendsen thermostat the deviation of the system temperature from target temperature $T_0$ is corrected slowly as $\frac{dT}{dt} = \frac{T_0 - T(t)}{\tau}$, where $\tau$ is the time constant. This approach does not yield a true canonical ensemble. However, when the system is large enough most of the

ensemble averages is not remarkably affected, except the kinetic energy distribution [1]. In the widely used Nose-Hoover thermostat the equation of motion is modified as: $\frac{d^2 r_i}{dt^2} = \frac{F_i}{m_i} - \frac{p_\zeta}{Q}\frac{dr_i}{dt}$. The friction parameter $\zeta$ is a dynamic quantity and its equation of motion is described as: $\frac{dp_\zeta}{dt} = (T - T_0)$. In my simulation I apply Noose-Hover thermostat because it allows one to rigorously generate a correct canonical ensemble [1].

Most of the equilibrium MD simulation results are quantified after equilibrium is established. To verify if the simulated system is equilibrated, temperature, structural and dynamical properties are monitored as a function of time. Equilibrium state is considered to be obtained when these properties do not change with simulation time.

### *2.1.4 Periodic Boundary Condition*

Periodic boundary conditions enable a large (infinite) system to be simulated using a small simulation box containing the atoms of interest. MD simulation algorithm is developed in a way that the central box is surrounded by its images in all directions. Atom in the central box interacts not only with the atoms in the same box but also with the atoms in the image box. In this way, the atoms in simulated box experience the forces as they are in large system. In my simulation I use cubic box and apply periodic boundary condition in all directions.

## 2.2 Non-equilibrium Simulation

In Fig. 2.1 I present two types of flow geometry implemented in this thesis to study the transport of fluids inside nanochannels. The first type is the Couette flow (top panel) [17], in which the atoms belonging to the top surface are driven at a constant

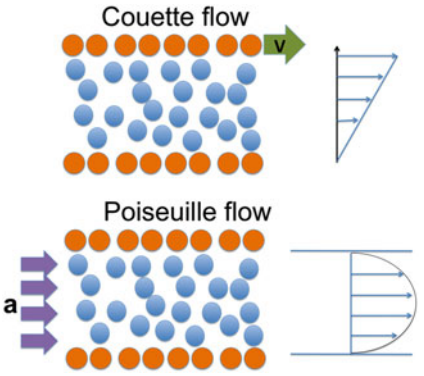


**Fig. 2.1** Schematic drawing showing the Couette (*top*) and Poiseuille (*bottom*) flow geometries used in my non-equilibrium simulations

velocity and the atoms belonging to the bottom surface are kept stationary. The typical velocity profile for this flow is shown in the top right panel. The second type is the Poiseuille flow (bottom panel), in which accelerations are applied to fluid atoms to force them to move in a specific direction [18]. The surfaces in Poiseuille flow geometry are kept stationary. The characteristic velocity profile of the Poiseuille flow is provided in bottom right panel. The non-equilibrium simulations are conducted until the velocity profile does not change with time (steady state flow).

In non-equilibrium MD simulations, the applied velocity in Couette geometry and the applied acceleration in Poiseuille flow are very large compared to those encountered in experiments. This is due to computing power limitations [18, 19]. However, because it has been reported that the time scale for fluid flow scales linearly with the applied acceleration [20, 21], and because many non-equilibrium MD simulation results are consistent with the experimental data [21, 22], I expect that reliable data can be obtained using non-equilibrium MD simulation.

Two approaches are usually used to control the temperature in non-equilibrium simulation: thermostat is coupled to all atoms in the system and thermostat is coupled only to the surfaces. In the later case, confined fluids exchange heat with the wall during the course of the simulation [23]. In my simulation I apply the former case. When implementing this algorithm it is essential to subtract the nonzero streaming velocity in the direction of the flow when calculating the kinetic energy. However, because the streaming velocity is un-known, only the velocity component perpendicular to the flow direction is usually thermostatted [24]. Since my streaming velocity is very small compared to the thermal velocity I include the streaming velocity in my temperature calculations. This will not result in significant error because small streaming velocity contributes only a tiny fraction of the total kinetic energy [25, 26]. Also, as demonstrated by Khare et al. [27], the differences in the temperature profiles expected at the shear rate considered in the this thesis are minimal and only present at the centre of the channel, the structure of interfacial water will not depend on the thermostat, and the conclusions in this thesis will hold independently on the algorithm considered.

The most common results presented in this thesis are the density and velocity profiles. In the left panel of Fig. 2.2 I show the schematic drawing presenting my

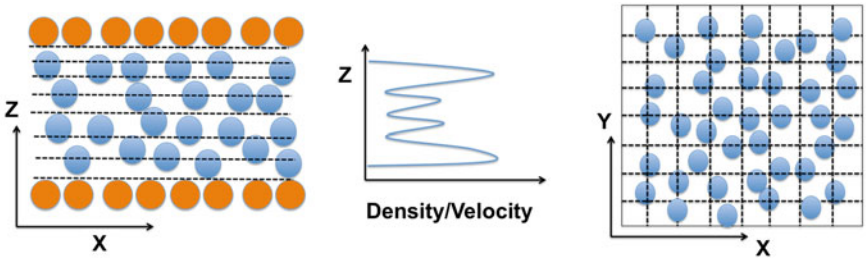


**Fig. 2.2** Schematic drawing showing the algorithm to calculate the profiles

algorithm to compute the velocity/density profiles as a functions of position in between two substrates. I divide the volume into bins that spans entire length of simulation box in X and Y directions, and 1 Å along the Z direction (dashed line). I then average the properties of the atoms in each bin over time. The averaged properties are plotted as a function of position z as shown in the middle panel. In the right panel of Fig. 2.2 I report the schematic drawing presenting my algorithm to calculate the planar density distribution, for example the distribution of water in the first hydration layer on the plane parallel to the surface. In this calculation, only the water in the layer of interest is taken into account. I divide the volume into small box of $1 \times 1$ Å$^2$ in XY plane and average the density inside each box over time. The density is then plotted in a 3D contour plot. For other properties reported in this thesis where the algorithm is applied I will provide in details.

## References


1. Van der Spoel, D., et al. (2005). GROMACS: Fast, flexible, and free. *Journal of Computational Chemistry, 26*(16), 1701–1718.
2. Berendsen, H. J. C., Postma, J. P. M., Van Gunsteren, W. F., & Hermans, J. (1981). *Intermolecular forces*. Dordrecht: Reidel.
3. Berendsen, H. J. C., Grigera, J. R., & Straatsma, T. P. (1987). The missing term in effective pair potentials. *Journal of Physical Chemistry, 91*(24), 6269–6271.
4. Abascal, J. L. F., & Vega, C. (2005). A general purpose model for the condensed phases of water: TIP4P/2005. *The Journal of Chemical Physics, 123*(23), 234505.
5. Jorgensen, W. L., Chandrasekhar, J., Madura, J. D., Impey, R. W., & Klein, M. L. (1983). Comparison of simple potential functions for simulating liquid water. *The Journal of Chemical Physics, 79*(2), 926–935.
6. Mahoney, M. W., & Jorgensen, W. L. (2000). A five-site model for liquid water and the reproduction of the density anomaly by rigid, nonpolarizable potential functions. *The Journal of Chemical Physics, 112*(20), 8910–8922.
7. Gonzalez, M. A., & Abascal, J. L. F. (2011). A flexible model for water based on TIP4P/2005. *The Journal of Chemical Physics, 135*(22), 224516–224523.
8. Lamoureux, G., Harder, E., Vorobyov, I. V., Roux, B., & MacKerell, A. D. (2006). A polarizable model of water for molecular dynamics simulations of biomolecules. *Chemical Physics Letters, 418*(1–3), 245–249.
9. Ryckaert, J.-P., Ciccotti, G., & Berendsen, H. (1977). Numerical integration of the cartesian equations of motion of a system with constraints: Molecular dynamics of n-alkanes. *Journal of Computational Physics, 23*(3), 327–341.
10. Mark, P., & Nilsson, L. (2001). Structure and dynamics of the TIP3P, SPC, and SPC/E water models at 298 K. *Journal of Physical Chemistry A, 105*(43), 9954–9960.
11. Pusztai, L., Pizio, O., & Sokolowski, S. (2008). Comparison of interaction potentials of liquid water with respect to their consistency with neutron diffraction data of pure heavy water. *The Journal of Chemical Physics, 129*(18), 184103.
12. Krynicki, K., Green, C. D., & Sawyer, D. W. (1978). Pressure and temperature-dependence of self-diffusion in water. *Faraday Discussions, 66*, 199–208.
13. Mahoney, M. W., & Jorgensen, W. L. (2001). Diffusion constant of the TIP5P model of liquid water. *The Journal of Chemical Physics, 114*(1), 363–366.
14. Vega, C., & Abascal, J. L. F. (2011). Simulating water with rigid non-polarizable models: A general perspective. *Physical Chemistry Chemical Physics: PCCP, 13*(44), 19663–19688.

15. Ho, T. A., et al. (2011). Interfacial water on crystalline silica: A comparative molecular dynamics simulation study. *Molecular Simulation, 37*(3), 172–195.
16. Basconi, J. E., & Shirts, M. R. (2013). Effects of temperature control algorithms on transport properties and kinetics in molecular dynamics simulations. *Journal of Chemical Theory and Computation, 9*(7), 2887–2899.
17. Thompson, P. A., & Troian, S. M. (1997). A general boundary condition for liquid flow at solid surfaces. *Nature, 389*(6649), 360.
18. Lauga, E., Brenner, M., & Stone, H. (2007). *Handbook of experimental fluid dynamics*. New York: Springer.
19. Ho, T. A., Papavassiliou, D. V., Lee, L. L., & Striolo, A. (2011). Liquid water can slip on a hydrophilic surface. *Proceedings of the National Academy of Sciences, 108*(39), 16170–16175.
20. Cohen-Tanugi, D., & Grossman, J. C. (2012). Water Desalination across nanoporous graphene. *Nano Letters, 12*(7), 3602–3608.
21. Holt, J. K., et al. (2006). Fast mass transport through sub-2-nanometer carbon nanotubes. *Science, 312*(5776), 1034–1037.
22. Whitby, M., & Quirke, N. (2007). Fluid flow in carbon nanotubes and nanopipes. *Nature Nanotechnology, 2*(2), 87–94.
23. Toton, D., Lorenz, C. D., Rompotis, N., Martsinovich, N., & Kantorovich, L. (2010). Temperature control in molecular dynamic simulations of non-equilibrium processes. *Journal of Physics: Condensed Matter, 22*(7), 074205.
24. Zhu, W., Singer, S. J., Zheng, Z., & Conlisk, A. T. (2005). Electro-osmotic flow of a model electrolyte. *Physical Review E, 71*(4), 041501.
25. Freund, J. B. (2002). Electro-osmosis in a nanometer-scale channel studied by atomistic simulation. *The Journal of Chemical Physics, 116*(5), 2194–2200.
26. Qiao, R., & Aluru, N. R. (2003). Ion concentrations and velocity profiles in nanochannel electroosmotic flows. *The Journal of Chemical Physics, 118*(10), 4692–4701.
27. Khare, R., de Pablo, J., & Yethiraj, A. (1997). Molecular simulation and continuum mechanics study of simple fluids in non-isothermal planar couette flows. *The Journal of Chemical Physics, 107*(7), 2589–2596.

# Chapter 3
# Correlation Between Interfacial Water Properties and Hydrodynamic Boundary Conditions

## 3.1 Introduction

Molecular-level understanding of hydrophobic effects including protein folding [1], micelle and cellular membrane formation [2], and frictionless flow of water through carbon nanotube membranes [3–5] is a scientific challenge. A now famous 2008 commentary by Granick and Bae [6] initiated a scientific discussion to identify the molecular signature of hydrophobic vs. hydrophilic surfaces. The question is whether or not molecular properties exist for interfacial water molecules that change with the surface 'degree of hydrophobicity'. Identifying such properties and their macroscopic consequences, in particular, could advance practical applications, e.g., designing self-cleaning surfaces, as well as fundamental scientific endeavours including understanding self-assembly [7].

Molecular simulations should allow the discovery of such molecular signatures because they allow a systematic variation of the properties of a surface, as well as of surface-water interactions [8]. Although the resultant substrates may not be realistic, the results are useful to interpret nature and to design innovative materials. It has so far been possible to relate some macroscopic observables to the degree of hydrophobicity (i.e., contact angle to adsorption free energy [9]). Garde and coworkers employed equilibrium molecular dynamics to determine a number of quantities, including local density, contact angle, and adsorption of small solutes for water near surfaces of varying degrees of hydrophobicity [10]. While the local water density provided unsatisfactory characterization, the probability of cavity formation was found to be large near hydrophobic and small near hydrophilic surfaces.



T.A. Ho, *Nanoscale Fluid Transport*, Springer Theses,
DOI 10.1007/978-3-319-47003-0_3

The present work focuses on the relation between one important macroscopic signature of hydrophobic surfaces, the hydrodynamic liquid slip, to molecular interfacial water properties. Flat surfaces are arbitrarily classified as hydrophobic when a water droplet yields a contact angle larger than 90°, hydrophilic otherwise. There are numerous evidences supporting for the fact that the hydrophobic surfaces tend to cause water slip [11–20]. Large liquid slip on hydrophobic surfaces could reduce the drag in vessels navigating the seas, the pressure drop encountered by fluids flowing inside pipes, and even repel ice formation. At nano length scale, liquid slip seems to appear when a fluid does not wet a surface [11, 19, 21–23] and the degree of slip depends on the surface roughness [19, 24]. Liquid slip is also found on micro-structured hydrophobic surfaces [25, 26]. On these textured surfaces, if the liquid completely penetrates into the rough grooves (Wenzel state) fluid adheres more strongly to the textured surface when compared to Cassie state (i.e., the liquid does not penetrate the grooves) [27]. In Cassie state liquid/solid interface actually consists of two interfaces: liquid/solid and liquid/vapour [28]. Liquid/vapour interface is the shear-free interface that offers liquid slip [29]. Since in Wenzel state liquid adheres strongly to the textured surface causing high contact angle hysteresis Cassie textured surface is usually preferred for some water repellent practical applications including self-cleaning surface [27]. Because the extent of slip varies systematically with the contact angle [13, 20, 30], in the case of water, slip should occur on hydrophobic surfaces [16]. However, in this study I present a surprising results demonstrating that water can slip on hydrophilic surface as well. Equilibrium and non-equilibrium MD simulations are employed to quantify the extent of water slip at various solid interfaces and search for molecular-level hydrophobic signatures.

## 3.2 Methodology

### *3.2.1 Surface Constructions*

The surface that I considered in this work is MgO. Its crystal structure is cubic with octahedral Mg and O. It is simulated by using the CLAYFF force field [31]. Many experimental results demonstrated that water dissociates on MgO surface to from surface hydroxyl group [32–34]. Because in my model water dissociation is not permitted, in general my simulated MgO surface is not realistic. However, by applying this simple MgO model I can easily alter the surface properties, a common approach applied in MD simulation to study how the strength of surface/water interaction and the surface morphology can affect interfacial water properties. I arbitrarily modify the MgO surface following two protocols. In the first protocol, I reduce the electrostatic interactions between water and the MgO surface atoms by a factor W, comprised between 0 and 1. When W = 1 I recover MgO. When W = 0 there is no partial charge on the surface atoms. In the second modification protocol I

maintain both dispersive and electrostatic surface-water interactions consistent with those of original MgO, but I reduce the lattice parameter that separates Mg and O atoms by a factor D. When D = 1 I recover MgO. As D decreases the surface atomic density increases.

### 3.2.2 Contact Angle Simulations

In Fig. 3.1 I show a representative equilibrium simulation snapshot to demonstrate the method to model contact angle of water droplet on a solid surface. A water droplet of 1000 water molecules was placed on the top of three surfaces MgO, W, and D that constructed following the method discussed above. In all cases, water molecules are described using the SPC/E model [35]. All simulations were conducted using LAMMPS [36], and performed in NVT ensemble (i.e., constant volume, number of particles, and temperature) at ambient conditions (T = 300 K). At equilibrium, the shape of the droplet insignificantly changes during the course of simulation. Following Ref. [37] a plane perpendicular to the surface and passing through the droplet centre of mass was identified. Along this plane the drop was sectioned in 0.5 Å wide bins used to calculate the atomic densities. The vacuum/water interface was defined when the water density decreases to 0.2 g/cm$^3$. The contact angle was determined at three point contact lines and was used to classify if the surface is hydrophilic or hydrophobic.

### 3.2.3 Couette Flow Simulations

In Fig. 3.2 I report, on the left panel, one simulation snapshot to illustrate the protocol implemented to determine the presence/absence of liquid slip. To investigate the presence/absence of liquid slip one could implement either the Couette or

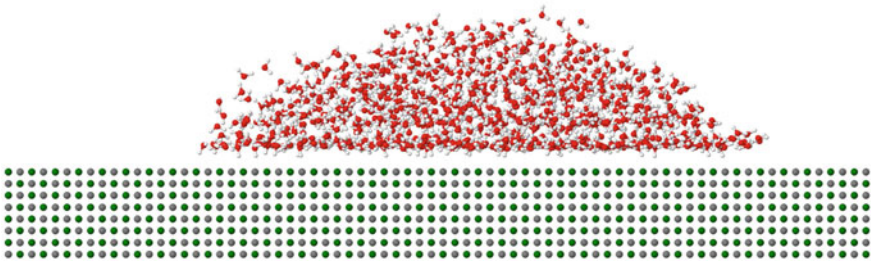

**Fig. 3.1** Simulation snapshot demonstrates the method used to determine the contact angle of water on solid surface. *Red* and *white* spheres represent water oxygen and hydrogen atoms, respectively. *Green* and *grey* spheres are the magnesium and oxygen atoms of the surface, respectively

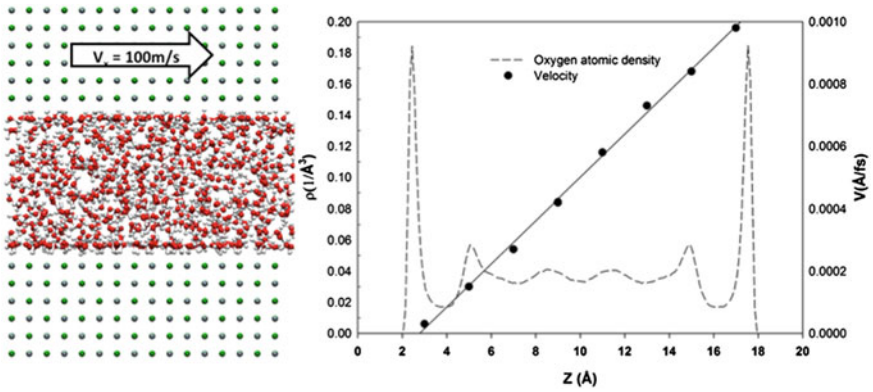


**Fig. 3.2** Simulation snapshot illustrating the protocol implemented to study the transport properties for confined water in a Couette flow (*left*). The bottom surface is maintained in its fixed position, while the top one is moved with constant velocity of 100 m/s (0.001 Å/fs) along the X direction. When the Couette flow is fully established I can study the density profile of the oxygen atoms of the confined water, as well as the velocity of the confined water molecules along the X direction as a function of their position within the narrow slit-shaped channel (*right*, example for MgO substrate). When the velocity of the water molecules in contact with the solid substrates equals that of the solid (as in the case of MgO) the simulations suggest no slip. On the contrary, when the water velocity in contact with the solid surface differs from that of the solid, hydrodynamic liquid slip is observed

the pressure-driven Poiseuille flow. Hydrodynamic slip is independent of the flow type [38]. Following Thompson and Troian [23], I simulated a Couette flow. Two parallel mirror-image solid surfaces are placed along the Z axis. The bottom surface is maintained at a fixed location. The top surface is displaced along the X direction with a constant velocity, $v_X$ = 100 m/s. Admittedly, the resultant shear rate, which is limited by the current state-of-the-art computational resources, is much higher than shear rates typically explored experimentally [39], yet comparable to those found in high performance lubrication applications such as rocket engines and computer disk drives [40]. Nevertheless, important insights can be attained from simulations, as shown, for example, by Martini et al. [18]. In most simulations reported here the atoms within the solid are maintained rigid. To ensure that this simplification does not introduce spurious effects [17], I conducted representative simulations in which the surface atoms vibrate, while maintaining the entire system at the desired temperature. No statistically significant differences were observed between the results obtained for MgO. The results presented also do not depend on the thermostat (Berendsen vs. Nose-Hoover). It should be pointed out that the Couette-type simulations are initiated after the thin film of water confined within the slit-shaped pores has been equilibrated at ambient conditions. Consequently, liquid water wets all surfaces considered in the non-equilibrium simulations discussed herein.

At steady states the water molecules confined in the gap between the two surfaces manifest a characteristic velocity profile [$v_{w,X}(z)$]. In the right panel of Fig. 3.2 I show the oxygen atomic density profile and the velocity profile for water molecules as a function of their Z position. The reference z = 0 is the centre atomic position of the top layer of the bottom surface. The slip velocity is defined as the velocity of the water in the first hydration layer [41]. The slip length $L_s$ is attained by extrapolating the velocity profiles from reference z = 0 to the distance at which the fluid velocity equals the surface velocity (i.e., $v_x = 0$ m/s) [42]. A small uncertainty is expected when estimating slip length because it depends on the definition of the wall position (reference z = 0). Sometime the position of the wall is taken at the centre of mass of the innermost layer of solid wall. Sometime it is taken at a distance of $\sigma$ (Van der Waals size of solid atom) away from the surface [15]. The temperature is maintained at 300 K, as in all other cases.

## 3.3 Results

In the top panels of Fig. 3.3 I report the water droplet profiles used to calculate the contact angles as W and D vary. The results indicate that the contact angle simulated on MgO surface (i.e., W = 1 or D = 1 surface) is $\sim 47°$ indicating a hydrophilic surface. When W decreases the MgO surface, originally hydrophilic, becomes hydrophobic. For example, when W = 0 the surface interacts with water molecules only via weak dispersive interactions, and the contact angle becomes $\sim 130°$ (bottom left panel), characteristic of a hydrophobic surface. The results also suggest that the contact angle changes non monotonically as D decreases, although remaining in all cases lower than 90° (consistent with hydrophilic surfaces), and reaches $\sim 30°$ when D = 0.62 (i.e., very hydrophilic surface). It is worth mentioning that the distance between Mg and O atoms in MgO is 0.21 nm, less than the diameter of one SPC/E water molecule. Thus all surfaces considered here are atomically smooth.

The non-monotonic dependence of the contact angle on the change in D can be explained based on the orientation of the water molecules at contact with the solid substrate, in qualitative agreement with the arguments proposed by Giovambattista et al. [37] and by Lee and Rossky [43]. To quantify these effects I report in Fig. 3.4 the density profiles for oxygen and hydrogen atoms of water molecules in the direction perpendicular to the solid substrates as D decreases from 1 to 0.62. The results are only shown up to 4 Å from the substrates.

When D = 1 (left) the first oxygen peak is found at z = 2.45 Å and two hydrogen peaks are found at z = 1.65 Å and z = 3.05 Å. The first hydrogen peak is closer to the surface than the first oxygen peak, indicating that, on average, one of the OH bonds of about half the water molecules belonging to the first hydration layer points towards the surface. Similar density distributions are found when D = 0.9 (second panel from left), suggesting that the orientation of water molecules does not change significantly when D changes from 1 to 0.9. However, the oxygen

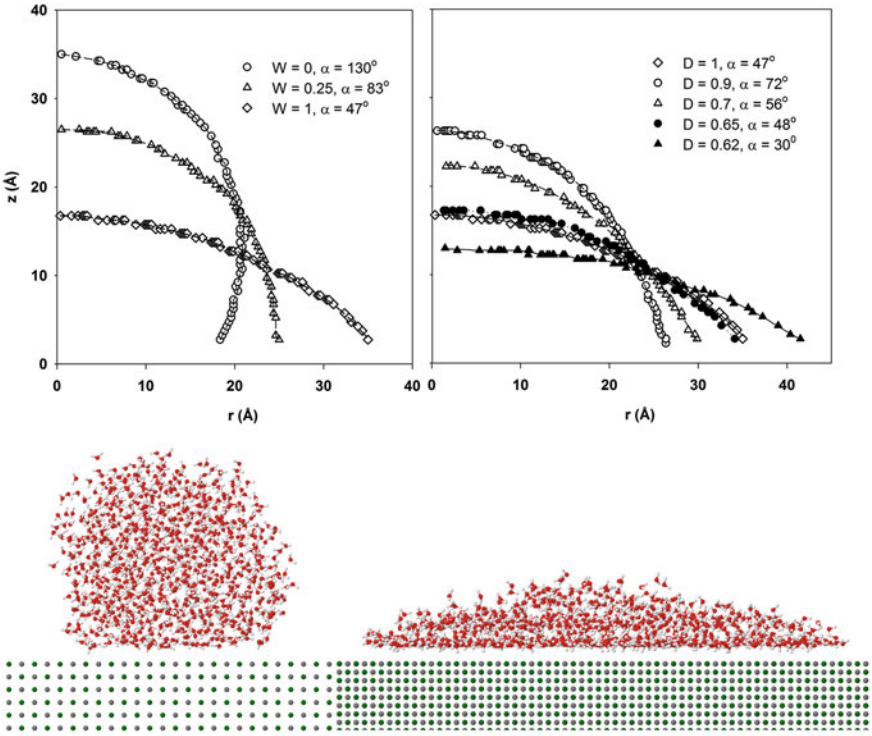


**Fig. 3.3** The drop profiles obtained from simulation of water droplets on the various surfaces considered. As W decreases (*top left*) the contact angle systematically increases. As D decreases (*top right*) the contact angle changes, but not monotonically. In general the substrates remain hydrophilic, but when D = 0.62 very hydrophilic surfaces are obtained. Simulation snapshots for the most hydrophobic (*bottom left*, W = 0, contact angle $\sim 130°$) and the most hydrophilic (*bottom right*, D = 0.62, contact angle $\sim 30°$) substrates considered herein

peak is found at z = 2.65 Å when D = 0.9, farther from the surface than the first oxygen peak on the D = 1 surface. The oxygen peak on the D = 0.9 surface is also broader and less intense than that on the D = 1 surface. These features suggest that interfacial water molecules are, to some extent, repelled from the surface when D is decreased from 1 to 0.9. As a consequence of this molecular-level repulsion the contact angle increases from $\sim 47°$ to $\sim 72°$, as shown in Fig. 3.3.

More dramatic are the changes in the density profiles for both oxygen and hydrogen atoms of interfacial water obtained when D is decreased from D = 0.9 to D = 0.7 (third panel from left) and D = 0.62 (right panel). The position of the first O peak is shifted to slightly larger distances from the solid (to z = 3.05 Å), but the intensity of the peak increases as D decreases, as a consequence of the increased water-solid attraction due to the enhanced atomic density in the solid substrate. In addition, the first peak for the hydrogen atoms of water becomes centred on the position of the first O peak when D = 0.7 or less, and it is slightly more intense than

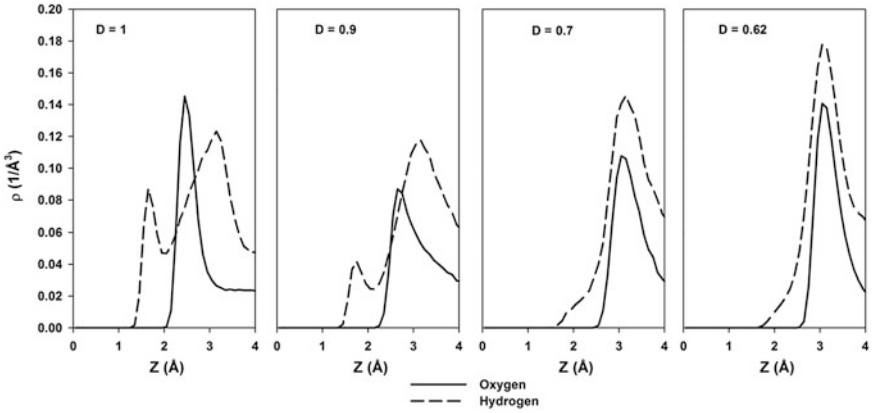


**Fig. 3.4** Density profiles in the direction perpendicular to the solid substrate for oxygen (*continuous line*) and hydrogen atoms (*broken lines*) of water molecules within the droplets used to calculate the contact angles of Fig. 3.3. Because for the water droplet it is difficult to determine the accurate volume that water molecules occupy I estimated the density in these cases based on the same volume of a rectangular box. As a result, the densities reported here are smaller than the true densities. Comparison should only be made among these cases. Results are shown for water on model MgO surfaces in which D decreases from 1 (*left panel*) to 0.62 (*right panel*). Note that both the intensity and the position of the various peaks change as D changes, reflecting changes in orientation of contact water molecules as well as in the density of the hydration layers

the O peak. This indicates that only a few OH bonds are pointing towards the D = 0.7 and D = 0.62 surfaces (note the small shoulders near the surfaces in the H density profiles), that more than one OH bonds per water molecule, on average, are approximately parallel to the solid surface, and that the rest are pointing away from the surface. The orientation of interfacial water molecules remain consistent with the description just provided as D decreases from 0.7 to 0.62, but the density of both first O and H peaks at contact with the D = 0.62 surface are much larger than those near the D = 0.7 surface, as a consequence of the increased surface-water attractions. These changes in the orientation and density of contact water molecules are responsible for the decrease in the equilibrium contact angle found in my simulations as D decreases from 0.9 to lower values.

The most important result presented herein is the demonstration that contact angles larger than 90° are not necessary to attain hydrodynamic slip. Liquid water can slip on hydrophilic surfaces. On the MgO surface, the results show in Fig. 3.2 (left) illustrate that the contact water layer at z = 2.5 Å has the same velocity as the immobile surface. This observation confirms that MgO shows no liquid slip, in qualitative agreement with the contact angle of $\sim 47°$, denoting hydrophilic properties. In Fig. 3.5 I compare the velocity for confined water molecules as a function of their position within the slit-shaped pore when W (left) and D (right) decrease. Liquid slip appears when the velocity of those water molecules in contact with the solid show different velocity than the solid. No slip is found otherwise.

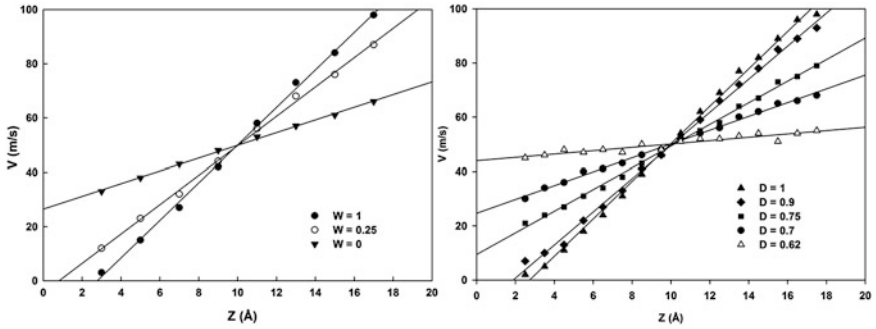


**Fig. 3.5** Velocity profiles for confined water molecules as a function of the position within the narrow slit-shaped channel when reducing W from 1 to 0 (*left*) or D from 1 to 0.62 (*right*). In all cases T = 300 K. The results show that when W = 0.25 slip begins to be observed (it becomes very evident at W = 0). More interestingly, slip is also detected for hydrophilic surfaces, when D is 0.75 or less. Lines are guides to the eye. Estimations for slip lengths, useful for hydrodynamic calculations, can be attained by extrapolating the velocity profiles shown above to the distance at which the fluid velocity equals the surface velocity [42]. For example, when D = 0.62 the slip length is $\sim$6.7 nm

As W decreases the surface becomes more hydrophobic, while as D decreases the surface remains hydrophilic and the contact angle can be as low as $\sim 30°$ (see Fig. 3.3). The results in Fig. 3.5 (left) show that while the MgO surface is characterized by no slip, as the surface becomes more hydrophobic liquid slip appears (slip velocity observed when W = 0 is $v_x$ = 35 m/s), as expected [30]. More interestingly, when the surface becomes very hydrophilic (D = 0.62) (right panel) slip is also possible (slip velocity is $v_x$ = 45 m/s), which contradicts conventional wisdom. It should be reiterated that for all cases considered the surfaces are atomically smooth and water wets all surfaces.

The extent of hydrodynamic slip is expected to depend on the shear rate. For example, Priezjev [44] found that at weak surface/fluid interaction the slip length increases nonlinearly with the shear rate and at strong surface/fluid interaction the slip length linearly increases when the shear rate increase. Ulmanella and Ho [45] reported that the slip velocity increases when the shear rate increases. Thompson and Troian [23] concluded that at sufficiently low shear rate the slip length equals its limiting value and at high shear rate the slip length increases rapidly with the shear rate. To investigate this ability, in Fig. 3.6 I report the velocity profiles obtained after the Couette flow was fully established for surfaces with varying W (left panel, W = 1, 0.25, and 0) and with varying D (right panel, D = 1, 0.7, and 0.62). The shear rate in this simulation equals half of that considered in Fig. 3.5 (i.e., the top surface is driven along the X direction with a constant velocity, $v_X$ = 50 m/s). Qualitatively, the results are consistent with those obtained at higher shear rates (no slip on MgO, hydrodynamic slip on surfaces with W < 1, and on surfaces with D < 0.7), but the slip length was found to decrease as the shear rate decreases (see Table 3.1), in qualitative agreement with results by Thompson and

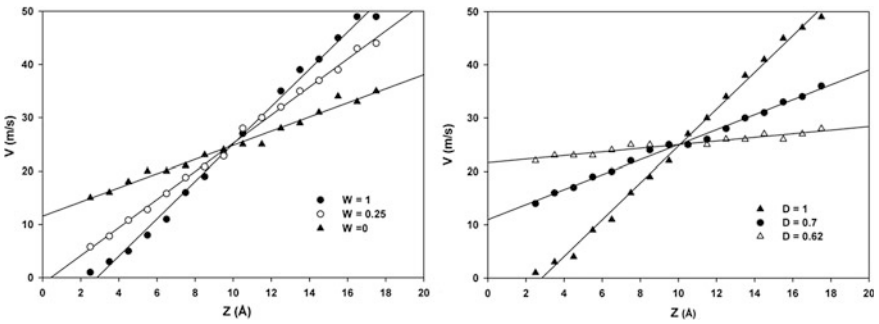


**Fig. 3.6** Velocity profiles obtained after the Couette flow was fully established for water confined in slit-shaped channels. The bottom surface is stationary. The top surface moves with constant velocity of 50 m/s. Results on the *left panel* are for surfaces of varying W. Results on the *right panel* are for surfaces of varying D

**Table 3.1** Slip length estimated for water on two surfaces (D = 0.7 and W = 0) as a function of shear rate

| Shear rate ($s^{-1}$) | D = 0.7 surface (Å) | W = 0 surface (Å) |
|---|---|---|
| $0.5 \times 10^{11}$ | 9.6 | 11.2 |
| $0.25 \times 10^{11}$ | 7.7 | 8.6 |

Note that the calculation of slip length $L_s$ depends on the choice of reference Z = 0. If reference z = 0 is taken at a distance of σ ~4 Å (Van der Waals size of solid atom) away from the surface, the slip length $L_s$ reported in this table become larger ($L_s$ + σ)

Troian [23]. To estimate the extent of slip at much smaller shear rates, in alternative to non equilibrium MD simulations one could employ the Green-Kubo formalism as applied to results from equilibrium simulations, following for example Barrat and Bocquet [21]. These authors found that slip lengths estimated conducting non equilibrium MD simulations were comparable to those obtained employing the Green-Kubo formalism for Lennard-Jones fluids simulated at equilibrium between two solid surfaces.

In Fig. 3.7 I report the in-plane density profiles obtained from equilibrium simulations for water molecules within the first layer near four surfaces: the MgO surface (top left); the W = 0 surface (top right); the D = 0.9 surface (bottom left); and the D = 0.70 surface (bottom right). These results are obtained for water confined within the slit-shaped pores used for the Couette-flow calculations, but at equilibrium ($v_X$ = 0 m/s). The algorithm to calculate the planar density distribution is discussed in Chap. 2. On the two surfaces on the left no hydrodynamic slip is observed. Slip is observed on both surfaces on the right (see Fig. 3.5). On the MgO surface (top left) and on the D = 0.9 surface (bottom left) water molecules adsorb in well defined adsorption spots. No connection between these high-density regions implies that water molecules seldom migrate from one to another. As a consequence, no hydrodynamic slip can be observed. On the W = 0 (top right) and on the

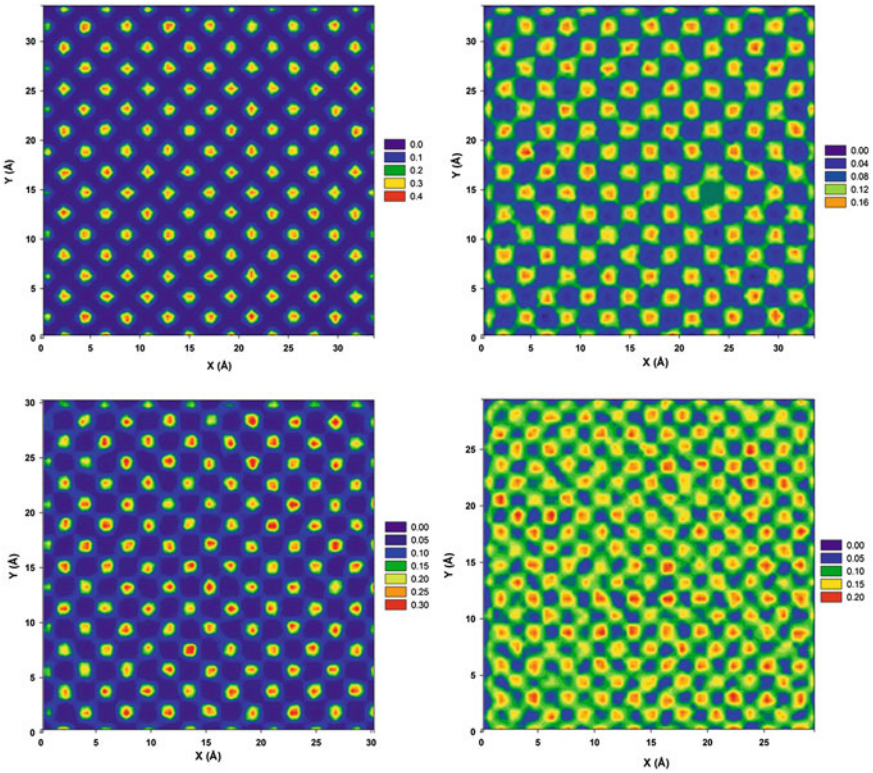


**Fig. 3.7** Surface density distribution of water molecules in the first layer on MgO surface (*top left*), W = 0 surface (*top right*), D = 0.9 surface (*bottom left*), and D = 0.70 surface (*bottom right*). Colour scale reflects the densities (number of atoms per $Å^3$). The *red* areas indicate the positions preferably occupied by water molecules in the contact layers

D = 0.70 (bottom right) surfaces the preferable adsorption sites are connected to each other (see green lines connecting the yellow/red spots). On these surfaces water molecules can easily migrate from one preferable adsorption site to a neighbouring one, leading to liquid slip. Therefore, for slip to occur it is necessary for the water molecules adsorbed on the contact layer to be able to migrate from one adsorption site to the next without leaving the contact layer, irrespectively of the contact angle.

In Fig. 3.8 I report the trajectory of representative contact water molecules near three substrates as obtained after the Couette flow is fully established. Lateral and top views of the trajectories are reported on top and middle panels, respectively. The lateral views identify, via two red lines, the position of the contact water layer. The top views also report the atomic positions on the solid substrates. The left panels are for contact water on MgO (which shows no slip). The centre panels are for contact water on the W = 0 surface (which shows slip). The right panels are for

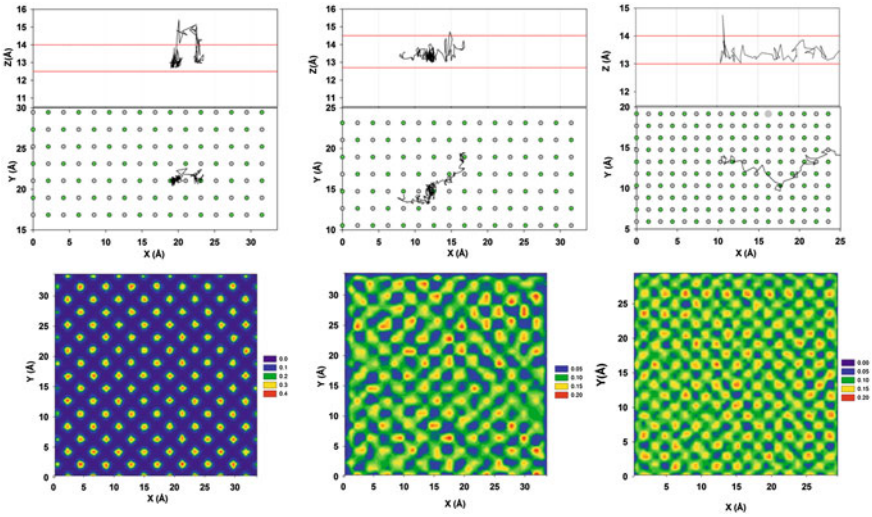

**Fig. 3.8** *Top* Trajectory of three representative water molecules as they migrate from one adsorption site to neighbouring ones on MgO (*left*, no slip), W = 0 surface (*middle*, slip), and D = 0.70 surface (*right*, slip). The two *red* lines on the top panels identify the position of the contact water layer. Surface solid atoms are identified by *green* and *grey* circles (Mg and O, respectively). The *black line* describes the trajectory of one water molecule. On the MgO substrate the trajectory is 35 ps long. On the W = 0 surface the trajectory is 20 ps long. On the D = 0.70 substrate the trajectory is 30 ps long. *Bottom* Planar density distributions are reported on the bottom panels for water molecules at contact with the three surfaces after the Couette flow is fully established. Colour scale reflects the densities (number of atoms per $Å^3$)

contact water on the D = 0.70 surface (which shows slip). The trajectories have been obtained from 35, 20, and 30 ps—long simulation fragments, respectively. On MgO (left), in order to migrate from one adsorption site (on top of a surface Mg atom) to a neighbouring one, the water molecule has to first desorb from the contact water layer, manifesting a hopping diffusion mechanism. On the contrary, the water molecules on either the W = 0 and D = 0.70 surfaces easily migrate from one adsorption site to a number of neighbouring others without necessarily leaving the contact layer. This slide mechanism is possible because the preferable adsorption sites are connected to each other on the W = 0 and D = 0.70 surfaces. As a quantification of the interpretation just provided, on the bottom panels of Fig. 3.8 I report the density distributions of water molecules at contact with the three surfaces just described. These results differ from those presented in Fig. 3.7 because they are obtained after the Couette flow has reached steady states. On MgO the density distribution obtained when shear is applied (left bottom panel in Fig. 3.8) is practically indistinguishable from that obtained at equilibrium (Fig. 3.7), because water molecules move from one preferential adsorption site to another following the hopping trajectories described above. On the contrary, the density distributions obtained under shear on the W = 0 and on the D = 0.70 surfaces (centre and right

bottom panels in Fig. 3.8) clearly show the formation of 'density bridges' that connect the preferential adsorption sites observed at equilibrium (see Fig. 3.7). These density bridges are due to water molecules sliding from one preferential adsorption site to another upon the application of shear, following the trajectories described in the top and middle panels of Fig. 3.8.

## 3.4 Discussions

The results presented above demonstrate that water can slip on hydrophilic surfaces. It is because slip is determined by the distribution of water molecules at contact with the solid and by the strength of water-solid interactions. When favourable adsorption sites exist, but are separated from each other by well-defined sub-nanometer distances, no slip is observed. When favourable adsorption sites are present that are close to each other, liquid slip can occur, provided water-solid attractions are not too strong. Because hydrophobic surfaces, such as graphite, are typically characterized by uniform distributions of interfacial water molecules, while hydrophilic ones, such as crystalline silica, present isolated highly attractive adsorption sites that water molecules readily occupy and seldom leave [46], experiments typically show hydrodynamic slip on hydrophobic surfaces and no slip on hydrophilic ones. My results suggest that such observations are just a coincidence: should hydrophilic surfaces be manufactured with high density of adsorption sites close enough to each other to allow water molecules to easily migrate from one to the next, such hydrophilic surfaces could show liquid slip. My interpretation is consistent with a recent simulation study for the thermal diffusion of carbon nanotube membranes [47], with the molecular mechanism proposed for liquid slip [18], and with experimental observations reported for alkanes [48]. My interpretation could also explain the experimental results by Gao and McCarthy [49], according to which the contact angle hysteresis, and not the static contact angle, should be used, macroscopically, to determine the hydrophobic versus hydrophilic character of a surface.

## 3.5 Conclusions

In conclusion, in this chapter I demonstrated, using molecular dynamics simulations, that slip and no-slip boundary conditions can both be observed for liquid water flowing on solid surfaces on which the static water contact angle is less than 90°. The responsible molecular signature appears to be the distribution of water molecules within the contact layer at equilibrium, coupled with the strength of water-surface interactions. When preferential adsorption sites exist that are sufficiently close to each other that water migration from one to the next can occur without requiring hopping events, hydrodynamic liquid slip occurs. Because of

computing-power limitations, the shear rates considered herein are high, but comparable to those found in high performance lubrication applications (e.g., rocket engines [40]). When verified experimentally my results could lead to the advancement of a variety of applications, including the design of hydrophilic nano-porous membranes with high permeation and self-cleaning hydrophilic surfaces. The desired surfaces should permit atomic-scale sliding of contact water molecules, which could be attained by providing a sufficient amount of preferential adsorption sites, by, e.g., atomic-scale etching, molecular grafting, or by integrating nanoparticles on a surface.

## References


1. Giovambattista, N., Debenedetti, P. G., & Rossky, P. J. (2009). Enhanced surface hydrophobicity by coupling of surface polarity and topography. *Proceedings of the National Academy of Sciences of the United States of America, 106*(36), 15181–15185.
2. Israelachvili JN (1991) *Intermolecular and surface forces* (2nd ed.). London: Academic Press.
3. Striolo, A. (2006). The mechanism of water diffusion in narrow carbon nanotubes. *Nano Letters, 6*(4), 633–639.
4. Kalra, A., Garde, S., & Hummer, G. (2003). Osmotic water transport through carbon nanotube membranes. *Proceedings of the National Academy of Sciences of the United States of America, 100*(18), 10175–10180.
5. Holt JK et al. (2006) Fast mass transport through sub-2-nanometer carbon nanotubes. *Science*, *312*(5776), 1034.
6. Granick, S., & Bae, S. C. (2008). Chemistry: A curious antipathy for water. *Science, 322* (5907), 1477–1478.
7. Chandler, D. (2005). Interfaces and the driving force of hydrophobic assembly. *Nature, 437* (7059), 640.
8. Castrillón, S. R.-V., Ns, Giovambattista, Aksay, I. A., & Debenedetti, P. G. (2009). Effect of surface polarity on the structure and dynamics of water in nanoscale confinement. *The Journal of Physical Chemistry B, 113*(5), 1438–1446.
9. Jamadagni, S. N., Godawat, R., & Garde, S. (2009). how surface wettability affects the binding, folding, and dynamics of hydrophobic polymers at interfaces. *Langmuir, 25*(22), 13092–13099.
10. Godawat, R., Jamadagni, S. N., & Garde, S. (2009). Characterizing hydrophobicity of interfaces by using cavity formation, solute binding, and water correlations. *Proceedings of the National Academy of Sciences of the United States of America, 106*(36), 15119–15124.
11. Cottin-Bizonne, C., Cross, B., Steinberger, A., & Charlaix, E. (2005). Boundary slip on smooth hydrophobic surfaces: Intrinsic effects and possible artifacts. *Physical Review Letters, 94*(5), 056102.
12. Ho, T. A., Papavassiliou, D. V., Lee, L. L., & Striolo, A. (2011). Liquid water can slip on a hydrophilic surface. *Proceedings of the National Academy of Sciences of the United States of America, 108*(39), 16170–16175.
13. Huang, D. M., Sendner, C., Horinek, D., Netz, R. R., & Bocquet, L. (2008). Water slippage versus contact angle: A quasiuniversal relationship. *Physical Review Letters, 101*(22), 226101.
14. Kannam, S. K., Todd, B. D., Hansen, J. S., & Daivis, P. J. (2011). Slip flow in graphene nanochannels. *The Journal of chemical physics, 135*(14), 144701.

15. Kannam, S. K., Todd, B. D., Hansen, J. S., & Daivis, P. J. (2012). Slip length of water on graphene: Limitations of non-equilibrium molecular dynamics simulations. *The Journal of chemical physics, 136*(2), 024705–024713.
16. Maali, A., Cohen-Bouhacina, T., & Kellay, H. (2008). Measurement of the slip length of water flow on graphite surface. *Applied Physics Letters, 92*(5), 053101.
17. Martini, A., Hsu, H.-Y., Patankar, N. A., & Lichter, S. (2008). Slip at high shear rates. *Physical Review Letters, 100*(20), 206001.
18. Martini, A., Roxin, A., Snurr, R. Q., Wang, Q., & Lichter, S. (2008). Molecular mechanisms of liquid slip. *Journal of Fluid Mechanics, 600*(1), 257.
19. Neto, C., Evans, D. R., Bonaccurso, E., Butt, H. J., & Craig, V. S. J. (2005). Boundary slip in Newtonian liquids: A review of experimental studies. *Reports on Progress in Physics, 68*(12), 2859–2898.
20. Zhu, Y., & Granick, S. (2001). Rate-dependent slip of Newtonian liquid at smooth surfaces. *Physical Review Letters, 87*(9), 096105.
21. Barrat, J.-L., & Bocquet, L. (1999). Influence of wetting properties on hydrodynamic boundary conditions at a fluid/solid interface. *Faraday Discussions, 112*, 119–128.
22. Zhu, Y., & Granick, S. (2002). Limits of the hydrodynamic no-slip boundary condition. *Physical Review Letters, 88*(10), 106102.
23. Thompson, P. A., & Troian, S. M. (1997). A general boundary condition for liquid flow at solid surfaces. *Nature, 389*(6649), 360.
24. Niavarani, A., & Priezjev, N. V. (2010). Modeling the combined effect of surface roughness and shear rate on slip flow of simple fluids. *Physical Review E, 81*(1), 011606.
25. Balasubramanian, A. K., Miller, A. C., & Rediniotis, O. K. (2004). Microstructured hydrophobic skin for hydrodynamic drag reduction. *AIAA Journal, 42*(2), 411–414.
26. Rothstein, J. P. (2010). Slip on superhydrophobic surfaces. *Annual Review of Fluid Mechanics, 42*, 89–109.
27. Koishi, T., Yasuoka, K., Fujikawa, S., Ebisuzaki, T., & Zeng, X. C. (2009). Coexistence and transition between Cassie and Wenzel state on pillared hydrophobic surface. *Proceedings of the National Academy of Sciences of the United States of America, 106*(21), 8435–8440.
28. Li, X. M., Reinhoudt, D., & Crego-Calama, M. (2007). What do we need for a superhydrophobic surface? A review on the recent progress in the preparation of superhydrophobic surfaces. *Chemical Society Reviews, 36*(9), 1529.
29. Truesdell, R., Mammoli, A., Vorobieff, P., van Swol, F., & Brinker, C. J. (2006). Drag reduction on a patterned superhydrophobic surface. *Physical Review Letters, 97*(4), 0044505.
30. Voronov, R. S., Papavassiliou, D. V., & Lee, L. L. (2008). Review of fluid slip over superhydrophobic surfaces and its dependence on the contact angle. *Industrial and Engineering Chemistry Research, 47*(8), 2455–2477.
31. Cygan, R. T., Liang, J. J., & Kalinichev, A. G. (2004). Molecular models of hydroxide, oxyhydroxide, and clay phases and the development of a general force field. *The Journal of Physical Chemistry B, 108*(4), 1255–1266.
32. Peng, X. D., & Barteau, M. A. (1990). Characterization of oxide layers on Mg(0001) and comparison of $H_2O$ adsorption on surface and bulk oxides. *Surface Science, 233*(3), 283–292.
33. Karolewski, M. A., & Cavell, R. G. (1992). Coadsorption of cesium and water on MgO(100). *Surface Science, 271*(1–2), 128–138.
34. Wu, M. C., Estrada, C. A., Corneille, J. S., & Goodman, D. W. (1992). Model surface studies of metal oxides: Adsorption of water and methanol on ultrathin MgO films on Mo(100). *The Journal of Chemical Physics, 96*(5), 3892–3900.
35. Berendsen, H. J. C., Grigera, J. R., & Straatsma, T. P. (1987). the missing term in effective pair potentials. *Journal of Physical Chemistry, 91*(24), 6269–6271.
36. Plimpton, S. (1995). Fast parallel algorithms for short-range molecular-dynamics. *Journal of Computational Physics, 117*(1), 1–19.
37. Giovambattista, N., Debenedetti, P. G., & Rossky, P. J. (2007). Effect of surface polarity on water contact angle and interfacial hydration structure. *The Journal of Physical Chemistry B, 111*(32), 9581–9587.

38. Cieplak, M., Koplik, J., & Banavar, J. R. (2001). Boundary conditions at a fluid-solid interface. *Physical Review Letters, 86*(5), 803.
39. Lauga, E., Brenner, M., & Stone, H. (2007). *Handbook of experimental fluid dynamics*. New York: Springer.
40. Khare, R., de Pablo, J., & Yethiraj, A. (1997). Molecular simulation and continuum mechanics study of simple fluids in non-isothermal planar couette flows. *The Journal of Chemical Physics, 107*(7), 2589–2596.
41. Falk, K., Sedlmeier, F., Joly, L., Netz, R. R., & Bocquet, L. (2010). Molecular origin of fast water transport in carbon nanotube membranes: superlubricity versus curvature dependent friction. *Nano Letters, 10*(10), 4067–4073.
42. Voronov, R. S., Papavassiliou, D. V., & Lee, L. L. (2007). Slip length and contact angle over hydrophobic surfaces. *Chemical Physics Letters, 441*(4–6), 273–276.
43. Lee, S. H., & Rossky, P. J. (1994). A comparison of the structure and dynamics of liquid water at hydrophobic and hydrophilic surfaces: A molecular dynamics simulation study. *The Journal of Chemical Physics, 100*(4), 3334–3345.
44. Priezjev, N. V. (2007). Rate-dependent slip boundary conditions for simple fluids. *Physical Review E, 75*(5), 051605.
45. Ulmanella, U., & Ho, C. M. (2008). Molecular effects on boundary condition in micro/nanoliquid flows. *Physics of Fluids, 20*(10), 101512.
46. Argyris, D., Tummala, N. R., Striolo, A., & Cole, D. R. (2008). Molecular structure and dynamics in thin water films at the silica and graphite surfaces. *The Journal of Physical Chemistry C*, *112*(35), 13587.
47. Kalra, A., Garde, S., & Hummer, G. (2010). Lubrication by molecularly thin water films confined between nanostructured membranes. *European Physical Journal Special Topics, 189*, 147–154.
48. Pit, R., Hervet, H., & Léger, L. (2000). Direct experimental evidence of slip in hexadecane: Solid interfaces. *Physical Review Letters, 85*(5), 980.
49. Gao, L., & McCarthy, T. J. (2008). Teflon is hydrophilic. Comments on definitions of hydrophobic, shear versus tensile hydrophobicity, and wettability characterization. *Langmuir, 24*(17), 9183–9188.

# Chapter 4
# The Role of Thin and Mobile Electric Double Layer in Water Purification and Energy Storage

## 4.1 Introduction

Growing worldwide population, changes in weather pattern, and demand for improved standards of living all contribute to shortage of both fresh water and energy (the water-energy nexus). Securing abundant fresh water and energy in economical yet environmentally friendly manners is indeed one of the critical challenges my society faces [1, 2]. A combination of water desalination technologies and renewable energy sources will most likely be needed to win such challenge. Capacitive desalination (CD) promises to purify large amounts of salty water with low energetic consumption [3]. Energy storage devices, e.g., water-based electric double layer capacitors (EDLCs), are needed to deploy renewable energy sources at the large scale [4]. The performance of both CD and EDLC devices relies on the properties of the electric double layer (EDL) formed near carbon-based electrodes.

Back in 1853, Helmholtz was the first to propose the concept of the compact EDL [5], suggesting that the excess surface charge is compensated by counter-ions closely packed near the surface. Although the Helmholtz EDL, with thickness comparable to the radius of solvated ions [6, 7], was observed in solutions of sufficiently high salt concentrations (>1M) [8, 9], the thermal motion of ions [9] yields the 'diffuse' EDL, as proposed by Gouy [10] and Chapman [11], in which the surface charge is balanced by a cloud of rather mobile counter-ions. The diffuse EDL extends to a thickness, the Debye length, that depends on salt concentration, with lower concentrations leading to larger thicknesses [12]. In many cases the EDL resembles the 1924 Gouy-Chapman-Stern model [13], according to which some ions bind to the charged surface (i.e., the compact layer), and others remain in its vicinity (i.e., the diffuse layer).



T.A. Ho, *Nanoscale Fluid Transport*, Springer Theses,
DOI 10.1007/978-3-319-47003-0_4

The EDL is important in the water-energy nexus because both CD and EDLCs function by accumulating and then releasing ions near charged surfaces and/or pores. In the EDLCs literature the accumulation of ions near the surface is quantified in terms of the electrodes capacitance, C. Borrowing the Gouy-Chapman-Stern model, C can be estimated as:

$$\frac{1}{C} = \frac{1}{C_H} + \frac{1}{C_D}. \tag{4.1}$$

In Eq. (4.1) $C_H$ and $C_D$ are the capacitance of the Helmholtz layer and that of the diffuse layer, respectively. Note that, based on Eq. (4.1), the smaller one out of $C_H$ or $C_D$ dominates C. In general, $C_H$ is smaller than $C_D$, and therefore it is the dominant contribution to C [8, 14]. Increasing $C_H$, and hence C, improves the EDLCs' energy density. In CD, because it is desired to balance the excess surface charge by counter-ions within a compact layer, augmenting the compact EDL yields the highest charge efficiency [15]. Under optimal conditions, one charge unit on the electrode removes one ion from a 1–1 (NaCl) electrolyte solution [16]. Unfortunately, in carbon-based electrodes the EDL tends to be diffuse, unless narrow pores are used to remove the solvation shell from the ions [17, 18]. Promoting the formation of the compact EDL in carbon-based electrodes has therefore the potential of positively impacting both EDLC and CD devices.

I introduce here a graphene-based composite electrode that promotes the formation of the atomically thick Helmholtz layer at conditions at which the diffuse layer would be expected. More importantly, in my design the compact layer, not mobile in conventional electrodes, can slip in the direction parallel to the charged surface. My equilibrium and non-equilibrium molecular dynamics (MD) simulation results suggest promising performance indicators towards advancements in water desalination and energy storage devices.

## 4.2 Simulation Details

I considered two electrochemical cells consisting of an electrode pair in contact with an aqueous NaCl solution of salinity $\alpha \sim 5.45$ g/l (0.093 mol/l) at 300 K. In the first cell ('bare electrode', Fig. 4.1a), two oppositely charged graphitic layers face across the aqueous solution. This configuration has been studied extensively [19–21]. In the second cell ('composite electrode', Fig. 4.1b) the configuration is similar to that of the bare electrode, except one neutral graphene membrane is placed in front of each charged graphitic electrode, at a distance of 0.7 nm. In each of these graphene membranes I carved two holes, each of diameter D = 10 Å (Fig. 4.1c) by removing the necessary carbon atoms from the graphene sheet. The holes allow both ions and water to exchange between the 'side pore', near the graphitic charged surface, and the solution at the centre of the cell. I show herein

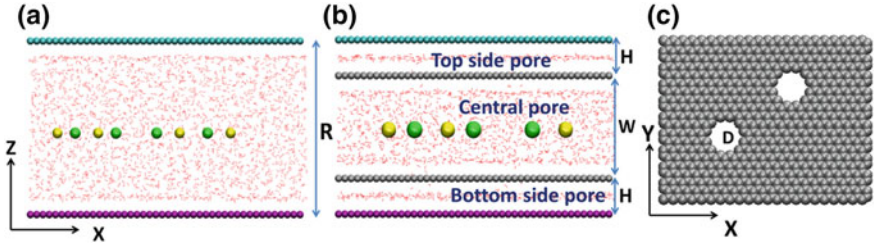


**Fig. 4.1** Schematic representations of the simulated electrochemical cells. In the bare cell (**a**), the negatively charged (*purple*) and positively charged (*cyan*) graphitic electrodes face across the slit pore of width R = 34 Å. In the composite cell (**b**), four graphene sheets are stacked vertically to create three slit-shaped pores: one central pore of width W = 20 Å and two side-pores (*top and bottom*), each of width H = 7 Å. The two outermost graphene sheets are charged positively (*cyan*) and negatively (*purple*), as in the bare cell, while the two inner graphene sheets (*grey*) are not charged. These graphene layers contain two holes each, both of diameter D = 10 Å (**c**). These graphene sheets act as membranes. In both bare and composite cells the area in the XY plane is $5.4 \times 4.2$ nm$^2$. The simulations are conducted at two surface charge densities $\sigma = 3.2$ μC/cm$^2$ and $\sigma = 4.2$ μC/cm$^2$, in an effort to replicate realistic experimental conditions. All simulations are initiated by distributing water molecules (shown in red according to the wireframe convention) uniformly throughout the system. The desired number of $Na^+$ (*yellow*) and $Cl^-$ (*green*) ions are placed within the pore center. The simulated systems are electrically neutral. All simulations are conducted at 300 K

that the graphene membranes effectively modify the structure of the EDL, yielding the unexpected performance in my design.

As a first approximation, the effect of different functional groups bound to the holes is not quantified here, although it is known to have a strong effect in graphene-based membranes [22, 23]. Experimentally, graphene membranes can be produced by several methods including chemical vapour deposition [24], graphene irradiation with a focused electron beam [25], and ultraviolet-induced oxidative etching [26]. The practical arrangement of the graphene membranes near graphitic electrodes requires mechanical aids to prevent the graphene membranes from collapsing on the graphitic electrodes. This collapse would be driven primarily by van der Waals interactions between the graphene layers, and by the tendency of water to evaporate from the region between two hydrophobic surfaces [27]. Methods similar to the one recently proposed by Huang et al. [28] could help solve this design issue. Firstly, they dissolved negatively charged graphene oxide (GO) sheets with positively charged copper hydroxide nanostrands (CHN). Because of the electrostatic interaction the CHN incorporated into GO layers to form the GO/CHN composite membrane. CHN is then removed to obtain GO laminate membranes with a narrow size distribution (3–5 nm) and superior separation performance. Further reduction of GO membrane to graphene membrane is required to obtain the pore structure depicted in my model.

To simulate the electrodes, I assign the same partial charge on all carbon atoms (i.e., I impose a constant surface charge density on each electrode). Merlet et al. [29, 30] showed that it is possible to conduct simulations similar to those discussed

herein by imposing a constant potential across the cell. These authors found that the distribution of electrolytes at the solid/liquid interface is strongly dependent on the algorithm implemented at high surface charge density (i.e., 1.00 e/nm$^2$). At the rather low surface charge densities considered here (0.26 e/nm$^2$ or less), the results are not expected to depend strongly on the algorithm implemented (i.e., constant charge density vs. constant potential).

Because I imposed periodic boundary conditions in all directions, the graphene electrodes are infinitely long along the X and Y directions (see Fig. 4.1 for a schematic). Along the Z direction a large vacuum volume was added above and below the charged graphene layers to minimize undesired interactions between the periodic replicas of my system, which could be caused by long-range electrostatic interactions [31]. All the graphene surfaces were kept rigid and simulated by the force field proposed by Cheng and Steele [32]. The simulated bare cells contained 1764 water molecules and 3 ion pairs, while the composite cells contained 2268 water molecules and 4 ion pairs. These compositions yield the salinity $\alpha \sim 5.45$ g/l (0.093 mol/l), which is consistent with that usually employed in capacitive desalination [16].

Many water models are available in the literature. In one of my publication [33] I compared the predictions obtained by simulating different water models on graphene. I found that the structure of interfacial water predicted implementing SPC/E, TIP4P/2005, SPC/Fw, TIP4P/2005f and SWM4_DP water models is rather similar on neutral, negatively, or positively charged graphene. In this work, water is simulated by implementing the SPC/E model [34]. NaCl ions are modeled by the force field proposed by Dang [35], without considering polarization effects. Some studies suggest that polarization effects might impact water and ions properties at interfaces [36–38]. These effects are not investigated in details in this chapter because, based on my analysis (see Appendix A) [37], they should not significantly affect the results presented. In all systems considered here, the temperature is kept constant at 300 K, using the Nose-Hoover algorithm. The equations of motion are integrated using the GROMACS simulation package, version 4.0.7, with the time step of 1 fs.

Both equilibrium and non-equilibrium simulations were conducted. I conducted my equilibrium all-atom simulations in the NVT ensemble. The simulated systems are equilibrated for 100 ns. Equilibration is considered achieved when the number of ions confined within the side pores remains constant over 50 ns. The results obtained during the last 50 ns of the equilibrium simulations are used to compute the averages reported herein.

Non-equilibrium simulations were conducted to study the flow of electrolyte solutions inside the electrochemical cells. In these non-equilibrium simulations all water molecules and NaCl ions are forced to move along the X direction with constant applied acceleration $2.4 \times 10^{13}$ m/s$^2$ (mimicking, e.g., a gravity-driven flow) [39–41]. In these simulations, because the periodic boundary conditions are applied in the direction of flow, the water and ions that exit the simulation box because of the imposed flow enter the pore from the opposite end of the electrode, thus maintaining a constant number of molecules within the simulation cell.

Because of the periodic boundary conditions, the simulations do not account for phenomena that would be encountered when water and ions enter or exit the electrodes. The non-equilibrium simulations are conducted until the velocities of water and ions in the X direction remain constant over a period of 100 ns (i.e., steady states are achieved). Instead of applying acceleration of $2.4 \times 10^{13}$ m/s$^2$ to all molecules, an equivalent pressure of 100 MPa can be imposed to drive the flow inside the pores. The large value of the acceleration applied in my simulations, clearly non realistic, is due to computing power limitations [42, 43]. However, because it has been reported that the time scale for fluid flow scales linearly with the applied acceleration [23, 44], and because fast water transport through graphitic nanopores and carbon nanotubes under small applied pressures was experimentally observed [45, 46], I expect that small applied pressures can drive the flow through the proposed desalination cell following mechanisms analogous to those discussed below.

## 4.3 Results and Discussions

I first investigated how the electrode design affects the EDL in the two electrochemical cells. The surface charge density applied on both electrochemical cells is $\sigma = 3.2$ μC/cm$^2$. Visual inspection of the simulation snapshots obtained once equilibration is achieved (Fig. 4.2a, b) reveals that the graphene membranes

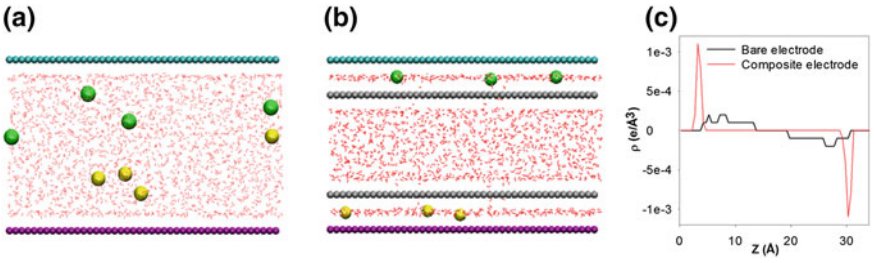


**Fig. 4.2** Representative simulation snapshots at equilibrium for the bare (**a**) and composite (**b**) electrochemical cells. These simulations are conducted at the surface charge density $\sigma = 3.2$ μC/cm$^2$. The colour code is the same as that of Fig. 1.1. Note that while in the bare cell the ions distribute throughout the entire pore, with counter-ions accumulating near the charged surfaces, in the composite cell the ions are not present within the central pore. Instead they accumulate within the side pores, with $Na^+$ ions near the negatively charged surface, and $Cl^-$ ions near the positively charged one. Charge density profiles obtained at equilibrium for bare (*black*) and composite (*red*) cells (**c**). The density distributions are consistent with the formation of diffuse EDLs in the bare cell, as expected at the low salinity and low charge density considered in these simulations. In contrast, the high intensity and narrow peaks observed in the composite cell indicate the formation of compact layers centred at 3.5 and 3.75 Å near negatively and positively charged electrodes, respectively

strongly affect the distribution of the ions. The counter-ions accumulate near the oppositely charged surface in both electrodes, but yielding diffuse EDLs in the bare cell and compact EDLs in the composite cell. The thickness of EDL can be quantified from the charge density profiles of NaCl shown in Fig. 4.2c. Within the bare cell (black line) the thickness (i.e., the distance between the electrode and the end of EDL) of the diffuse EDLs near the negative and positive electrodes are ~13.75 and 14.25 Å, respectively. In contrast, within the composite cell (red line) the thickness of the compact layers near the negative and positive electrodes are 4.75 and 5.25 Å, respectively. These data indicate the formation of compact layers at conditions at which diffuse layers are expected.

Because of the presence of the graphene membranes, when the ions migrate from the central pore to the side pores they remain trapped within the side pores instead of returning to the central pore consequently to thermal motion (as observed in the bare cell, see Fig. 4.3a). The ability of the graphene membranes to keep the ions within the side pores is a crucial feature of my design. If the membrane holes diameter D is too large, the ions can easily diffuse back from the side pores to the central pore (Fig. 4.3b). As a side note, I point out that, because of confinement effects, there are 6 and 4 water molecules in the first hydration shell of $Cl^-$ and $Na^+$ ions, respectively, as opposed to 7 and 6 in bulk aqueous solutions [22, 47]. Clearly, the water molecules in the first hydration shells rearrange in a plane parallel to the pore surfaces (Fig. 4.3c). Because of this re-arrangement, the EDL thickness found in my composite cell is not only much smaller than that of the diffuse layer but also smaller than the thickness of a typical Helmholtz EDL in which the ions remain hydrated [6, 7].

The latter observation has an important practical consequence as reducing the Helmholtz layer thickness enhances the electrode capacitance ($C = \frac{\varepsilon A}{d}$ [14, 17], where A, d, and ε are surface area, Helmholtz layer thickness, and dielectric constant,

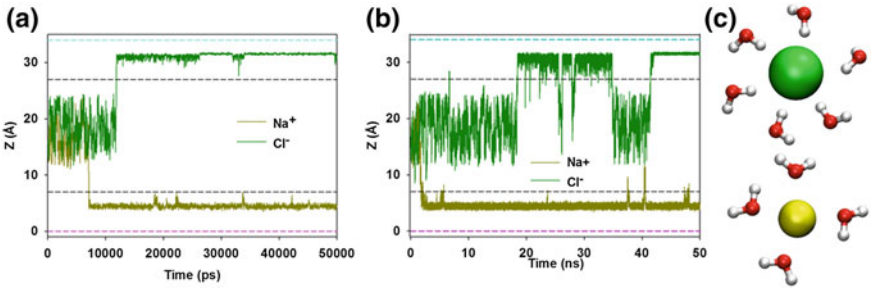


**Fig. 4.3** Z coordinates of representative $Na^+$ and $Cl^-$ ions obtained during equilibrium simulations conducted within the composite cell as a function of time when the hole diameter D = 10 Å (**a**) and D = 15 Å (**b**). The results show that in the case of D = 10 Å, when the ions migrate from the central pore to the side pores (within ~2 ns in the case of $Na^+$, and ~10 ns in the case of $Cl^-$), they remain trapped within the side pores for long times. On the contrary, when D = 15 Å the ions can frequently move between side and central pores. Hydration shells structure of $Cl^-$ and $Na^+$ (**c**) ions within the side-pore of composite cell

respectively). From the charge density profiles I integrate twice (see Appendix B) the Poisson equation [12, 21] $\frac{d^2\psi(z)}{dz^2} = \frac{\rho(z)}{\varepsilon_0}$ ($\varepsilon_0, \psi(z)$, and $\rho(z)$ are vacuum permittivity, electrical potential, and charge density, respectively) to extract the electrical potential profiles near the charged surfaces (Fig. 4.4). To conduct this integration I require two boundary conditions. As first condition, I impose that the electric field in correspondence to the center of the pore is zero ($\frac{d\psi}{dz} = 0$ *at* $z = R/2$, where R is the pore width). The physical reason underpinning this boundary condition is that at the pore center the electric field emitted from the negative electrode neutralizes the one emitted from the positive electrode. As the second boundary condition, I impose that the electrical potential is zero at z = 0. This condition is arbitrary, and it will not affect the potential difference across the EDL. The electrical potential profiles I obtain allow us to calculate the capacitance using the equation $C = \frac{\sigma}{\psi}$, where σ is the surface charge density and ψ is the potential drop across each EDL (see Table 4.1).

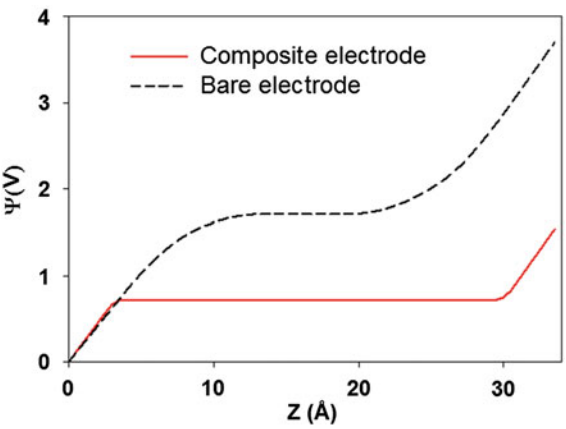


**Fig. 4.4** Electrical potential profiles as a function of distance Z between two electrodes. The potential drop across the EDL is the difference between the potential found at the interface and that determined at the end of the EDL. These results are obtained by integrating the charge density profiles twice using the Poisson equation following the procedure described in the Appendix B

**Table 4.1** EDL thickness, potential drop across the EDL (up to the EDL thickness), and capacitance obtained for bare and composite electrodes

| | Negatively-charged electrode | | | Positively-charged electrode | | |
|---|---|---|---|---|---|---|
| | $d_{EDL}$ (Å) | Potential drop (V) | Capacitance (μF/cm$^2$) | $d_{EDL}$ (Å) | Potential drop (V) | Capacitance (μF/cm$^2$) |
| Composite | 4.75 | 0.72 | 4.44 | 5.25 | 0.81 | 3.95 |
| Bare | 13.75 | 1.71 | 1.87 | 14.25 | 1.99 | 1.60 |

The capacitance predicted for the composite electrode is much larger than that predicted for the bare electrode, as expected due to the change in the EDL thickness. It is perhaps more important to point out that the capacitance predicted for the composite electrode considered in my simulations is ∼70–80 % those reported for electrochemical cells that employ ionic liquids [20, 48, 49].

To study the effect of the salinity on the performance of the composite cell, I provide in Fig. 4.5 the number of NaCl pairs accumulated within the side-pores as a function of the total number of NaCl pairs initially present in the salty water. These equilibrium simulations were conducted at surface charge density of 3.2 μC/cm$^2$. The results show that when 3 or less ion pairs are present ($\alpha \leq 5.45$ g/l), they can all be extracted into the side-pores. When more ion pairs are present (up to $\alpha = 29.07$ g/l ∼ sea salinity), only 3 are extracted from the salty water, while the others remain inside the central pore. This indicate that increasing the system salinity above 5.45 g/l does not affect the number of ions in the side pores, and hence the capacitance of the Helmholtz EDL.

In Fig. 4.6 I compare the results obtained from the simulations of the composite cell when the side-pore width H is 7 and 10 Å. In these simulations, the surface charge density is $\sigma = 4.2$ μC/cm$^2$ and salinity is $\alpha \sim 9$ g/l. Visual inspection of the simulation snapshot (*panel* **a** and **b**) indicates that when H = 10 Å there is two water layers inside the side-pore. As a results the Helmholtz EDL thickness near the negatively charged electrode (*panel* **c**) increases from $d_{Helmholtz} = 4.25$ Å when H = 7 Å (*red line*) to $d_{Helmholtz} = 6.75$ Å when H = 10 Å (*black line*) (see Table 4.2 for more details on $d_{Helmholtz}$ near positively charged electrode). Because the EDL thickness increases the capacitance of the composite electrodes decreases.

The compact EDL described in Fig. 4.2b (composite electrode) is not only atomically thick, but it also slips in the direction of flow parallel to the electrodes (Fig. 4.7a), as suggested by my non-equilibrium simulations. These simulations are initiated either from the last configuration obtained from the equilibrium simulations (i.e., the ions are inside the side pores, Fig. 4.2b) or from the configuration where the

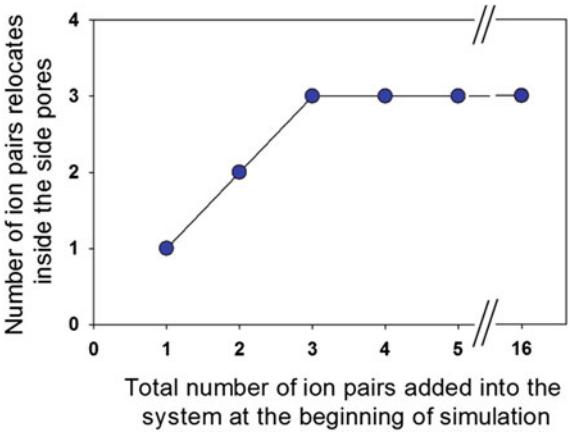


**Fig. 4.5** Number of NaCl pairs accumulated within the side-pores as a function of the total number of NaCl pairs initially present in the salty water

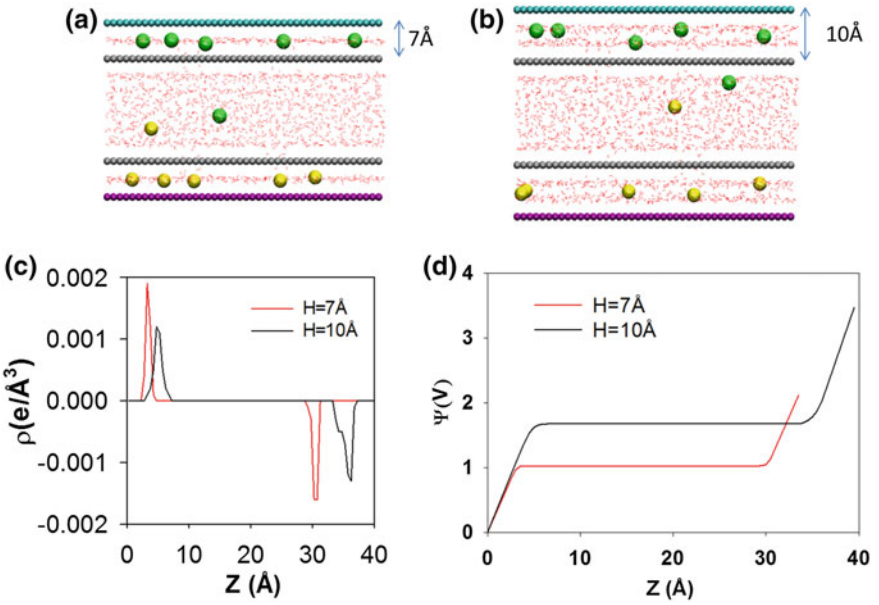


**Fig. 4.6** The effect of side-pore size H on the capacitance of the composite electrode. Representative simulation snapshots at equilibrium for side-pore size H = 7 Å (*panel* ***a***) and H = 10 Å (*panel* **b**). The colour code is the same as that used in Fig. 4.1. Charge density profiles (*panel* **c**) obtained at equilibrium for the composite electrochemical cells in which the side-pore size H = 7 Å (*red*) and H = 10 Å (*black*). Electrical potential profiles (*panel* **d**) across the composite electrode when H = 7 Å (*red*) and H = 10 Å (*black*). See Table 4.2 for thickness, potential drops, and capacitance of EDLs

**Table 4.2** Thickness, potential drop, and capacitance estimated for composite electrodes with side-pore size H = 7 and H = 10 Å. The correspondent simulation results are summarized in Fig. 4.6

| | Negatively charged electrode | | | Positively charged electrode | | |
|---|---|---|---|---|---|---|
| Å | $d_{Helmholtz}$ (Å) | Potential drop (V) | Capacitance (μF/cm$^2$) | $d_{Helmholtz}$ (Å) | Potential drop (V) | Capacitance (μF/cm$^2$) |
| H = 7 | 4.25 | 1 | 4.2 | 5.25 | 1.1 | 3.8 |
| H = 10 | 6.75 | 1.67 | 2.5 | 7.25 | 1.73 | 2.4 |

ions are inside the central pore (Fig. 4.1b). The results obtained from these different initial configurations do not differ from each other. The non-equilibrium simulations are conducted until the ions relocate inside the side pores and steady-states flow is achieved, as described in the 0 section. The results presented in Fig. 4.7a indicate that in the side pores the velocity of water molecules is nonzero (thus consistent with hydrodynamic slip), and it undistinguishable from the velocity of the ions (suggesting that the ions move with water). The velocity of $Na^+$ ions is larger than that of

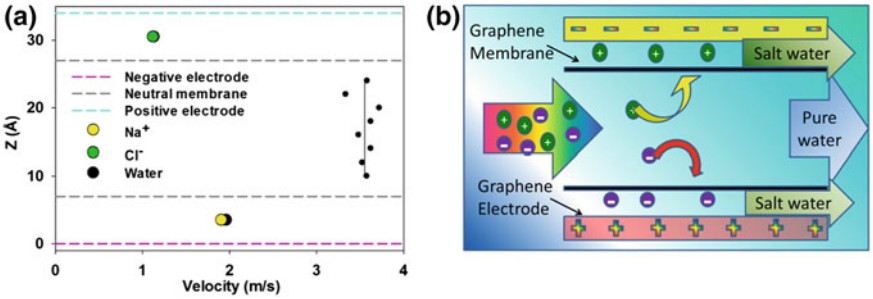


**Fig. 4.7** Velocity of water molecules, $Na^+$ and $Cl^-$ ions inside the composite electrode cell (**a**) as obtained from Poiseuille flow simulations. The water flows with the velocity of ~3.5 m/s within the central pore. In the bottom side-pore, water and $Na^+$ ions flow with the velocity of 1.9 m/s. In the *top side*-pore, water and $Cl^-$ ions flow with the velocity of 1.2 m/s. Despite these differences in flow velocities, all the electrolyte solutions slip inside all of the pores in the composite cell, promising continuous CD operation (**b**)

$Cl^-$ ions because of steric effects within the narrow side pores considered in my design. In the centre of the device water molecules flow with higher velocity than in the side pores because the pore is wider, as expected. The hydrodynamic slip observed both in the side pores and within the central pore is consistent with prior experimental and modelling observations [44–46, 50, 51]. My results suggest that the slippage of the compact EDLs observed within the composite cell can tremendously improve the operation of CD devices because CD is based on the physical adsorption of ions onto charged porous electrodes. In both flow-by [3, 16] and flow-through [52] processes when salty water is exposed to a pair of fresh electrodes the counter-ions adsorb onto the charged electrodes, and fresh water is produced. However, because once the ions enter the electrodes they remain trapped there, regeneration is necessary [3, 16, 52], and the process is not continuous, unless complex operations are designed (e.g., desalination with wires) [53]. As opposed to existing technologies, the composite cell I propose promises the possibility of continuous operation, because there is no need of electrodes regeneration (Fig. 4.7b). I christened my designed '*continuous electrode-membrane desalination cell*'.

The *continuous electrode-membrane desalination cell* I envision is operated as follows: the salty water is fed continuously into the central pore (note that in my non-equilibrium simulations, because of periodic boundary conditions, salty water cannot be fed to the system); during operation the ions diffuse from the central pore to the side pores because of the applied voltages. Compared to existing CD devices [54], the envisioned cell has the advantage that the two neutral graphene membranes provide a physical barrier to separate purified from salty water (central and side pores, respectively). Because the compact Helmholtz EDL can slip inside the side pores, and the water in the central pore can flow smoothly through the device, both fresh and salty water can be continually withdrawn from the device. I reiterate that the operation enabled by the proposed design differs substantially compared to flow-through, flow-by, and desalination-with-wires CD devices in which the ions,

once trapped, remain immobilized inside the porous electrodes [16]. I estimate water permeability (30L/cm$^2$/day/MPa, under the assumption that 10 % of the cross surface area of an hypothetical membrane that embeds the proposed cell is constituted by pores) much larger than that obtained from current membrane-based water desalination techniques [55]. At optimum conditions (surface charge density $\sigma = \pm 4.2$ μC/cm$^2$ and salinity <10.9 g/l) the proposed desalination cell can capture all salty ions within the side pores (100 % rejection), recover 70 % of the salty water initially fed to the system, and yield a charge efficiency of 83 %. Higher charge efficiency, pershaps 100 % can be obtained at higher salinity using larger pores (Fig. 4.8). Note that 100 % charge efficiency has been reported in the literature [16]. Operating the cell will require energy for applying voltages on the electrodes and pumping the salty water through the cell. Because fast water transport through graphitic nanopores and carbon nanotubes under small applied pressures was experimentally observed [45, 46], because it has been reported that CD of brackish water consumes much less energy than reverse osmosis does [3, 56, 57], and because high charge efficiency can be obtained in the engineered cell I propose, I expect the proposed cell to be competitive against existing processes. Unfortunately, quantification of operational costs cannot be conducted reliably at this stage.

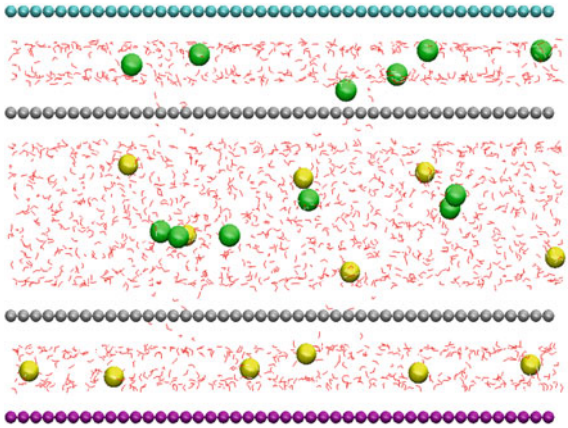

**Fig. 4.8** Representative simulation snapshot at equilibrium for the composite electrochemical cells in which the side-pore size is H = 10 Å, salinity 18 g/l, and surface charge density μ = ±4.2 μC/cm$^2$ [6e/(5.4 × 4.2 nm$^2$)]. There are 6 ion pairs extracted to the side-pores. Unity charge efficiency is obtained: 6 charge units on each electrode extract 6 monovalent ions from NaCl solution

## 4.4 Conclusions

To conclude, I managed to alter the structure of the electric double layer formed within graphitic electrochemical cells. This was achieved by inserting graphene membranes near charged graphitic electrodes. I demonstrated that the ability of manipulating the electric double layer has important implications for the water-energy nexus, as it allows us to both effectively and efficiently store energy and purify water. The compact Helmholtz layer found in the envisioned composite electrochemical cell is not only atomically thick, but it is also able to slip in the direction parallel to the electrodes. The formation of the compact electric double layer significantly enhances the electrodes capacitance, with important implications for the design of electric double layer capacitors. It cannot be overstated that the slippage of the Helmholtz layer is important for the practical realization of the *continuous electrode-membrane desalination cells*. Based on my simulation results, the proposed desalination cell can be operated continuously, achieving up to 100 % charge efficiency, recovering 70 % of the water initially loaded to the system with 100 % salt rejection at salinity <10 g/l, and yielding high water permeability (30 L/cm$^2$/day/MPa).

**Supplemental Information**

The polarizability effects in molecular dynamics simulations of graphene/water interface are reported in Appendix A. In Appendix B, details regarding the integration of the Poisson are reported.

## References

1. Shannon, M. A., et al. (2008). Science and technology for water purification in the coming decades. *Nature, 452*(7185), 301–310.
2. Tour, J. M., Kittrell, C., & Colvin, V. L. (2010). Green carbon as a bridge to renewable energy. *Nature Materials, 9*(11), 871–874.
3. Anderson, M. A., Cudero, A. L., & Palma, J. (2010). Capacitive deionization as an electrochemical means of saving energy and delivering clean water. Comparison to present desalination practices: Will it compete? *Electrochimica Acta, 55*(12), 3845–3856.
4. Miller, J. R., & Simon, P. (2008). Materials science—Electrochemical capacitors for energy management. *Science, 321*(5889), 651–652.
5. Helmholtz, H. (1853). Ueber einige Gesetze der Vertheilung elektrischer Ströme in körperlichen Leitern mit Anwendung auf die thierisch-elektrischen Versuche. *Annalen der Physik, 165*(6), 211–233.
6. Bard, A., & Fraulkner, L. (2001). *Electrochemical methods: Fundamentals and applications*. New York: Wiley.
7. Butt, H. J., & Kappl, M. (2010). *Surface and interfacial forces*. Weinheim, Germany: Wiley.
8. Huang, J. S., Qiao, R., Sumpter, B. G., & Meunier, V. (2010). Effect of diffuse layer and pore shapes in mesoporous carbon supercapacitors. *Journal of Materials Research, 25*(8), 1469–1475.

9. Schmickler, W. (1996). Electronic effects in the electric double layer. *Chemical Reviews, 96*(8), 3177–3200.
10. Gouy (1909). On the constitution of the electric charge at the surface of an electrolyte. *Cr Hebd Acad Sci, 149*, 654–657.
11. Chapman, D. L. (1913). A contribution to the theory of electrocapillarity. *Philosophical Magazine, 25*(148), 475–481.
12. Israelachvili, J. (1991). *Intermolecular & surface forces* (2nd ed.). New York: Academic Press.
13. Stern, O. (1924). The theory of the electrolytic double shift. *Z Elktrochem Angew P* 30: 508–516.
14. Wang, H. N., & Pilon, L. (2011). Accurate simulations of electric double layer capacitance of ultramicroelectrodes. *Journal of Physical Chemistry C, 115*(33), 16711–16719.
15. Zhao, R., Biesheuvel, P. M., Miedema, H., Bruning, H., & van der Wal, A. (2010). Charge efficiency: A functional tool to probe the double-layer structure inside of porous electrodes and application in the modeling of capacitive deionization. *The Journal of Physical Chemistry Letters, 1*(1), 205–210.
16. Porada, S., Zhao, R., van der Wal, A., Presser, V., & Biesheuvel, P. M. (2013). Review on the science and technology of water desalination by capacitive deionization. *Progress in Materials Science, 58*(8), 1388–1442.
17. Chmiola, J., et al. (2006). Anomalous increase in carbon capacitance at pore sizes less than 1 nanometer. *Science, 313*(5794), 1760–1763.
18. Largeot, C., et al. (2008). Relation between the ion size and pore size for an electric double-layer capacitor. *Journal of the American Chemical Society, 130*(9), 2730–2731.
19. Fedorov, M. V., & Kornyshev, A. A. (2008). Ionic liquid near a charged wall: Structure and capacitance of electrical double layer. *The Journal of Physical Chemistry B, 112*(38), 11868–11872.
20. Vatamanu, J., Borodin, O., & Smith, G. D. (2010). Molecular insights into the potential and temperature dependences of the differential capacitance of a room-temperature ionic liquid at graphite electrodes. *Journal of the American Chemical Society, 132*(42), 14825–14833.
21. Shim, Y., Kim, H. J., & Jung, Y. (2012). Graphene-based supercapacitors in the parallel-plate electrode configuration: Ionic liquids versus organic electrolytes. *Faraday Discussions, 154*, 249–263.
22. Konatham, D., Yu, J., Ho, T. A., & Striolo, A. (2013). Simulation insights for graphene-based water desalination membranes. *Langmuir, 29*(38), 11884–11897.
23. Cohen-Tanugi, D., & Grossman, J. C. (2012). Water desalination across nanoporous graphene. *Nano Letters, 12*(7), 3602–3608.
24. O'Hern, S. C., et al. (2014). Selective ionic transport through tunable subnanometer pores in single-layer graphene membranes. *Nano Letters,* 234–1241.
25. Garaj, S., Liu, S., Golovchenko, J. A., & Branton, D. (2013). Molecule-hugging graphene nanopores. *Proceedings of the National Academy of Sciences, 110*(30), 12192–12196.
26. Koenig, S. P., Wang, L. D., Pellegrino, J., & Bunch, J. S. (2012). Selective molecular sieving through porous graphene. *Nature Nanotechnology, 7*(11), 728–732.
27. Giovambattista, N., Rossky, P. J., & Debenedetti, P. G. (2006). Effect of pressure on the phase behavior and structure of water confined between nanoscale hydrophobic and hydrophilic plates. *Physical Review E, 73*(4), 041604.
28. Huang, H. B., et al. (2013). Ultrafast viscous water flow through nanostrand-channelled graphene oxide membranes. *Nat Commun, 4*, 2979.
29. Merlet, C., et al. (2012). On the molecular origin of supercapacitance in nanoporous carbon electrodes. *Nature Materials, 11*(4), 306–310.
30. Merlet, C., et al. (2013). Simulating supercapacitors: Can we model electrodes as constant charge surfaces? *J Phys Chem Lett, 4*(2), 264–268.

31. Ho, T. A., & Striolo, A. (2013). Polarizability effects in molecular dynamics simulations of the graphene-water interface. *The Journal of Chemical Physics, 138*(5), 054117.
32. Cheng, A., & Steele, W. A. (1990). Computer-simulation of ammonia on graphite. 1. Low-temperature structure of monolayer and bilayer films. *The Journal of Chemical Physics, 92*(6), 3858–3866.
33. Ho, T. A., & Striolo, A. (2014). Molecular dynamics simulation of the graphene-water interface: Comparing water models. *Molecular Simulation, 40*(14), 1190–1200.
34. Berendsen, H. J. C., Grigera, J. R., & Straatsma, T. P. (1987). The missing term in effective pair potentials. *Journal of Physical Chemistry, 91*(24), 6269–6271.
35. Dang, L. X. (1995). Mechanism and thermodynamics of ion selectivity in aqueous-solutions of 18-crown-6 ether: a molecular-dynamics study. *Journal of the American Chemical Society, 117*(26), 6954–6960.
36. Levin, Y. (2009). Polarizable ions at interfaces. *Physical Review Letters, 102*(14), 147803.
37. Huang, J. Y., et al. (2013). Nanowire liquid pumps. *Nature Nanotechnology, 8*(4), 277–281.
38. Jungwirth, P., & Tobias, D. J. (2002). Ions at the air/water interface. *The Journal of Physical Chemistry, 106*(25), 6361–6373.
39. Kannam, S. K., Todd, B. D., Hansen, J. S., & Daivis, P. J. (2011). Slip flow in graphene nanochannels. *The Journal of Chemical Physics, 135*(14), 144701.
40. Thomas, J. A., McGaughey, A. J. H., & Kuter-Arnebeck, O. (2010). Pressure-driven water flow through carbon nanotubes: Insights from molecular dynamics simulation. *International Journal of Thermal Sciences, 49*(2), 281–289.
41. Gong, X. J., et al. (2008). Enhancement of water permeation across a nanochannel by the structure outside the channel. *Physical Review Letters, 101*(25), 257801.
42. Ho, T. A., Papavassiliou, D. V., Lee, L. L., & Striolo, A. (2011). Liquid water can slip on a hydrophilic surface. *Proceedings of the National Academy of Sciences, 108*(39), 16170–16175.
43. Lauga, E., Brenner, M., & Stone, H. (2007). *Handbook of experimental fluid dynamics.* New York: Springer.
44. Holt, J. K., et al. (2006). Fast mass transport through sub-2-nanometer carbon nanotubes. *Science, 312*(5776), 1034–1037.
45. Holt, JK., et al. (2006). Fast mass transport through sub-2-nanometer carbon nanotubes. *Science 312*(5776), 1034.
46. Whitby, M., & Quirke, N. (2007). Fluid flow in carbon nanotubes and nanopipes. *Nature Nanotechnology, 2*(2), 87–94.
47. Smith, D. E., & Dang, L. X. (1994). Computer-simulations of Nacl association in polarizable water. *The Journal of Chemical Physics, 100*(5), 3757–3766.
48. Yang, L., Fishbine, B. H., Migliori, A., & Pratt, L. R. (2009). Molecular simulation of electric double-layer capacitors based on carbon nanotube forests. *Journal of the American Chemical Society, 131*(34), 12373–12376.
49. Shim, Y., & Kim, H. J. (2010). Nanoporous carbon supercapacitors in an ionic liquid: A computer simulation study. *ACS Nano, 4*(4), 2345–2355.
50. Kalra, A., Garde, S., & Hummer, G. (2003). Osmotic water transport through carbon nanotube membranes. *Proceedings of the National Academy of Sciences, 100*(18), 10175–10180.
51. Striolo, A. (2006). The mechanism of water diffusion in narrow carbon nanotubes. *Nano Letters, 6*(4), 633.
52. Suss, M. E., et al. (2012). Capacitive desalination with flow-through electrodes. *Energy & Environmental Science, 5*(11), 9511–9519.
53. Porada, S., Sales, B. B., Hamelers, H. V. M., & Biesheuvel, P. M. (2012). Water desalination with wires. *The Journal of Physical Chemistry Letters, 3*(12), 1613–1618.
54. Kalluri, R. K., Konatham, D., & Striolo, A. (2011). Aqueous NaCl Solutions within charged carbon-slit pores: Partition Coefficients and density distributions from molecular dynamics simulations. *Journal of Physical Chemistry C, 115*(28), 13786–13795.

55. Pendergast, M. M., & Hoek, E. M. V. (2011). A review of water treatment membrane nanotechnologies. *Energy & Environmental Science, 4*(6), 1946–1971.
56. Christen, K. (2006). Desalination technology could clean up wastewater from coal-bed methane production. *Environmental Science and Technology, 40*(3), 639.
57. Welgemoed, T. J., & Schutte, C. F. (2005). Capacitive deionization technology™: An alternative desalination solution. *Desalination, 183*(1–3), 327–340.

# Chapter 5
# Water and Methane in Shale Rocks: Flow Pattern Effects on Fluid Transport and Pore Structure

## 5.1 Introduction

The economical success of the shale gas production in the United States in the last decade [1] has attracted great interest around the world. Europe, Australia, Africa, and China initiate research to evaluate the vast unconventional shale reservoirs. The shale rocks are characterized by small pore, compared to, e.g., sandstone formations, composed of pores with size ranging from 1 to 200 nm [2]. Because of these features, the permeability of shale rocks can be as low as 1–100 nD, (for comparison, the permeability of sandstone is of the order of 1–10 mD). The Darcy's law is usually used to calculate the flow rate in micropores in unconventional and conventional reservoirs [3]. According to the Darcy's law, the flow rate is linearly proportional to the driving force (i.e., the pressure drop): $Q = \frac{\pi r^4}{8\mu}\frac{\Delta P}{L}$ (where Q is the flow rate, r is the pore radius, μ is the fluid viscosity, ΔP/L is the pressure drop along the channel length L) [4]. However, for the fluid flow in nano-pores, the enhanced complexity due to the combination of the interactions between the fluids, the significance of viscous and capillary forces, and the pore morphology might cause Darcy's law to no longer provide accurate predictions of fluid flow [5–7]. As I discussed in Chap. 1, because traditional hydrodynamics equations such as the Darcy's law start to fail to describe the flow in the narrow pore in shale formation [8] a new accurate description of gas transport through nanopores is required.

The horizontal drilling and hydraulic fracturing are practiced to enable the economic production of gas, and sometimes oil in shale formations [9]. Because water can both be injected and be present naturally in some shale formations, one complicating characteristic is that water and natural gas can co-exist within the pores, leading to the possibility that two-phase flow occurs through the extremely narrow pores of shale formations [10]. In addition, the interactions between water, gas, and shale rocks within such tight environment can lead to capillary forces and



T.A. Ho, *Nanoscale Fluid Transport*, Springer Theses,
DOI 10.1007/978-3-319-47003-0_5

surface phenomena. Understanding these interactions and how they affect the fluid transport is crucial to estimate gas productivity, design effective stimulation practices, optimize gas production, and reduce the environmental impact of shale gas [9, 11].

In the context of two-phase flow, the flow rate of each phase is linearly proportional to the driving force [6] only if one phase does not interfere with the flow of the other (i.e., according to the Darcy's law) [12]. In this case, one phase effectively reduces the pore area available for the flow of the other. However, in some cases, the Darcy's law fails to describe the two-phase flow in micro- and macro-channels because of the complexity of the flow pattern and its dependence on the pore morphology [13–15]. Experimental study of two-phase flow in nanochannels are prohibitive due to the technical difficulty in fabricating and manipulating nano-devices, in measuring the flow rate in such systems, and in visualizing the flow patterns [16]. As mentioned above, it is expected that the two-phase flow in nanochannels will differ compared to that in wider channels because capillary and surface forces could generate unexpected effects. Recently, Wu et al. [10, 16] used optical imaging to study single and two-phase pressure-driven flows in silicon nitride nanochannels of width 100 nm. They concluded that the linear correlation between flow rate and pressure drop was upheld for single-phase flow, and they reported three different flow patterns including single, annular, and stratified for two-phase flow. More experimental or numerical studies are required to better understand the two-phase flow mechanism in nanochannels.

In this study I employ molecular dynamics simulations to study the two-phase flow of water and methane inside slit-shape muscovite nanochannels. The simulations are designed to investigate the effect of flow patterns on the fluids transport and on the pore structure. In the remainder of this chapter I first present details regarding the model substrate and the algorithms implemented for my simulations. I then discuss the results and how they are pertinent to (i) the two-phase flow in narrow pores and (ii) the pore deformation due to fluid flow and imposed pressure. Finally, I summarize the results.

## 5.2 Simulation Details

In Fig. 5.1 I report a simulation snapshot representing of one of my simulated systems. For all simulations, there are 1800 water and 600 methane molecules inside the slit-shape muscovite nanopore. Muscovite is a phyllosilicate mineral [17, 18] with TOT structure: an Al-centred octahedral sheet is sandwiched between two Si-centred tetrahedral sheets, in which one Al atom substitutes one out of every four Si atoms. An interlayer of potassium ions balances the negative charge due to the Al substitution. The potassium interlayer holds the TOT layers together by electrostatic interactions [19]. Muscovite is a popular substrate because of its perfect cleavage, which allows the creation of large surfaces that are atomically smooth [17]. I chose muscovite because it has similar structure to illite [20], a common clay in

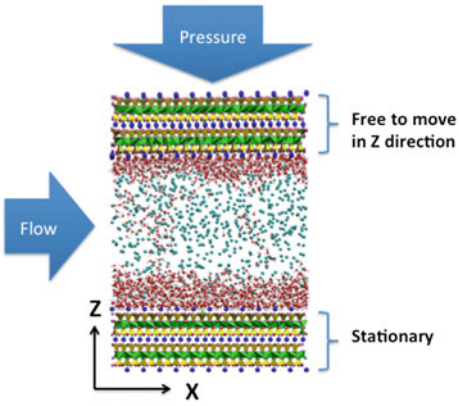


**Fig. 5.1** Simulation snapshot representing one of the simulated systems. Water (*red* and *white spheres*) and methane (*cyan spheres*) are confined in a slit-shape muscovite nanopore. Al-centred octahedral, Si-centred tetrahedral, and potassium atoms are presented in *green*, *yellow*, and *blue* colours, respectively

sedimentary rock environments, including the shale formations [21] found in the Marcellus and Barnett regions [22, 23]. In my model, the muscovite substrate spans 6.2 nm along the X, 5.5 nm along the Y, and 1.96 nm along the Z directions.

The pore-pressure is either 75 MPa or 250 MPa, conditions usually implemented in laboratory studies for rock permeability using the triaxial-test method [24, 25]. In my simulation, all atoms belonging to the bottom muscovite surface are kept rigid. All atoms belonging to the top surface are kept rigid in X and Y directions, but free to move along the Z direction. By applying a force along the Z direction onto the top surface, pore size is adjusted and hence the pore-pressure (i.e., applied force per surface area) is controlled. Initially the pore size is 5 nm (i.e., that of Fig. 5.1). After applying a force $F_1$ to adjust pore-pressure to 250 MPa the pore shrinks from 5 nm to 2.65 nm.

The 75 MPa pore-pressure system is prepared by following two simulation protocols starting from two different initial configurations. In the first protocol, the 'compression' protocol, I start from the initial configuration in which the pore width is 5 nm (Fig. 5.1) and apply a force $F_2$ ($F_2 < F_1$) onto the top surface. During the simulation, the pore size reduces to a width that is larger than the 2.65 nm achieved for the 250 MPa pore-pressure system (discussed later). In the second protocol, the 'expansion' protocol, I use the initial configuration of the system of 250 MPa pore-pressure obtained above (pore size 2.65 nm) and reduce the applied force from $F_1$ to $F_2$. As the applied force is reduced, the pore widens. All of the pore-pressure simulations are conducted for 30 ns. A constant pore size is usually obtained after 6 ns.

After obtaining the desired pore-pressure (i.e., pore size is constant), I conduct the non-equilibrium molecular dynamics simulation to study the two-phase flow inside the muscovite nanopore using Poiseuille flow approach. These simulations are initiated from the final configurations of the pore-pressure control simulations described above. A constant acceleration ranging from 0.02 to 0.08 nm/ps$^2$ is applied to all water and methane molecules within the pore to force them to move

along the X direction. Other simulation conditions are the same as those applied in the pore-pressure controlled simulation, i.e., the bottom surface is treated as rigid bodies and a force is applied on the top surface along the Z direction. The simulations are conducted until steady states (i.e., constant velocity profiles for the fluid inside the pore) are obtained. The Poiseuille flow simulations are conducted for 30 ns. The steady state is usually obtained after 10 ns. In the literature there are two common simulation approaches implemented to study flow in nanopores. The first approach is to apply a body force to all fluids inside nanopore. This method is widely used to study the fluid transport through infinite nanopore with periodicity, which is the condition of our model [26–28]. The second approach is implemented for non-periodic finite nanopore including the flow through membrane [29]. In this method fluid flow through the pore is driven by reservoir pressure control [26, 29]. Two reservoirs (source and sink) are connected to the membrane. A force is applied on the moveable wall [29] or on the fluid within the user-defined region [26] to produce pressure drop between two reservoirs. If one applies the second approach the corresponding pressure drop across the pore should range approximately from $1.5 \times 10^{16}$ to $6 \times 10^{16}$ Pa/m to reproduce my simulation condition. Although these applied accelerations are meant to mimic a pressure-driven flow [30–32], they are too high to be realistic; this is due to computing power limitations [33, 34].

In all cases, the atoms in the muscovite mineral, water, and methane are simulated by implementing the CLAYFF [35], SPC/E [36], and TraPPE [37] force fields, respectively. The temperature is kept constant at 300 K. Periodic boundary conditions are applied in all directions for all simulations. Therefore, the muscovite substrate is infinitely long in X and Y directions. Following the methods implemented in my prior studies, in the Z direction a large vacuum volume is added above the muscovite layer to minimize unphysical effects due to interactions between periodic images of the simulated system [38]. The equations of motion are integrated using the GROMACS simulation package, version 4.0.7, with the time step of 1fs.

## 5.3 Results and Discussions

### *5.3.1 Pore-Pressure 250 MPa*

In Fig. 5.2 I present the result obtained for the 250 MPa pore-pressure system. The final simulation snapshot obtained from pore-pressure control simulation (i.e., without flow) confirms the presence of a two-phase system: water and methane phases (Fig. 5.2a). As expected, water preferentially wets the muscovite surfaces. Visual inspection also suggests the formation of a water bridge connecting the two pore surfaces and spanning the entire length of the pore along the Y direction. Methane molecules form one gas bubble that is trapped within water. From configuration of Fig. 5.2a I initiate the flow simulations by applying a constant

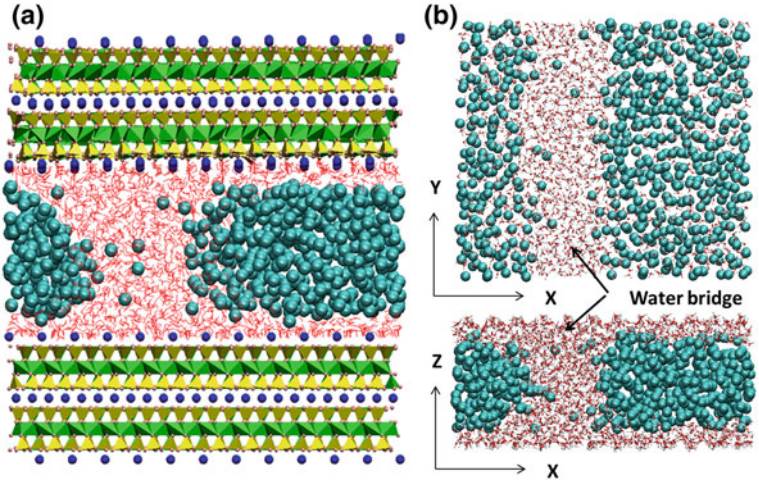


**Fig. 5.2** Simulation snapshot representing the final configuration of the 250 MPa pore-pressure system (**a**). Top (*top panel*) and side (*bottom panel*) views of the flow patterns inside the pore of Fig. 5.2a (surfaces are removed for clarity) when the applied acceleration is 0.05 nm/ps$^2$ or smaller (**b**)

acceleration to the fluid molecules along the X direction. In Fig. 5.2b I present the flow patterns inside the pore when the applied acceleration is 0.05 nm/ps$^2$ or smaller. The flow occurs along the X direction, and the snapshots are obtained after steady states conditions are established. The results presented show that the water bridge, forms in between the two surfaces and spans the entire length along Y direction observed in the pore-pressure controlled simulation, is still present when the applied acceleration is 0.05 nm/ps$^2$ or smaller. This pattern is consistent with the 'slug flow' observed for two-phase flow at larger length scales when the gas phase exists as a large bubbles separated from each other by liquid 'slugs' [39]. Further investigation is necessary to study the dependence of this structure on the length of the simulation box along the Y direction.

When the acceleration increases from 0.05 to 0.06 nm/ps$^2$ the flow pattern changes from that of Fig. 5.2a to that of Fig. 5.3a. The water bridge between the two surfaces is still present, but it no longer spans the entire length of the pore along the Y direction and resembles a water 'pillar' surrounded by methane. As a consequence, water molecules reduce the flow area available to methane, but they do not slow methane flow (discussed later). The flow pattern just described does not change when the acceleration increases from 0.06 to 0.08 nm/ps$^2$. I also point out that the flow pattern change just discussed is irreversible. In other words, even if I reduce the applied acceleration from 0.06 to any value below 0.05 nm/ps$^2$, the flow pattern remains the one described in Fig. 5.3a, and the one described on Fig. 5.2b is not re-established. This is probably evidence of the possibility that long-lived metastable states can strongly affect two-phase fluid flow through nano-pores.

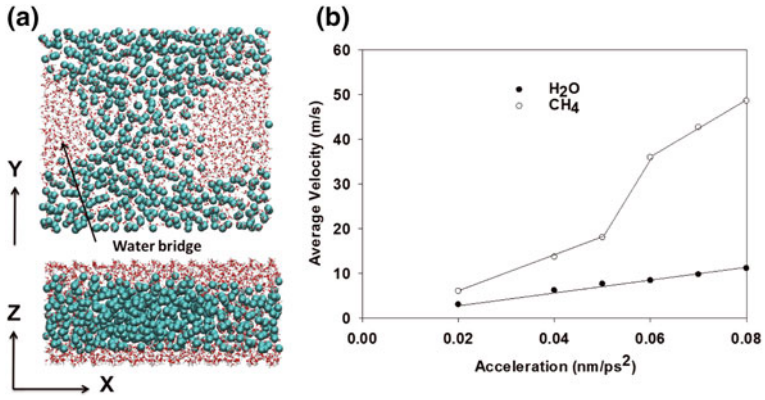


**Fig. 5.3** Top (*top panel*) and side (*bottom panel*) views of the flow patterns inside the pore (surfaces are removed for clarity) when the applied acceleration is 0.06 nm/ps$^2$ or higher (**a**). Average velocity along the X direction of water (*filled circles*) and methane (*empty circles*) during the two-phase flow within the muscovite nano-pore as a function of the applied acceleration (**b**)

In Fig. 5.3b I report the average velocities of water (filled circles) and methane (empty circles) obtained at steady states as a function of the applied acceleration. The results indicate that the average velocity of water increases linearly as the applied acceleration increases, which is consistent with the Darcy's law, as the applied acceleration is the driving force for the flux of water. The results obtained for methane differ significantly from those just described for water. In particular, the average velocity for methane increases linearly when the acceleration increases from 0.02 to 0.05 nm/ps$^2$, and then again from 0.06 to 0.08 nm/ps$^2$. As the acceleration increase from 0.05 to 0.06 nm/ps$^2$, a step increase of the methane velocity is observed. It is also worth pointing out that, even though below 0.05 nm/ps$^2$ and above 0.06 nm/ps$^2$ the relationship between average velocity and applied acceleration is linear, the slopes of the lines differ, suggesting that the effective permeability of the pore is larger at higher applied accelerations. The results also suggest that the Darcy's law can be used to describe the two-phase flow in nanochannels only if there is no change in flow pattern. They also suggest, perhaps more importantly, that the permeability of the porous material depends strongly on the structure of the confined fluid, which can change upon changes in external stimuli, including applied pressure drops. Because when the flow pattern changes the pore size does not change, my results suggest that the step increase in the velocity of methane when the applied acceleration increases from 0.05 to 0.06 nm/ps$^2$ is due to the change in flow pattern from that of Fig. 5.2a to that of Fig. 5.3a. Within the simulated conditions the flow of water continues to obey the Darcy's law.

To better understand how the flow pattern affects the flow of water and methane through the slit-shaped muscovite nanopore I present in Fig. 5.4a the velocity profiles of water (filled symbols) and methane (empty symbols) as a function of the

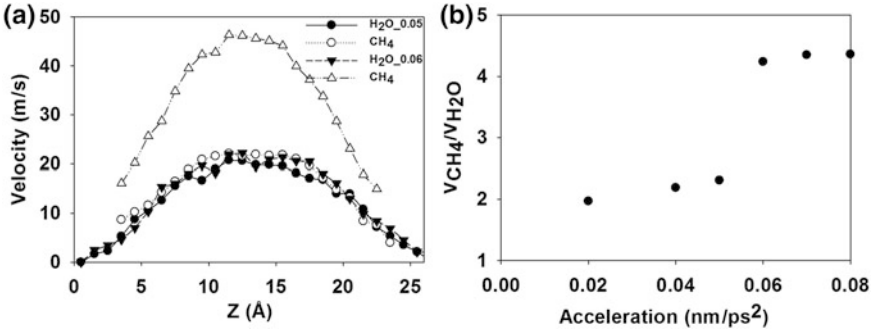


**Fig. 5.4** Velocity profiles of water (*filled symbols*) and methane (*empty symbols*) during the two-phase flow within muscovite pore when the applied accelerations are 0.05 nm/ps$^2$ (*circles*) and 0.06 nm/ps$^2$ (*triangles*) (**a**). Ratio between the average velocity of methane and that of water during the two-phase flow as a function of applied acceleration (**b**)

position within the pore when the acceleration is 0.05 (circles) and 0.06 nm/ps$^2$ (triangles). At the acceleration of 0.05 nm/ps$^2$ (circles) the velocity profiles of water and that of methane suggest that at the pore center methane travels at the same speed as water does (note that very few methane molecules are found near the surface). This suggests that, effectively, the water bridge (see Fig. 5.2) blocks the methane transport in the direction of flow. At the higher applied accelerations, the results in Fig. 5.4a show that, at every position within the pore methane travels much faster than water does. This happens because the water bridge no longer entirely blocks methane transport, as it no longer spans the entire width of the nano-pore. In this configuration methane molecules can move through the pore free from physical block of the water bridge. The effect of the change in flow pattern becomes more evident when I compare the average velocity of methane to that of water inside the pore (Fig. 5.4b). For example, at low accelerations (0.02–0.05 nm/ps$^2$) the ratio between the average velocity of methane and that of water is $\sim$2, while at higher accelerations (0.06–0.08 nm/ps$^2$) this ratio is $\sim$4.3. Note that at 0.05 nm/ps$^2$, despite the velocity of water and that of methane are the same in the middle of the pore (see Fig. 5.4a), the average velocity of methane is as twice the average velocity of water (see Fig. 5.4b). This is because water wets the muscovite surface, and the water molecules in the region near the solid surface are effectively not moving along the direction of motion.

### 5.3.2 *Pore-Pressure 75 MPa*

The results discussed for pore-pressure 250 MPa system strongly depend on the presence of the water bridge and on the flow pattern within the muscovite pore. Building on prior simulation studies for water in clay pores [40, 41], I expect that the

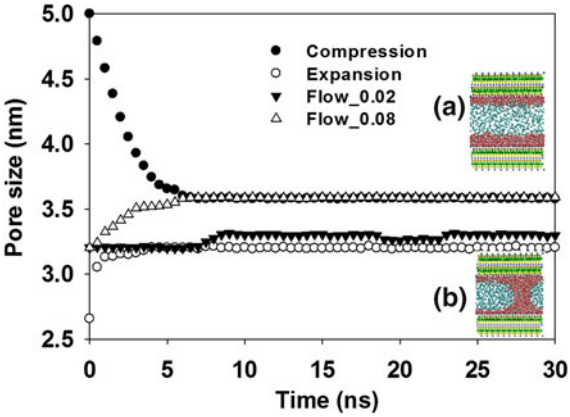


**Fig. 5.5** Pore size as a function of simulation time obtained for 75 MPa compression (*filled circles*), expansion (*empty circles*), flow at acceleration of 0.02 nm/ps$^2$ (*filled triangles*), and 0.08 nm/ps$^2$ (*empty triangles*) simulations

stability of the water bridge will depend on the amount of water present within the pore, on the pore size, and on the pore pressure. To test this possibility I conducted simulations reducing the pore pressure from 250 to 75 MPa. In Fig. 5.5 I show how the pore width changes as a function of time when the applied pressure is instantaneously changed from low to 75 MPa (compression protocol, filled circles), and when the applied pressure is reduced from 250 to 75 MPa (expansion protocol, empty circles). In the compression protocol the pore width decreases from 5 to 3.58 nm, while in the expansion one the pore width increases from 2.65 to 3.19 nm. These results indicate that starting from two different initial configurations, I obtain two stable configurations (insets A and B) that, although characterized by the same pore pressure, are 0.4 nm different in width. Analysis of the simulation snapshots (insets) show that the fluid molecules assume different structures within the system: in the configuration presented in the inset A, water molecules accumulate near the solid surfaces while methane remains in the pore center. In the configuration presented in the inset B, water molecules form a bridge between the two solid surfaces. The resultant capillary force brings the two pore surfaces closer by 0.4 nm compared to when the bridge is not present. Investigation of the total energy of both compression and expansion systems (results not shown) indicate that the configuration shown in inset B is more stable than that depicted in inset A, suggesting that the capillary force is essential in determining the stable pore structure at the nanoscale. Because we observed two different final configurations starting from two different approaches (expansion vs. compression) it is suggested that more simulations initiating from different initial configurations should be performed to obtain the significant statistics.

From the last configurations shown in insets A and B for the pore at 75 MPa I initiate flow simulations. The results show that the imposed flow does not change the fluid distribution within the pore when the simulations start from the structure shown in inset A for all accelerations applied. In this case my results are consistent with the annular two-phase flow described in micro-channels. The correspondent average velocity along the X direction for water (empty circles) and methane

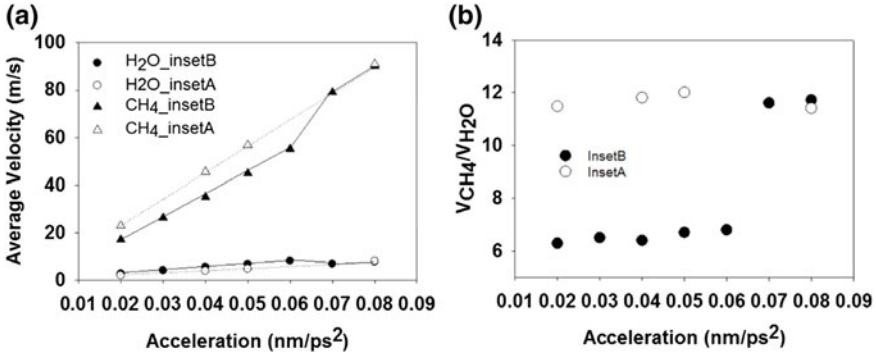


**Fig. 5.6** Average velocity along the X direction of water (*circles*) and methane (*triangles*) during the two-phase flow simulated within the muscovite nano-pore described in inset A (*empty symbols*) and inset B (*filled symbols*) of Fig. 5.5 as a function of the applied acceleration (**a**). Ratio between the average velocity of methane and that of water during the two-phase flow described in inset B (*filled circles*) and inset A (*empty circles*) of Fig. 5.5 as a function of applied acceleration (**b**)

(empty triangles) during the simulated two-phase flow are shown in Fig. 5.6a. The results suggest that the average velocities of both water and methane increase linearly for the whole range of acceleration studied, which is consistent with Darcy's law. The ratio between the average velocity of methane and that of water (empty circles, Fig. 5.6b) is $\sim 12$.

When I simulate the fluid flow starting from the configuration presented in the inset B of Fig. 5.5, my results show that the flow pattern changes over time. When the imposed acceleration is in the range from 0.02 to 0.06 nm/ps$^2$, the water pillar remains, but it becomes thinner as the simulation progresses. One macroscopic consequence of this result is that the pore width slightly increases over time (see filled triangles in Fig. 5.5). When the applied acceleration is increased further to 0.07 and 0.08 nm/ps$^2$, the water bridge vanishes, causing the expansion of the pore from 3.19 to 3.59 nm (empty triangles in Fig. 5.5). In other words, when the applied acceleration is large enough, the fluid structure within the pore changes from that pictured in inset B to that in inset A. The correspondent average velocity along the X direction for water (filled circles) and methane (filled triangles) during the simulated two-phase flow are shown in Fig. 5.6a. The results indicate that the average velocities of both water and methane increase linearly when the applied acceleration increases from 0.02 to 0.06 nm/ps$^2$, which is consistent with Darcy's law. Within this range of applied accelerations, the ratio between the average velocity of methane and that of water (filled circles, Fig. 5.6b) is around 6.4. When the applied acceleration increases to 0.07 and 0.08 nm/ps$^2$, as a step increase of the methane average velocity and a slight decrease of the water average velocity are observed. The ratio between the average velocity of methane and that of water increases to 12 (filled circles, Fig. 5.6b), consistent with the results obtained starting the flow simulations from the configuration of inset A of Fig. 5.5. As described above, when the acceleration increases to 0.07 nm/ps$^2$, there are major changes in

flow pattern and in pore size. Both changes contribute to the step increase of the average velocity of methane. Unexpectedly, the change in flow pattern slightly decreases the average velocity of water, despite of the increase in acceleration. This is because the water in the centre of the pore of inset B of Fig. 5.5 can move faster, even at the smaller acceleration, along the X direction than the water in the water film near the surface in the inset A of Fig. 5.5. The water molecules at the center of the pore move closer to the surface when the bridge is disrupted, leading to lower average velocity for water molecules.

The results just discussed indicate that the fluid flow can alter the effective interactions between water, methane, and pore surfaces, with effects not only on flow patterns and applications of the Darcy's law, but also on the pore structure.

## 5.4 Conclusions

Using molecular dynamics simulation I study the two-phase flow of water and methane inside slit-shape pores obtained from muscovite. The simulations are designed to investigate the effect of flow patterns on the fluids transport and on the pore structure at the temperature of 300 K and pore-pressure of either 75 or 250 MPa. The results indicate that Darcy's law is obeyed as long as the flow pattern does not change. When the fluid structure changes, the movement of methane with respect to that of water changes. My results illustrate the importance of the capillary force, due to the formation of water bridges across the clay pores, not only on the fluid flow, but also on the pore structure, in particular on its width. When the water bridges are broken, perhaps because of fast fluid flow, the capillary force vanishes leading to the significant expansion of the pore. Because muscovite is considered a model of illite, a clay often found in the shale formations in the Marcellus and Barnett regions, these results advance my understanding regarding the mechanism of water and gas transport in tight shale gas formations.

## References

1. Hughes, J. D. (2013). A reality check on the shale revolution. *Nature, 494*(7437), 307–308.
2. Cipolla, C. L., Lolon, E., & Mayerhofer, M. J. (2009). Reservoir modeling and production evaluation in shale-gas reservoirs. In *International Petroleum Technology Conference*.
3. Javadpour, F., Fisher, D., & Unsworth, M. (2007). Nanoscale gas flow in shale gas sediments. *Journal of Canadian Petroleum Technology*, *46*(10).
4. Tanikawa, W., & Shimamoto, T. (2009). Comparison of Klinkenberg-corrected gas permeability and water permeability in sedimentary rocks. *International Journal of Rock Mechanics and Mining Sciences, 46*(2), 229–238.
5. Ahmadlouydarab, M., Liu, Z.-S., & Feng, J. J. (2011). Interfacial flows in corrugated microchannels: Flow regimes, transitions and hysteresis. *International Journal of Multiphase Flow, 37*(10), 1266–1276.

6. Ahmadlouydarab, M., Liu, Z.-S., & Feng, J. J. (2012). Relative permeability for two-phase flow through corrugated tubes as model porous media. *International Journal of Multiphase Flow, 47*, 85–93.
7. Niessner, J., Berg, S., & Hassanizadeh, S. M. (2011). Comparison of two-phase Darcy's law with a thermodynamically consistent approach. *Transport in Porous Media, 88*(1), 133–148.
8. Ziarani, A. S., & Aguilera, R. (2011). Knudsen's permeability correction for tight porous media. *Transport in Porous Media, 91*(1), 239–260.
9. Yethiraj, A., & Striolo, A. (2013). Fracking: What can physical chemistry offer? *The Journal of Physical Chemistry Letters, 4*(4), 687–690.
10. Wu, Q. H., et al. (2014). Optic imaging of two-phase-flow behavior in 1D nanoscale channels. *SPE Journal, 19*(5), 793–802.
11. Silin, D., & Kneafsey, T. J. (2011). Gas shale: From nanometer-scale observations to well modelling. *Canadian Society for Unconventional Gas* CSUG/SPE 149489.
12. Muskat, M., & Meres, M. W. (1936). The flow of heterogeneous fluids through porous media. *Journal of Applied Physics, 7*(9), 346–363.
13. Shao, N., Gavriilidis, A., & Angeli, P. (2009). Flow regimes for adiabatic gas–liquid flow in microchannels. *Chemical Engineering Science, 64*(11), 2749–2761.
14. Indraratna, B., & Ranjith, P. (2001). Laboratory measurement of two-phase flow parameters in rock joints based on high pressure triaxial testing. *Journal of Geotechnical and Geoenvironmental Engineering, 127*(6), 530–542.
15. Ranjith, P. G., Choi, S. K., & Fourar, M. (2006). Characterization of two-phase flow in a single rock joint. *International journal of rock mechanics and mining sciences, 43*(2), 216–223.
16. Wu, Q., et al. (2013). Optic imaging of single and two-phase pressure-driven flows in nano-scale channels. *Lab on a Chip, 13*(6), 1165–1171.
17. Wang, J. W., Kalinichev, A. G., Kirkpatrick, R. J., & Cygan, R. T. (2005). Structure, energetics, and dynamics of water adsorbed on the muscovite (001) surface: A molecular dynamics simulation. *The Journal of Physical Chemistry B, 109*(33), 15893–15905.
18. Teich-McGoldrick, S. L., Greathouse, J. A., & Cygan, R. T. (2012). Molecular dynamics simulations of structural and mechanical properties of muscovite: Pressure and temperature effects. *Journal of Physical Chemistry C, 116*(28), 15099–15107.
19. Teich-McGoldrick, S. L., Greathouse, J. A., & Cygan, R. T. (2012). Molecular dynamics simulations of structural and mechanical properties of muscovite: Pressure and temperature effects. *The Journal of Physical Chemistry C, 116*(28), 15099–15107.
20. White, W. M. (2013). *Geochemistry*. Oxford, UK: Wiley.
21. Pevear, D. R. (1999). Illite and hydrocarbon exploration. *Proceedings of the National Academy of Sciences of the United States of America, 96*(7), 3440–3446.
22. Tian, Y., & Ayers, W. B. (2010). Barnett shale (Mississippian), Fort Worth Basin, Texas: Regional variations in gas and oil production and reservoir properties. In *Canadian Unconventional Resources and International Petroleum Conference*. Society of Petroleum Engineers.
23. Blatt, H., Tracy, R., & Owens, B. (1996). *Petrology: Igneous, sedimentary and metamorphic* (Freeman).
24. Nara, Y., Meredith, P. G., Yoneda, T., & Kaneko, K. (2011). Influence of macro-fractures and micro-fractures on permeability and elastic wave velocities in basalt at elevated pressure. *Tectonophysics, 503*(1–2), 52–59.
25. Tanikawa, W., & Shimamoto, T. (2009). Comparison of Klinkenberg-corrected gas permeability and water permeability in sedimentary rocks (Vol. 46, p. 229). *International Journal of Rock Mechanics and Mining Sciences, 46*(8), 1394–1395.
26. Docherty, S. Y., Nicholls, W. D., Borg, M. K., Lockerby, D. A., & Reese, J. M. (2014). Boundary conditions for molecular dynamics simulations of water transport through nanotubes. *Proceedings of the Institution of Mechanical Engineers, Part C: Journal of Mechanical Engineering Science, 228*(1), 186–195.

27. Joseph, S., & Aluru, N. R. (2008). Why are carbon nanotubes fast transporters of water? *Nano Letters, 8*(2), 452–458.
28. Koplik, J., Banavar, J. R., & Willemsen, J. F. (1988). Molecular dynamics of Poiseuille flow and moving contact lines. *Physical Review Letters, 60*(13), 1282–1285.
29. Wang, L., Dumont, R. S., & Dickson, J. M. (2013). Nonequilibrium molecular dynamics simulation of pressure-driven water transport through modified CNT membranes. *The Journal of Chemical Physics, 138*(12), 124701.
30. Kannam, S. K., Todd, B. D., Hansen, J. S., & Daivis, P. J. (2011). Slip flow in graphene nanochannels. *Journal of chemical physics, 135*(14), 144701.
31. Thomas, J. A., McGaughey, A. J. H., & Kuter-Arnebeck, O. (2010). Pressure-driven water flow through carbon nanotubes: Insights from molecular dynamics simulation. *International Journal of Thermal Sciences, 49*(2), 281–289.
32. Gong, X. J., et al. (2008). Enhancement of water permeation across a nanochannel by the structure outside the channel. *Physical Review Letters, 101*(25), 257801.
33. Ho, T. A., Papavassiliou, D. V., Lee, L. L., & Striolo, A. (2011). Liquid water can slip on a hydrophilic surface. *Proceedings of the National Academy of Sciences of the United States of America, 108*(39), 16170–16175.
34. Lauga, E., Brenner, M., & Stone, H. (2007). *Handbook of experimental fluid dynamics*. New York: Springer.
35. Cygan, R. T., Liang, J. J., & Kalinichev, A. G. (2004). Molecular models of hydroxide, oxyhydroxide, and clay phases and the development of a general force field. *The Journal of Physical Chemistry B, 108*(4), 1255–1266.
36. Berendsen, H. J. C., Grigera, J. R., & Straatsma, T. P. (1987). The missing term in effective pair potentials. *Journal of Physical Chemistry, 91*(24), 6269–6271.
37. Martin, M. G., & Siepmann, J. I. (1998). Transferable potentials for phase equilibria. 1. United-atom description of n-alkanes. *The Journal of Physical Chemistry B, 102*(14), 2569–2577.
38. Ho, T. A., Argyris, D., Cole, D. R., & Striolo, A. (2012). Aqueous NaCl and CsCl solutions confined in crystalline slit-shaped silica nanopores of varying degree of protonation. *Langmuir, 28*(2), 1256–1266.
39. Rebrov, E. V. (2010). Two-phase flow regimes in microchannels. *Theoretical Foundations of Chemical Engineering*, *44*(4), 355–367.
40. Tambach, T. J., Hensen, E. J. M., & Smit, B. (2004). Molecular simulations of swelling clay minerals. *The Journal of Physical Chemistry B, 108*(23), 7586–7596.
41. Rao, Q., Xiang, Y., & Leng, Y. S. (2013). Molecular simulations on the structure and dynamics of water-methane fluids between Na-montmorillonite clay surfaces at elevated temperature and pressure. *Journal of Physical Chemistry C, 117*(27), 14061–14069.

# Chapter 6
# Summary and Outlook

## 6.1 Summary

In this thesis I focus on studying the interfacial fluid behaviours and how these behaviours govern nanoscale fluid transport. In particular, I employ equilibrium and non-equilibrium atomistic molecular dynamics simulations using LAMMPS and GROMACS to study the properties of water, aqueous electrolyte solutions, and methane in contact with metal oxide surfaces, clay minerals, and graphene. From the fundamental understanding of the structural and dynamical properties of the interfacial fluids I learn how to manipulate these properties to enhance the performance of practical applications including nano-fluidic devices, water desalination, energy storage, and shale gas exploration.

The results presented in Chap. 3 demonstrate that liquid water can slip on hydrophilic surfaces, which contradicts conventional knowledge. The responsible molecular signature appears to be the dynamic properties of water molecules within the contact layer, coupled with the strength of water-surface interactions. When preferential adsorption sites exist that are sufficiently close to each other that water migration from one to the next can occur without requiring hopping events, hydrodynamic liquid slip occurs. Because of computing-power limitations, the shear rates considered herein are high, but comparable to those found in high performance lubrication applications. When verified experimentally my results could lead to the advancement of a variety of applications, including the design of hydrophilic nano-porous membranes with high permeation and self-cleaning hydrophilic surfaces. The desired surfaces should permit atomic-scale sliding of contact water molecules, which could be attained by providing a sufficient amount of preferential adsorption sites, by, e.g., atomic-scale etching, molecular grafting, or by integrating nanoparticles on a surface.

In Chap. 4, I manage to alter the properties of the electric double layer formed within graphitic electrochemical cells. This is achieved by inserting graphene membranes near charged graphitic electrodes. I demonstrate that the ability of



T.A. Ho, *Nanoscale Fluid Transport*, Springer Theses,
DOI 10.1007/978-3-319-47003-0_6

manipulating the electric double layer has important implications for the water-energy nexus, as it allows us to both effectively and efficiently store energy and purify water. The compact Helmholtz layer found in the envisioned composite electrochemical cell is not only atomically thick, but it is also able to slip in the direction parallel to the electrodes. The formation of the compact electric double layer significantly enhances the electrodes capacitance, with important implications for the design of electric double layer capacitors. It cannot be overstated that the slippage of the Helmholtz layer is important for the practical realization of the *continuous electrode-membrane desalination cells*. Based on my simulation results, the proposed desalination cell can be operated continuously, achieving up to 100 % charge efficiency, recovering 70 % of the water initially loaded to the system with 100 % salt rejection at salinity <10 g/l, and yielding high water permeability (30 L/cm$^2$/day/MPa).

In Chap. 5, I study the two-phase flow of water and methane inside slit-shape pores obtained from muscovite. The simulations are designed to investigate the effect of flow patterns on the fluids transport and on the pore structure at the temperature of 300 K and pore-pressure of either 75 or 250 MPa. The results indicate that the Darcy's law is obeyed as long as the flow pattern does not change. When the fluid structure changes, the movement of methane with respect to that of water changes. My results illustrate the importance of the capillary force, due to the formation of water bridges across the clay pores, not only on the fluid flow, but also on the pore structure, in particular on its width. When the water bridges are broken, perhaps because of fast fluid flow, the capillary force vanish leading to the significant expansion of the pore. Because muscovite is considered a model of illite, a clay often found in the shale formations in the Marcellus and Barnett regions, these results advance our understanding regarding the mechanism of water and gas transport in tight shale gas formations.

Although some models may not be realistic because of limitation in computational resources my research results significantly contributes to our understanding of the mutual relation between the microscopic properties of interfacial fluids and macroscopic observations. This understanding could provide us a systematically strategy in designing innovative materials and engineering processes.

## 6.2 Outlook

The results presented in Chap. 3 can be used to further our understanding toward a few phenomena and applications. For example, Rafiee et al. [1] reported experimental and simulation results illustrating the wetting transparency of graphene. They took advantage of this property to improve the performance of the condensation heat transfer applications. Copper is the material used in heat transfer equipment due to its very high thermal conductivity. To prevent the oxidation of Cu coating is required. If the coating surface becomes more hydrophilic condensed water forms a liquid film that can reduce the heat transfer coefficient. If the coating

Cu surface becomes more hydrophobic the nucleation density of condensed water decreases leading to the decrease of heat transfer coefficient. The authors shown that coating one layer of graphene on Cu surface does not significantly change its the intrinsic wettability, as the contact angle measured on Cu surface is comparable with that measured on one-layer-graphene-coating one. Graphene coating not only prevents Cu surface from oxidation but also increases 30–40 % heat transfer efficiency. Although coating Cu surface with one layer of graphene does not significantly alter the static contact angle I believe that it would severely change the dynamic contact angle and dynamic properties of water near the copper surface. This is because, based on my result reported in Chap. 3, the graphene with the distance between two carbon atoms is $\sim 1.42$ Å which is smaller than the diameter of water molecule will be an excellent platform for water slippage. This argument is currently being investigated in my group.

The results reported in Chap. 4 indicate that the water molecules and ions can slip inside very narrow charged graphene channels. My hypothesis is that charged graphene surface might become very hydrophilic, but water still can slip on it. To support this hypothesis, I will investigate the effect of surface charge density on the contact angle and on the degree of water slippage. I expect to see the contact angle of water droplet and the degree of slippage decrease when the surface charge density increases. If successful, this work will serve as a reliable complement to my research reported in Chap. 3. It will also provide an idea to experimentalist to study the water slippage on hydrophilic surfaces because charged graphene surface can be obtained experimentally.

I am also interested in the research on the geological storage of $CO_2$, a method to bury $CO_2$ underground to reduce atmospheric $CO_2$, which helps to reduce global warming and dangerous climate change. The $CO_2$ collected from its sources such as power plant is injected into the depleted oil and gas reservoirs, deep saline formations, and deep oceans. The interactions among injected $CO_2$, saline fluids, and sedimentary rocks, in particularly the migration of $CO_2$ are important to designing, predicting the behaviors, and monitoring sequestration systems and sites [2]. To prevent $CO_2$ leakage to the atmosphere ($CO_2$ is buoyant and move upward), several storage mechanisms are proposed. One of the principle mechanisms is the structural trapping by which the impermeable or low permeability rocks acts as a seal to prevent $CO_2$ moving upward. The $CO_2$ migration can also be prevented by the residual trapping mechanism by which the micrometer scale $CO_2$ bubbles are trapped by the capillary force. As a first prediction, the water 'bridge' observed in Chap. 5 might prevent the $CO_2$ migration during the injection stage, but can act like a 'seal' to prevent $CO_2$ leakage during storage stage. The dissolution of $CO_2$ into brine is another mechanism (i.e., dissolution trapping) that might be responsible for up to 22 % of the $CO_2$ store at the Bravo Dome $CO_2$ nature gas field in New Mexico [3]. In addition, injected $CO_2$ can react with mineral such as calcite available in the reservoir resulting in permanent storage (mineral trapping). It can also physically adsorb on clay surfaces and clay interlayers. The $CO_2$ invasion into the interlayer of the clays mineral can lead to the swelling. The swelling can act as a storage mechanism but also change the porosity, permeability and formation of

micro-fracture in the cap rocks. For example, Giesting et al. [4] experimental studied the interaction between $CO_2$ and Na-Monmorillonite. They demonstrated that the d-space of clay expands because of $CO_2$ adsorption. For the dry clay the d-space is around 10 Å. The d-space of the dry clays does not increase upon the exposure to dry $CO_2$. Residual water is required for the $CO_2$ intercalation. On the contrary, Schaef et al. [5] reported that smectite clay with 2 layers of water in the interlayer will collapse into 1 water layer state upon the exposure to dry $CO_2$.

Molecular simulation can help to establish a solid scientific background related to geological $CO_2$ storage. Myshakin et al. [6] using molecular dynamics simulation shown that the intercalation of $CO_2$ into the clay depending on the water content in the interlayer space. Inside the interlayer $CO_2$ molecules tend to orient parallel to the clay surfaces. The invasion of $CO_2$ into the clay interlayer can also promote the migration of Na ions to the interlayer. The authors also suggest that this could change the hydrophobicity of the surface. In my opinion it is difficult to measure the contact angle in the interlayer to confirm authors' suggestion. Another approach can be used to investigate the hydrophobicity of the surface in the very small pore is to study the probability of forming a cavity inside the water as proposed by Garde et al. [7].

## References

1. Rafiee, J., et al. (2012). Wetting transparency of graphene. *Nature Materials, 11*(3), 217–222.
2. Benson, S. M., & Cole, D. R. (2008). $CO_2$ sequestration in deep sedimentary formations. *Elements, 4*(5), 325–331.
3. Sathaye, K. J., Hesse, M. A., Cassidy, M., & Stockli, D. F. (2014). Constraints on the magnitude and rate of $CO_2$ dissolution at Bravo Dome natural gas field. *Proceedings of the National Academy of Sciences, 111*(43), 15332–15337.
4. Giesting, P., Guggenheim, S., Koster van Groos, A. F., & Busch, A. (2012). Interaction of carbon dioxide with Na-exchanged montmorillonite at pressures to 640 bars: Implications for $CO_2$ sequestration. *International Journal of Greenhouse Gas Control, 8*, 73–81.
5. Schaef, H. T., et al. (2012). In situ XRD study of Ca 2+ saturated montmorillonite (STX-1) exposed to anhydrous and wet supercritical carbon dioxide. *International Journal of Greenhouse Gas Control, 6*, 220–229.
6. Myshakin, E. M., Saidi, W. A., Romanov, V. N., Cygan, R. T., & Jordan, K. D. (2013). Molecular Dynamics simulations of carbon dioxide intercalation in hydrated Na-montmorillonite. *The Journal of Physical Chemistry C, 117*(21), 11028–11039.
7. Godawat, R., Jamadagni, S. N., & Garde, S. (2009). Characterizing hydrophobicity of interfaces by using cavity formation, solute binding, and water correlations. *Proceedings of the National Academy of Sciences, 106*(36), 15119–15124.

# Appendix A
# Polarizability Effects in Molecular Dynamics Simulations of the Graphene/Water Interface

## A.1 Abstract

The importance of including the polarizability of both water and graphene in molecular dynamics simulations of the water/graphene system was quantified. A thin film of rigid SPC/E and polarizable SWM4_DP water on non-polarizable and polarizable graphene surfaces were simulated. The graphene surface was either maintained neutral or charged, positively and negatively. The results suggest that SPC/E and SWM4_DP water models yield very similar predictions for the water structural properties on neutral non-polarizable graphene, although they yield slightly different dynamical properties of interfacial water on neutral non-polarizable graphene.

More pronounced were the differences obtained when graphene was modeled with a polarizable force field. In particular, the polarizability of graphene was found to enhance the number of interfacial SWM4_DP water molecules pointing one of their OH bonds towards the neutral surface. Despite this structural difference, the dynamical properties predicted for the interfacial SWM4_DP water were found to be independent on polarizability as long as the polarizability of a carbon atom is smaller than $\alpha = 0.878$ Å. On charged graphene surfaces, the effect of polarizability of graphene on structural properties and some dynamical properties of SWM4_DP water is negligible because electrostatic forces due to surface charge dominate polarization forces, as expected. For all cases, my results suggest that the hydrogen bond network is insensitive to the polarizability of both water and graphene. Understanding how these effects will determine the accumulation of ions near neutral or charged graphene could have important implications for applications in the fields of energy storage and water desalination.

## A.2 Introduction

Many groups have discussed the importance of including the polarizable term in molecular dynamics (MD) simulations, especially in those simulations conducted for ions at the water/air interface [1–7]. Levin argued that the ability of adjusting the



T.A. Ho, *Nanoscale Fluid Transport*, Springer Theses,
DOI 10.1007/978-3-319-47003-0

charge distribution of an ion, i.e., its polarizability, is necessary to capture the right physic of ions at interfaces [8]. Berkowitz and Perera found significant differences in both energy and geometry for $Na^+(H_2O)_n$ and $Cl^-(H_2O)_n$ clusters depending on whether or not polarizable force fields were implemented [9]. Dang and Smith found that the properties predicted by simulations for water-ion clusters depend on the magnitude of the ion polarizablity [10]. Jungwirth and Tobias [11] demonstrated that heavier halogen anions have a propensity to accumulate at the water/air interface, proportional to their polarizability. Recent interesting results by Caleman et al. explain the surface preference of halides using MD simulations that implemented polarizable force fields [12].

The work briefly summarized above suggests the need of implementing polarizable force fields in simulating aqueous electrolytes at the water/air interfaces. As other interfaces are of practical interest, one wonders whether polarizable effects are important to describe every interface. For example, it is still unclear whether it is important to implement polarizable force fields to simulate solid/water interfaces. In this work I are concerned with the graphene/water interface. Graphene is an exceptional material possessing a unique combination of high surface area, extraordinary mechanical, thermal, and chemical stability, and remarkable electronic and optical properties [13, 14]. It is being used in many applications, ranging from materials sciences [15, 16] to the energy field (batteries and electric double layer capacitors) [17–20], from sensing devices [21] to catalysis [22]. Because some of these applications take place in aqueous environments, it is important to understand at the molecular level the structure of interfacial water on graphene under different conditions. Simulations are often conducted for such purposes. Most of the simulations for water on graphene reported in the literature were obtained implementing non-polarizable force fields [23–25]. One exception is the work of Sala et al. [26] These authors studied aqueous electrolyte solutions confined within a graphene slit-shaped pore. Two sets of potential models were implemented: (a) the rigid non-polarizable SPC/E potential for water with non-polarizable ions, and (b) the rigid polarizable RPOL model for water with polarizable ions. Graphene was in both cases treated as non-polarizable. The results indicated that polarizable force fields favor the accumulation of ionic species near the solid/liquid interface. To secure progress, I believe it is necessary to quantify the effect of polarizability of both water and graphene on the water properties, as predicted by simulations. When synergistically coupled to experimental data, this quantification will allow accurate prediction of the properties of aqueous electrolyte solutions at the graphene interface, necessary for the development of energy storage (e.g., electric double layer capacitors) and water desalination devices, among others. The performance of these devices depends in fact on the accumulation of ions near graphene, which, as suggested by the results obtained at the water/air interface, might be affected by polarization effects.

## A.3 Simulation Methods

In this work, three simulation sets were conducted. In the first set, I considered a thin film of either SPC/E [27] or SWM4_DP [28] water on neutral, non-polarizable graphene. These simulations were conducted to verify the importance of implementing a polarizable water model when the water/graphene system is of interest. Within the SPC/E model water is described as rigid with three point charges: two hydrogen sites and one oxygen site. The oxygen site also corresponds to the center of Lennard-Jones (LJ) interactions. This model has been extensively used by many, and it is known to satisfactorily reproduce structure and diffusion of bulk liquid water at ambient conditions. In my simulations one SPC/E water molecule was kept rigid by applying the SHAKE algorithm [29] to constrain the two OH bonds and the fictitious H–H bond length. The polarizable water model SWM4_DP was chosen because it reproduces well vaporization enthalpy, dielectric constant, self-diffusion coefficient, and air/water interfacial tension. In the SWM4_DP model, the permanent charge distribution of a water molecule is represented by three point charges: two hydrogen sites and one site positioned along the HOH bisector. The electronic induction is represented by a classical charged Drude particle [30, 31], bound to the oxygen site by a harmonic spring. The oxygen site carries a charge equal and opposite to the one of the Drude particle. The oxygen site is also the center of intermolecular LJ interactions. In neutral non-polarizable graphene, all carbon atoms were maintained rigid and modeled as LJ spheres employing literature parameters [32].

In the second simulation set, a thin film of polarizable SWM4_DP water [28] (polarizability $\alpha \sim 1.042$ Å$^3$) on neutral polarizable graphene surfaces was simulated to study the effect of graphene polarizability on water properties. To simulate the polarizability of carbon atoms, I implemented the Drude-particle method [30, 31], inspired by the SWM4_DP water model (described in the paragraph above). Each carbon atom was represented by a fixed charged LJ carbon atom and a Drude particle carrying a charge opposite in sign to that fixed on the center. The fixed carbon atom and the Drude particle were connected by a spring. Manipulating the spring constant and the charge on the Drude particle results in different polarizability. The LJ parameters for the fixed carbon atoms were identical to those used in the first simulation set. The polarizability of a carbon atom in graphene is expected to be around $\alpha \sim 0.878$ Å$^3$, which is the polarizability of the carbon atom in $CCl_4$ as simulated by Chang and Dang [33]. Because I excluded the interactions among the carbon atoms in the graphene sheet, the polarizability of carbon atoms used in my simulations should reflect the out-of-plane value. According to Langlet et al. [34], the out-of-plane polarizability of a carbon atom varies from 0.5 to 1.5 Å$^3$. They used 0.86 Å$^3$, close to the value $\alpha \sim 0.878$ Å$^3$ I expect to be reasonable. Karapetian and Jordan [35] implemented out-of-plane $\alpha \sim 0.57$ Å$^3$ to study the properties of a water cluster on graphite. They concluded that using an anisotropic polarizability on the carbon atoms gave the similar structures and binding energies to those obtained using an isotropic polarizability. To fully understand the effect of

polarizability I conducted additional simulations, varying the polarizability α of a carbon atom from 0 (no polarizability) to 1.1 $Å^3$ (i.e., α = 0, α = 0.578, α = 0.878 and α = 1.1 $Å^3$).

In the third and last simulation set, a thin film of polarizable water SWM4_DP was simulated on charged polarizable graphene and on charged non-polarizable graphene surfaces to understand the role of the polarizability of graphene on the water properties when the graphene surfaces are charged, negatively or positively. The water/charged graphene interface is encountered in many practical applications such as electric double layer capacitor (EDLC) or capacitive desalination (CD) [36]. In the present contribution I considered two representative surface charge densities (i.e., −8 and +8 $\mu C/cm^2$). The non-polarizable graphene was simulated as discussed in the first simulation set. The polarizable graphene was simulated using the approach described in the second simulation set, with polarizability α = 0.878 $Å^3$. When the graphene surface was charged, all the fixed carbon atoms belonging to the graphene sheet on top of the graphitic slab (shown below) carried the same partial charge.

In Fig. A.1 I represent a simulation domain containing SPC/E water molecules on a neutral non-polarizable graphite surface. Similar domains were employed for all other simulations. In my simulation box, a thin film composed by 829 water molecules was placed on a 27.0 × 29.8 $Å^2$ graphite surface. All simulations presented below were conducted using the GROMACS simulation package [37], version 4.0.7. During each simulation the number of particles (N) in the system, the volume (V), and the temperature (T) were maintained constant (i.e., I implemented the NVT ensemble). The system temperature was maintained at 300 K by applying the Nose-Hoover thermostat with the relaxation time of 100 fs. Periodic boundary conditions were applied in all three directions (note that the Z direction is the one perpendicular to the solid substrate). Long-range interactions were calculated by the particle mesh Ewald (PME) method [38]. Along the Z direction a large vacuum volume was added to eliminate unphysical interactions between periodic images of the simulated system. Similar approaches have been implemented in my prior work [39]. Alternatively, one can apply two-dimensional algorithms available for treating long-ranged electrostatic interactions [40]. The resultant lengths of the simulation box used herein along the X, Y, and Z directions were 2.70, 2.98, and 10.00 nm, respectively.

The equations of motion were integrated with a time step of 1 fs. After equilibration, the system coordinates were recorded every 200 time steps (i.e., 200 fs of simulation), and used for subsequent analysis. Each simulation lasted 3 ns. The results obtained during the first 1 ns were discarded (equilibration), while the trajectories recorded during the last 2 ns of the simulation were used to calculate the properties of interest. By monitoring temperature, density profiles, and orientation probability as a function of simulation time I confirmed that the reported results are obtained after equilibration is complete. The simulation trajectories were analyzed to extract detailed information regarding atomic density profiles, orientation, residence time, translation and rotational dynamics for interfacial water. Additional

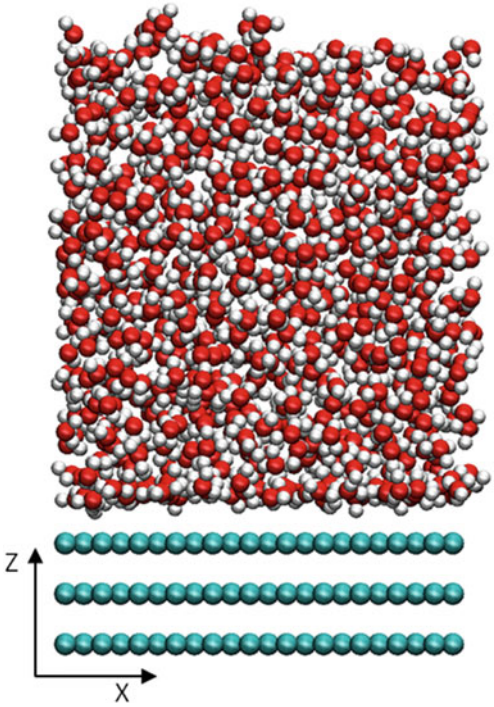


**Fig. A.1** Side view of the simulation box with SPC/E water molecules on a neutral non-polarizable graphite surface. *Red*, *white*, and *cyan* spheres represent oxygen, hydrogen, and carbon atoms, respectively

details concerning the hydrogen bond network near the interface were extracted. The algorithms employed for such analysis have been described in previous publications from my group [39, 41–45].

## A.4 Results and Discussions

### *A.4.1 Density Profiles*

In Fig. A.2 I present the density profiles in the direction perpendicular to the surface for oxygen (left) and hydrogen (right) atoms of water molecules near graphite. The results are compared when different force fields are implemented.

On the top panels I compare the density profiles obtained for SPC/E and SWM4_DP water simulated on the neutral non-polarizable graphene surface. The comparison suggests a minimal difference due to the polarization. The oxygen density profile obtained for SPC/E water indicates that a first intense density peak forms at $z = 3.25$ Å and a second, less pronounced density peak forms at $z = 6.05$ Å. This is in agreement with results reported by other groups [23–25]. The oxygen density profile obtained for SWM4_DP water is different from that obtained

for SPC/E water, but the differences are almost insignificant. For example, the peaks observed on the oxygen density profile for SWM4_DP are higher and narrower than those observed for SPC/E water. Quantitative calculations presented below indicate that water molecules are predicted to pack in the interfacial layer at a constant surface coverage (9.9 water molecules per $nm^2$), independently on the water model implemented. The hydrogen density profiles (top right) also show negligible differences between results obtained implementing either the SPC/E or the SWM4_DP water models. The results presented on the top panels of Fig. A.2 demonstrate that the distribution of oxygen and hydrogen atoms of water molecules in the direction perpendicular to the surface are predicted to be comparable when either the rigid non-polarizable SPC/E or the polarizable SWM4_DP water models are implemented.

The next question I address is whether including the polarizability of carbon atoms of graphene and the polarizability of water molecules will affect the predicted structure of water. In the middle panels of Fig. A.2 I compare the results obtained using the polarizable SWM4_DP model of water, combined with a Drude-particle model to describe polarizable effects in the carbon atoms of graphene. The results suggest that including the polarizability of graphene negligibly affects the vertical distribution of oxygen atoms of interfacial water (left panel). However, the prediction for the density profiles of hydrogen atoms (right panel) is affected by the polarizability of carbon atoms. In particular, a small shoulder at z = 2.15 Å gradually forms when the polarizability increases. The shoulder found at z = 2.15 Å on the hydrogen density profile is 1 Å closer to the surface than the first oxygen peak observed on the oxygen density profile. This suggests that polarizability affects the orientation of interfacial water molecules. My results indicate that the number of water molecules in the first hydration layer projecting one of their hydrogen atoms toward the surface increases when the graphene polarizability increases. This observation is supported by additional results, discussed below, for the orientation of interfacial water molecules and by the estimation of the number of water molecules pointing one of their hydrogen atoms towards the surface. The results just discussed show that polarizability is important in predicting the orientation of interfacial water molecules near neutral graphene. The next question I address is whether or not the same observation holds when the graphene surface, instead of being neutral, is charged.

In the bottom panels of Fig. A.2 I present the density profiles predicted when the SWM4_DP water is simulated on charged non-polarizable and charged polarizable graphene surfaces. Graphene was either positively or negatively charged. The density profiles for SWM4_DP water on neutral non-polarizable graphene (black line) are also shown for comparison. The results shown in the bottom panels of Fig. A.2 indicate that the surface charge density has a strong effect in determining the orientation of interfacial water. More importantly for the scopes of the present work, however, is that when graphene is charged, my results show that including the polarizability of graphene in the calculations has little effect. For instance, the oxygen density profile (left panel) for water on $-8$ $\mu C/cm^2$ non-polarizable

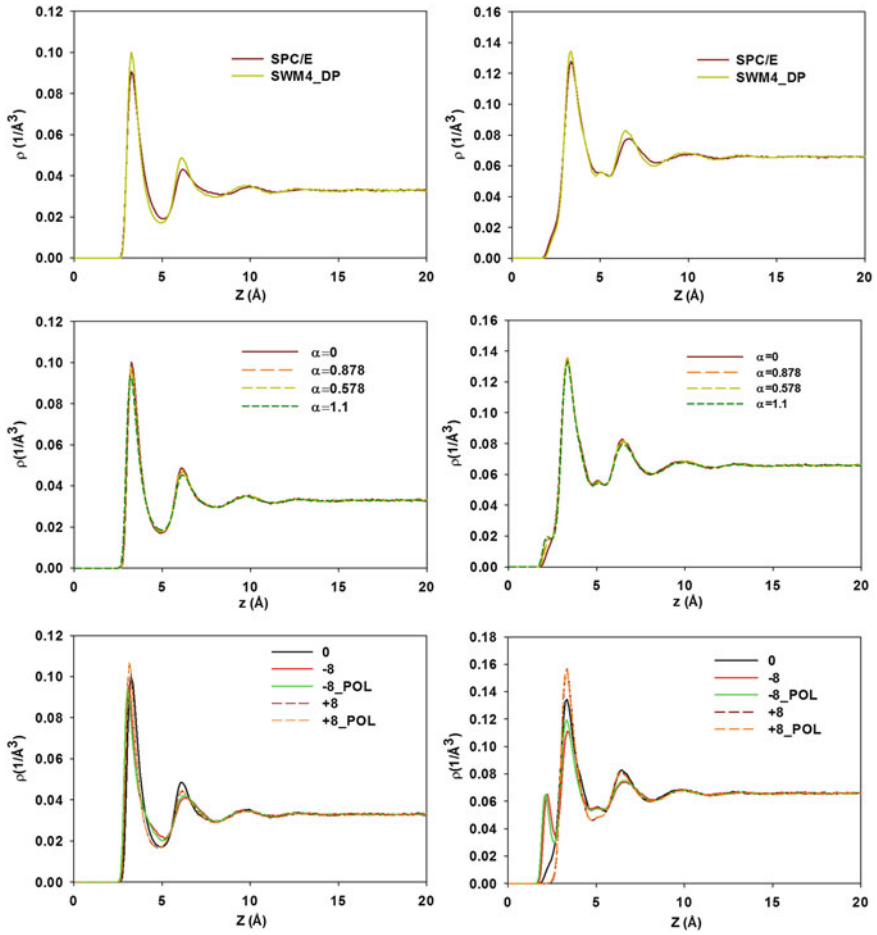


**Fig. A.2** *Top* Oxygen (*left*) and hydrogen (*right*) density profiles of SPC/E and SWM4_DP water on neutral non-polarizable graphene surfaces. *Middle* Oxygen (*left*) and hydrogen (*right*) density profiles of SWM4_DP water on neutral polarizable graphene surfaces of different polarizability α. *Bottom* Oxygen (*left*) and hydrogen (*right*) density profiles of SWM4_DP water on charged non-polarizable and charged polarizable graphene surfaces

graphene (solid red line) shows little difference compared to that obtained on polarizable graphene (green solid line). The same can be repeated for the hydrogen density profile (right panel) on +8 $\mu C/cm^2$ non-polarizable or polarizable graphene.

### A.4.2 Orientation

In the left panel of Fig. A.3 I present the orientation distribution of interfacial SPC/E (pink circles) and SWM4_DP (black circles) water on neutral non-polarizable graphene. In the left panel I also report the results obtained for SWM4_DP water on neutral polarizable graphene (red circles, green triangles, and yellow triangles). The angle Φ was defined as the angle between the OH bond of one water molecule and the normal vector of the surface. When $\cos(\Phi) = 1$, the OH bond points away from the surface. When $\cos(\Phi) = -1$, the OH bond points towards the surface. The probability $P[\cos(\Phi)]$ of observing the various angles Φ for the water molecules whose oxygen atom is found within 5 Å from the surface is reported. It should be remembered that Lee et al. [46] were the first to predict that water molecules within the first hydration layer near a hydrophobic surface point some of their OH groups towards the surface to minimize the number of hydrogen bonds lost because of the presence of the surface. Many subsequent simulations for water on graphite agree with such prediction [23–25]. Qualitatively, the results obtained here on the neutral graphene also show that some of the water molecules within the first hydration layer point one of their OH bonds towards the surface. Further, the results obtained for SPC/E (pink circles) and SWM4_DP (black circles, obtained for $\alpha = 0$) suggest that the polarizability of water insignificantly affects the orientation of interfacial water when graphene is neutral and not polarizable. However, my results show that the polarizability of graphene affects the orientation of interfacial water. The results obtained for interfacial SWM4_DP water on neutral polarizable graphene indicate that the probability $P[\cos(\Phi) \sim -1]$ increases when the polarizability increases, indicating that more interfacial water molecules point one of their OH bonds towards the surface when the surface polarizability increases.

In the right panel of Fig. A.3 I report the number of oxygen and hydrogen atoms found in the first peak on the density profiles obtained for SPC/E water on neutral non-polarizable graphene (pink circles), and for SWM4_DP water on neutral polarizable graphene. The number of oxygen and hydrogen atoms were counted up to 5 Å (the first minima on oxygen density profile) and 2.65 Å from the surface (the shoulder on the hydrogen density profile), respectively. On neutral non-polarizable graphene nearly 9 % of interfacial water molecules (either SPC/E or SWM4_DP) point one of their OH bonds toward the surface. On the most polarizable graphene considered ($\alpha = 1.1$), nearly 14 % of interfacial SWM4_DP water point one of their OH bonds toward the surface. At the expected polarizability of a carbon atom ($\alpha = 0.878$), approximately 12 % of interfacial water molecules point one OH bond towards the surface. Experimental results show that at water/air interface more than 20 % water molecules have ‘dangling’ OH bonds projecting into the air [47], suggesting that perhaps including polarizability is important for capturing the correct physics of the water/graphene interface as well. Experimental data necessary for validating my predictions are at present not available.

The orientation distribution of SWM4_DP water on neutral graphene surfaces, presented in the left panel of Fig. A.3, clearly indicates the effect of graphene

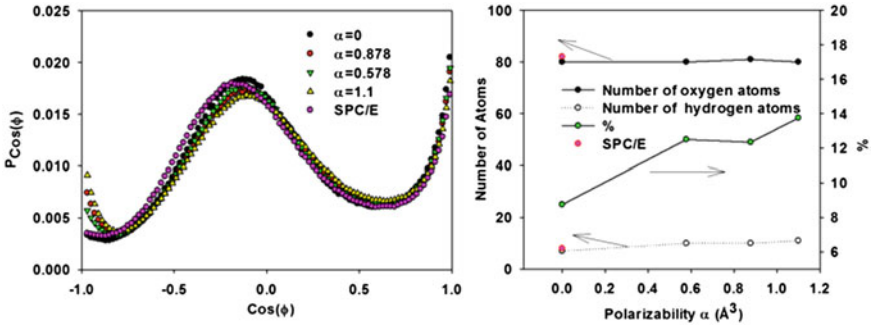


**Fig. A.3** *Left* The orientation distribution of SWM4_DP water molecules on polarizable graphene surfaces. Only the water molecules in the first hydration layer are considered in this calculation. *Right* The number of hydrogen and oxygen atoms of SWM4_DP water molecules within the first peaks observed on the atomic density profiles (see Fig. A.2). On both *left* and *right* panels, the results obtained for SPC/E water on non-polarizable graphene were also reported (*pink circle*) to compare with the results obtained for SWM4_DP (*black*) water on neutral non-polarizable graphene

polarizability on the orientation of interfacial water. Will the polarizability of graphene affect the orientation of water on graphene when the graphene, instead of being neutral, is charged? The orientation distributions of interfacial SWM4_DP water on charged non-polarizable and charged polarizable graphene are presented in Fig. A.4. The results obtained for SWM4_DP water on neutral non-polarizable graphene are also shown in this figure for comparison (black). Changing the surface charge density from negative to positive has the expected effect on the orientation of interfacial water. Briefly, water preferentially points more OH bonds towards the negatively charged surface (red triangles, note the high $P[\cos(\Phi) \sim -1]$ in

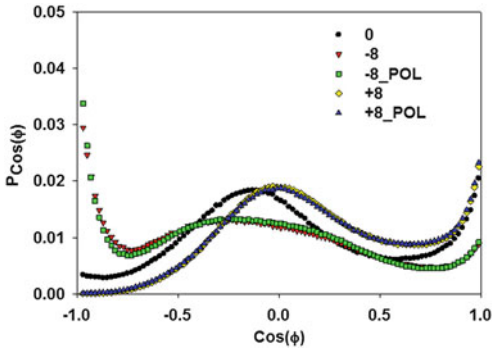


**Fig. A.4** The orientation distribution of SWM4_DP interfacial water on charged non-polarizable and charged polarizable graphene surfaces. The results obtained for SWM4_DP water molecules (*black circle*) on neutral non-polarizable graphene are also shown for comparison. Only water molecules in the first hydration layer are used for this analysis

Fig. A.4). On the contrary, water points no OH bonds towards the positively charged surface (yellow diamonds, note the low $P[\cos(\Phi) \sim -1]$ in Fig. A.4). I focus here on the effect of graphene polarizability on the orientation distribution of interfacial SWM4_DP water on charged graphene. My results show that such effect is negligible. For instance, the orientation distribution of interfacial water on $-8$ μC/cm$^2$ non-polarizable (red) and $-8$ μC/cm$^2$ polarizable graphene (green), or the orientation distribution of interfacial water on $+8$ μC/cm$^2$ non-polarizable (yellow) and $+8$ μC/cm$^2$ polarizable (blue) graphene are identical. The electrostatic forces clearly dominate the effect of polarizable forces.

### *A.4.3 Hydrogen-Bond Network*

In Fig. A.5 I present the number of hydrogen bonds per water molecule (left) and the hydrogen bond density profiles (right) obtained for SPC/E and SWM4_DP water on neutral non-polarizable graphene (top), for SWM4_DP water on neutral polarizable graphene surfaces (middle), and for SWM4_DP water on charged non-polarizable and charged polarizable graphene (bottom). One hydrogen bond was identified using the geometric criterion proposed by Marti [48]. The position of each hydrogen bond was considered as the middle point between the hydrogen of the donor and the oxygen of the acceptor molecules. The results presented in the top and middle panels indicate that the polarizability of either water or graphene have an insignificant effect on the hydrogen bond network. The water molecules in the first hydration layer (up to 5 Å from the surface) form fewer hydrogen bonds than the molecules in the bulk region do because of the asymmetry of the system (left panels). However, the hydrogen bond network is very dense in the contact layer as observed on the hydrogen density profiles (right panels) because the density of water molecules in the first hydration layer is high (see density profiles in Fig. A.2). These observations are in agreement with the results reported by Marti et al. [49] and Gordillo et al. [23]. The results obtained on charged graphene surfaces (bottom panels) also indicate that at the same surface charge density, the non-polarizable and polarizable graphene substrates do not affect the hydrogen bond network differently from each other.

### *A.4.4 Dynamical Properties*

In Fig. A.6 I present several dynamical properties computed for interfacial water on various graphene surfaces. Only water molecules within the first hydration layer were considered for these calculations. I computed the residence auto-correlation function (left panels), the mean square displacement as a function of time (middle panels), and the reorientation correlation function (right panels). The results are compared when different force fields were implemented.

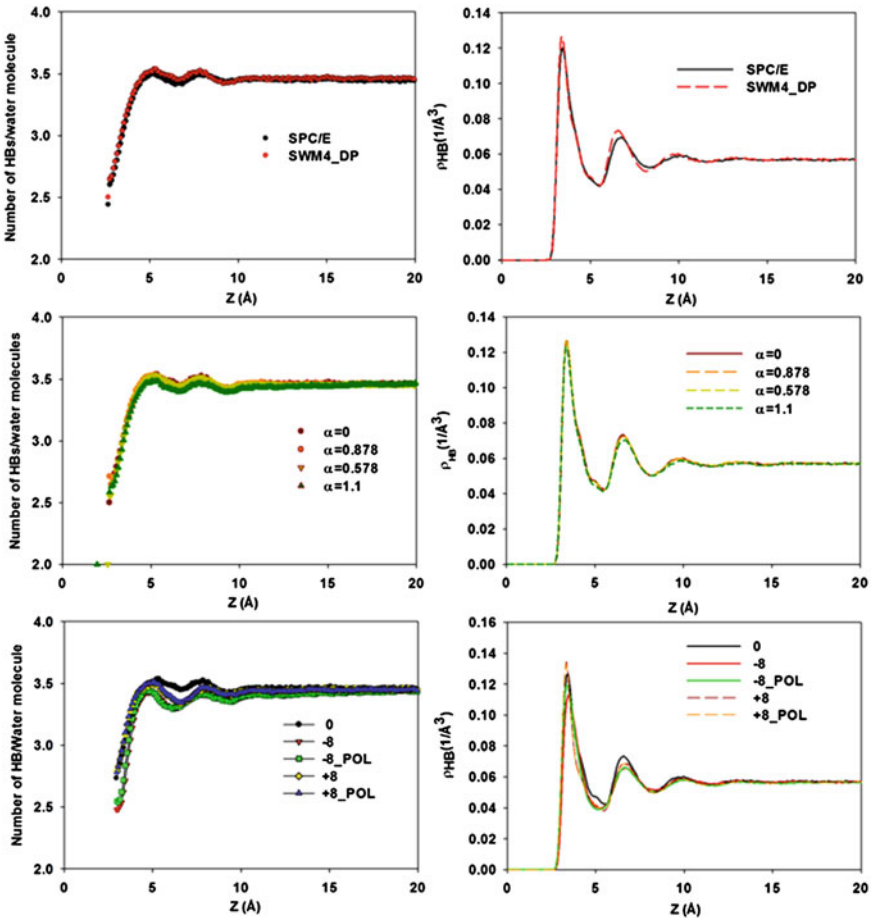


**Fig. A.5** Number of hydrogen bonds per water molecule (*left panels*) and hydrogen bond density profiles (*right panels*) as a function of vertical distance z from the surface. The results obtained for SPC/E and SWM4_DP water on neutral non-polarizable graphene, for SWM4_DP water on neutral polarizable graphene, and for SWM4_DP water on charged non-polarizable and charged polarizable graphene are shown in the *top*, *middle*, and *bottom* panels, respectively

The residence auto-correlation function was defined as: $C_R(t) = \frac{\langle P(t)P(0)\rangle}{P(0)P(0)}$. At time $t = 0$, P(0) = 1 for all the water molecules whose oxygen atom is found within the first peak on the oxygen density profile (see Fig. A.2). If the water molecules continuously stay in the first hydration layer when the time $t$ progresses, then P(t) = 1, otherwise, P(t) = 0. The auto-correlation function decays from 1 to 0 when the system evolves because the interfacial water molecules leave the hydration layer as time progresses [50]. By studying the residence auto-correlation function it is possible to estimate the average residence time for water molecules at

contact with the graphene (e.g., the time required for the auto-correlation function to decay from 1 to 1/e).

The in-plane MSD was quantified as: $(t) = \frac{< \sum [(x_i(t)-x_i(0))^2 + (y_i(t)-y(0))^2] >}{N(t)}$, where N(t) is the number of water molecules remaining in the hydration layer at time t. Note that as time progresses, $N(t)$ decreases. Once a water molecule leaves the hydration layer, it does not contribute any more to the mean square displacement, even if it returns after some time. The slope of the in-plane MSD as a function of time could be used to estimate the self-diffusion coefficient for water molecules in the direction parallel to the surface, although the correlation should last for infinite times, which is not possible as water molecules eventually leave the hydration layer. Qualitatively, I estimate the mobility of interfacial water from the initial slope of the MSD data. The larger of the slope, the faster interfacial water molecules diffuse [50].

The reorientation correlation function was obtained as: $C_{DM}(t) = \frac{<M(t)M(0)>}{<M(0)M(0)>}$, where $M(0)$ is the dipole moment of water molecule vector at time $t = 0$, $M(t)$ is the dipole moment of water molecules vector at time t. Only water molecules continuously staying within the first hydration layer were considered for this calculation. The slower the reorientation correlation function decays from 1 to 0, the slower the water molecules rotate [50]. The rotational diffusion can be estimated, qualitatively, from the time required by the reorientation correlation function to decay from 1 to 1/e.

The comparison of the dynamical properties obtained for SPC/E and SWM4_DP water on neutral non-polarizable graphene surface is shown in the top panels of Fig. A.6. The results for the residence correlation function (top left) demonstrate that the SPC/E water molecules stay in the contact layer on average shorter than SWM4_DP water molecules do. However, the MSD results (top middle) suggest that SPC/E and SWM4_DP water molecules have similar mobility in the direction parallel to the substrate. The reorientation correlation function data (top right) indicate that the SPC/E water molecules rotate more slowly than SWM4_DP water molecules do. This appears to be counter-intuitive, since SPC/E water was found to reside in the first hydration layer for shorter times than the SWM4_DP water. However, I note that the differences are rather small.

The dynamical properties predicted for SWM4_DP water on neutral graphene as a function of graphene polarizability (middle panels from the top) show differences only when the polarizability of a carbon atom is larger than $\alpha = 0.878$ Å. Because on neutral polarizable graphene the orientation of SWM4_DP water was found different compared to that on non-polarizable graphene, it is surprising that the dynamical properties of water are not affected by the surface polarizability when $\alpha < 0.878$ Å. It is possible that the dynamics of interfacial water molecules depend more strongly on the presence of ions, whose predicted behaviour (i.e., surface adsorption) might depend on polarizability [26]. This possibility will be explored in the future.

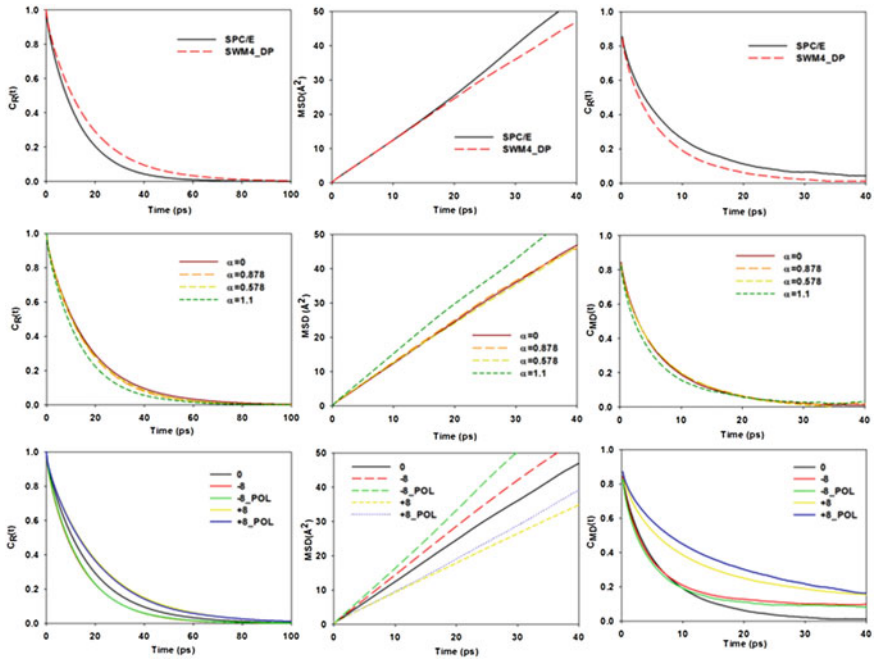


**Fig. A.6** Residence auto-correlation function (*left panels*), mean square displacement as a function of time (*middle panels*), and reorientation correlation function (*right panels*) for interfacial water on graphene surfaces. *Top*, *middle*, and *bottom* panels are for the results for SPC/E and SWM4_DP water on neutral non-polarizable graphene surface, SWM4_DP water on neutral graphene as a function of graphene polarizability, and SWM4_DP water on charged graphene, polarizable and non-polarizable, respectively

The structural properties of water on charged graphene were found not to depend on graphene polarizability. However, the dynamical properties predicted for interfacial SWM4_DP water on charged graphene appear to depend, to some extent, on the graphene polarizability (bottom panels of Fig. A.6). Note that these results were obtained when the polarizability α of carbon atoms of graphene was either 0 or equal to the expected value of 0.878 $Å^3$. The residence auto-correlation function data (bottom left) show no difference, as a function of surface polarizability, when graphene is charged. However, the MSD data (bottom middle) show that water molecules on charged polarizable graphene have faster mobility along the direction parallel to the substrate compared to water on charged non-polarizable graphene. For example, water molecules on the $-8$ μC/$cm^2$ non-polarizable graphene (dash red) diffuse more slowly than on the polarizable surface with the same surface charge density (dash green). The same can be repeated for the positively charged graphene. Experimental data such as those obtained from NMR or neutron scattering are needed to determine which of these predictions better reproduces reality. The reorientation correlation function data (bottom right) indicate that the effect of polarizability of graphene on the rotation of water on charged graphene is negligible.

## A.5 Conclusions

The importance of including the polarizability of water and graphene in molecular dynamics simulation of the water/graphene system was explored. A thin film of rigid SPC/E and polarizable SWM4_DP water on non-polarizable and polarizable graphene surfaces was simulated. The graphene surface was either maintained neutral or charged. The obtained results suggest that the SPC/E and SWM4_DP yield very similar structural properties of water on neutral non-polarizable graphene, while the dynamical properties of SPC/E and SWM4_DP on neutral non-polarizable graphene are slightly different. More importantly, I found that including explicitly in the calculations the polarizability of graphene enhances the number of interfacial SWM4_DP water molecules pointing one of their OH bonds toward the surface, although it insignificantly affects the dynamical properties of interfacial SWM4_DP water if the polarizability of carbon is smaller than $\alpha = 0.878$ Å. On charged graphene surfaces, the effect of polarizability of graphene on the structural properties and some of the dynamical properties of SWM4_DP water is negligible because the electrostatic forces dominate the polarization forces, as expected. For all cases, the hydrogen bond network is insensitive to the polarizability of both water and graphene. These results, when accompanied by experimental data, will provide a comprehensive picture of water properties and insight into the importance of polarization at graphene/water interface. Applications that will benefit from this fundamental understanding include the design of energy storage devices as well as water desalination processes.

## References

1. Bucher, D., & Kuyucak, S. (2008). Polarization of water in the first hydration shell of $K^+$ and $Ca^{2+}$ ions. *The Journal of Physical Chemistry*, *B* 112, (35), 10786–10790.
2. Picalek, J., Minofar, B., Kolafa, J., & Jungwirth, P. (2008). Aqueous solutions of ionic liquids: study of the solution/vapor interface using molecular dynamics simulations. *Physical Chemistry Chemical Physics*, *10*(37), 5765–5775.
3. Dang, L. X., & Chang, T. M. (2002). Molecular mechanism of ion binding to the liquid/vapor interface of water. *The Journal of Physical Chemistry B*, *106*(2), 235–238.
4. Stuart, S. J., & Berne, B. J. (1999). Surface curvature effects in the aqueous ionic solvation of the chloride ion. *The Journal of Physical Chemistry A*, *103*(49), 10300–10307.
5. Jungwirth, P., & Tobias, D. J. (2006). Specific ion effects at the air/water interface. *Chem*ical *Reviews*, *106*(4), 1259–1281.
6. Horinek, D., & Netz, R. R. (2007). Specific ion adsorption at hydrophobic solid surfaces. *Physical Reviews Letters*, *99*(22), 226104.
7. Brown, M. A., et al. (2008). Ion spatial distributions at the liquid-vapor interface of aqueous potassium fluoride solutions. *Physical Chemistry Chemical Physics*, *10*(32), 4778–4784.
8. Levin, Y. (2009). Polarizable ions at interfaces. *Physical Reviews Letters*, *102*(14), 147803.
9. Perera, L., & Berkowitz, M. L. (1991). Many-body effects in molecular-dynamics simulations of $Na^+(H_2O)N$ and $Cl^-(H_2O)N$ clusters. *The Journal of Chemical Physics*, 95(3), 1954–1963.
10. Dang, L. X., & Smith, D. E. (1993). Molecular-dynamics simulations of aqueous ionic clusters using polarizable water. *The Journal of Chemical Physics*, *99*(9), 6950–6956.

11. Jungwirth, P., & Tobias, D. J. (2002). Ions at the air/water interface. *The Journal of Physical Chemistry B*, *106*(25), 6361–6373.
12. Caleman, C., Hub, J. S., van Maaren, P. J., & van der Spoel D. (2011). Atomistic simulation of ion solvation in water explains surface preference of halides. *Proceedings of the National Academy of Sciences USA*, *108*(17), 6838–6842.
13. Geim, A. K., & Novoselov, K. S. (2007). The rise of graphene. *Nature Materials*, *6*(3), 183–191.
14. Geim, A. K. (2009). Graphene: Status and prospects. *Science*, *324*(5934), 1530–1534.
15. Rafiee, J., et al. (2012). Wetting transparency of graphene. *Nature Materials*, 11(3), 217–222.
16. Topsakal, M., Şahin, H., & Ciraci, S. (2012). Graphene coatings: An efficient protection from oxidation. *Physical Review B*, 85(15), 155445.
17. Simon, P., & Gogotsi, Y. (2008). Materials for electrochemical capacitors. *Nature Materials*, 7(11), 845–854.
18. Gao, W., et al. (2011). Direct laser writing of micro-supercapacitors on hydrated graphite oxide films. *Nature Nanotechnology*, 6(8), 496–500.
19. El-Kady, M. F., Strong, V., Dubin, S., & Kaner, R. B. (2012). Laser scribing of high-performance and flexible graphene-based electrochemical capacitors. *Science*, 335 (6074), 1326–1330.
20. Liu, C. G,, Yu, Z. N., Neff, D., Zhamu, A., & Jang, B. Z. (2010). Graphene-based supercapacitor with an ultrahigh energy density. *Nano Letters*, *10*(12), 4863–4868.
21. Artiles, M. S., Rout, C. S., & Fisher, T. S. (2011). Graphene-based hybrid materials and devices for biosensing. *Advanced Drug Delivery Reviews*, *63*(14–15), 1352–1360.
22. Machado, B. F., & Serp, P. (2012). Graphene-based materials for catalysis. *Catalysis Science & Technology*, 2(1), 54–75.
23. Gordillo, M. C., & Marti, J. (2008). Structure of water adsorbed on a single graphene sheet. *Physical Review B 78*(7), 075432.
24. Cicero, G., Grossman, J. C., Schwegler, E., Gygi, F., & Galli, G. (2008). Water confined in nanotubes and between graphene sheets: A first principle study. *Journal of the American Chemical Society*, *130*(6), 1871–1878.
25. Striolo, A., Chialvo, A. A., Cummings, P. T., & Gubbins, K. E. (2003). Water adsorption in carbon-slit nanopores. *Langmuir*, *19*(20), 8583–8591.
26. Sala, J., Guardia, E., & Marti, J. (2012). Specific ion effects in aqueous eletrolyte solutions confined within graphene sheets at the nanometric scale. *Physical Chemistry Chemical Physics*, *14*(30), 10799–10808.
27. Berendsen, H. J. C., Grigera, J. R., & Straatsma, T. P. (1987). The missing term in effective pair potentials. *Journal of Physical Chemistry*, *91*(24), 6269–6271.
28. Lamoureux, G., MacKerell, A. D., & Roux, B. (2003). A simple polarizable model of water based on classical drude oscillators. *The Journal of Chemical Physics*, *119*(10), 5185–5197.
29. Ryckaert, J.-P., Ciccotti, G., & Berendsen, H. (1977). Numerical integration of the cartesian equations of motion of a system with constraints: molecular dynamics of n-alkanes. *Journal of Computational Physics*, *23*(3), 327–341.
30. Lamoureux, G., & Roux, B. (2003). Modeling induced polarization with classical drude oscillators: Theory and molecular dynamics simulation algorithm. *The Journal of Chemical Physics 119*(6), 3025–3039.
31. Drude, P. (1902). *The Theory of Optics* (C. Riborg Mann & Robert A. Millikan, Trans.). New York: Longmans, Green.
32. Cheng, A., & Steele, W. A. (1990). Computer-simulation of ammonia on graphite .1. Low-temperature structure of monolayer and bilayer films. *The Journal of Chemical Physics*, *92*(6), 3858–3866.
33. Chang, T.-M. & Dang, L. X. (1996). Molecular dynamics simulations of $CCl_4$–$H_2O$ liquid—liquid interface with polarizable potential models. *The Journal of Chemical Physics*, *104*(17), 6772–6783.

34. Langlet, R., Devel, M., & Lambin, P. (2006). Computation of the static polarizabilities of multi-wall carbon nanotubes and fullerites using a Gaussian regularized point dipole interaction model. *Carbon*, *44*(14), 2883–2895.
35. Karapetian, K., & Jordan, K. D. (2003). *Properties of water clusters on a graphite sheet* (pp.139–150). Springer.
36. Kalluri, R. K., et al. (2012) Unraveling the potential and pore-size dependent capacitance of slit-shaped graphitic carbon pores in aqueous electrolytes. *Physical Chemistry Chemical Physics*, *15*(7), 2309–2320.
37. Van der Spoel, D., et al. (2005). GROMACS: Fast, flexible, and free. *Journal of Computational Chemistry*, *26*(16), 1701–1718.
38. Essmann, U., et al. (1995). A smooth particle mesh Ewald method. *The Journal of Chemical Physics*, *103*(19), 8577–8593.
39. Ho, T. A., Argyris, D., Cole, D. R., & Striolo, A. (2012). Aqueous NaCl and CsCl solutions confined in crystalline slit-shaped silica nanopores of varying degree of protonation. *Langmuir*, *28*(2), 1256–1266.
40. Yeh, I. C., & Berkowitz, M. L. (1999). Dielectric constant of water at high electric fields: Molecular dynamics study. *The Journal of Chemical Physics*, *110*(16), 7935–7942.
41. Ho, T. A., Papavassiliou, D. V., Lee, L. L., & Striolo, A. (2011). Liquid water can slip on a hydrophilic surface. *Proceedings of the National Academy of Sciences USA*, *108*(39), 16170–16175.
42. Argyris, D., Cole, D. R., & Striolo, A. (2009). Hydration structure on crystalline silica substrates. *Langmuir*, *25*(14), 8025–8035.
43. Argyris, D., Rajesh Tummala N. R., Cole, D., & Striolo, A. (2008). Molecular structure and dynamics in thin water films at the silica and graphite surfaces. *The Journal of Physical Chemistry C*, *112*(35), 13587.
44. Argyris, D., Tummala, N. R., Striolo, A., & Cole, D. R. (2008). Molecular structure and dynamics in thin water films at the silica and graphite surfaces. *The Journal of Physical Chemistry C*, *112*(35), 13587–13599.
45. Phan, A., Ho, T. A., Cole, D. R., & Striolo, A. (2012). Molecular structure and dynamics in thin water films at metal oxide surfaces: Magnesium, aluminum, and silicon oxide surfaces. *The Journal of Physical Chemistry C*, *116*(30), 15962–15973.
46. Lee, C. Y., Mccammon, J. A., & Rossky, P. J. (1984). The Structure of Liquid Water at an Extended Hydrophobic Surface. *The Journal of Chemical Physics*, *80*(9), 4448–4455.
47. Du, Q., Superfine, R., Freysz, E., & Shen, Y. R. (1993). Vibrational spectroscopy of water at the vapor/water interface. *Physical Review Letters*, *70*(15), 2313–2316.
48. Marti, J. (1999). Analysis of the hydrogen bonding and vibrational spectra of supercritical model water by molecular dynamics simulations. *The Journal of Chemical Physics*, *110*(14), 6876–6886.
49. Marti, J., Nagy, G., Gordillo, M. C., & Guardia, E. (2006). Molecular simulation of liquid water confined inside graphite channels: Thermodynamics and structural properties. *The Journal of Chemical Physics*, *124*(9), 94703–94709.
50. Allen, M. P., & Tildesley, D. J. (2004). *Computer simulation of liquids*. Oxford: Oxford University Press.

# Appendix B
# Integration of the Poisson Equation

The Poisson equation reads (the symbols are explained in the Chap. 4):

$$\frac{d^2\psi}{dz^2} = \frac{-1}{\mathcal{E}_o}\rho(z) \tag{B.1}$$

The first and second integrations with respect to the variable z, the distance from the charged surface, yield:

$$\frac{d\psi}{dz}(z) = \frac{-1}{\mathcal{E}_o}\int_0^z \rho(u)du + C_1 \tag{B.2}$$

$$\psi_z = \frac{-1}{\varepsilon_o}\int_0^z\int_0^s \rho(u)duds + C_1 z + C_2 \tag{B.3}$$

In Eqs. (B.2) and (B.3) u and s are dummy variables, $C_1$ and $C_2$ are constants of integration that are defined by imposing appropriate boundary conditions.

As the first boundary condition, I impose that

$$\frac{d\psi}{dz} = 0 \; at \; z = R/2$$

(i.e., the electric field at the pore centre is zero), which yields.

$$C_1 = \frac{1}{\mathcal{E}_o}\int_0^{R/2} \rho(u)du.$$

As the second boundary condition I impose $\psi(z) = 0 \; at \; z = 0$.



T.A. Ho, *Nanoscale Fluid Transport*, Springer Theses,
DOI 10.1007/978-3-319-47003-0

(i.e., the potential is chosen to be zero at z = 0), which for all electrochemical cells yields.

$$C_2 = 0.$$

The last equality implies that all electrical potentials shown in this work as expressed relative to the potential of the electrode at z = 0.

Using the relations just derived for $C_1$ and $C_2$, Eq. (B.3) becomes

$$\psi_z = \frac{-1}{\varepsilon_o} \int_0^z \int_0^s \rho(u)duds + \left[ \frac{1}{\mathcal{E}_o} \int_0^{R/2} \rho(u)du \right] z \tag{B.4}$$

From Eq. (B.4) I switch the order of integration within the double integrals to obtain

$$\psi_z = \frac{-1}{\varepsilon_o} \left[ \int_0^z \int_u^z \rho(u)dsdu - \left( \int_0^{R/2} \rho(u)du \right) z \right] \tag{B.5}$$

and subsequently

$$\psi_z = \frac{-1}{\varepsilon_o} \left[ \int_0^z (z-u)\rho(u)du - \left( \int_0^{R/2} \rho(u)du \right) z \right] \tag{B.6}$$

The results presented in Figs. 4.4 and 4.6 are obtained by numerical integration of Eq. (B.6) using the respective charge density profiles as input.